Spin currents and magnetization dynamics in multilayer systems

Erik van der Bijl
Spin currents and magnetization dynamics in multilayer systems
PhD thesis
Institute for Theoretical Physics
Utrecht University
ISBN: 978-94-622-8366-4
Printed by: Gildeprint Drukkerijen - Enschede

Spin currents and magnetization dynamics in multilayer systems

Spinstromen en magnetisatiedynamica in meerlaags systemen

(met een samenvatting in het Nederlands)

Proefschrift

ter verkrijging van de graad van doctor aan de Universiteit Utrecht op gezag van de rector magnificus, prof. dr. G.J. van der Zwaan, ingevolge het besluit van het college voor promoties in het openbaar te verdedigen op dinsdag 28 januari 2014 des ochtends te 10.30 uur

door

Erik van der Bijl

geboren op 26 november 1985 te Rotterdam

Promotor : Prof. dr. ir. H.T.C. Stoof
Co-promotor: Dr. R.A. Duine

This work is part of the research programme of the Foundation for Fundamental Research on Matter (FOM), which is part of the Netherlands Organisation for Scientific Research (NWO).

Contents

Publications

The main chapters of this Thesis are based on the following works:

- chapter 3:
  E. van der Bijl and R.A. Duine, *Current induced torques in textured Rashba Ferromagnets*, *Phys. Rev. B* **86**, 094406 (2012).

- chapter 4:
  E. van der Bijl, A. Sakai and H. Kohno, *Microscopic calculation of thermally induced spin torques, II Spin-Orbit Torques*, *in preparation.*

- chapter 5:
  E. van der Bijl, R. E. Troncoso and R.A. Duine, *Magnetic-texture-controlled transverse spin injection*, *Phys. Rev. B* **88**, 064417 (2013).

Other publications

- E. van der Bijl and R.A. Duine, *Anomalous Hall conductivity from the dipole mode of spin-orbit-coupled cold-atom systems*, *Phys. Rev. Lett.* **107**, 195302 (2011).

Chapter 1

Introduction

Early in the nineteenth century Oersted discovered that a current generates a magnetic field. He observed this magnetic field using the deflection of his compass needle in the presence of a current. His discovery led the French physicist Ampère to his law that describes the force due to the magnetic interaction between two current conducting wires. In addition to a mathematical expression for the strength of that force, Ampère also gave a physical understanding of the effect in terms of the dynamics of a new particle with electric charge that is now known as the electron. The work of Ampère forms the foundation for the theory of electromagnetism, firmly established at the end of the nineteenth century, that describes all interactions between electromagnetic fields and the dynamics of charged particles. Even after a century of unprecedented technological developments in electronics, which revolutionized the world, devices are still mostly described by these nineteenth-century laws and utilize only the electron charge. In particular, non-volatile magnetic memory devices such as hard disk drives depend on progressive miniaturization of electromagnetic inductive coils for reading and for generating magnetic fields, that are referred to as Oersted fields, to write magnetic information.

The discovery of the giant magnetoresistance (GMR) independently by the groups of Grünberg [1] and Fert [2] has changed this. The GMR is observed in multilayer structures that consist of two or more ferromagnetic layers separated by a conducting paramagnetic or nonmagnetic layers, called spin valves. When the two ferromagnetic layers have their magnetizations parallel the conductance is significantly larger than in the antiparallel configuration. This holds both for the current perpendicular and parallel to the interface planes of the spin valve. The large difference in conductivity, which persists up to room temperatures, is due to the spin polarization of the conduction electrons in the magnets. With the observation of the GMR by Grünberg and Fert, who were awarded the Nobel prize in 2007, the field of magnetoelectronics, also called spin electronics or *spintronics*[1], was initiated [4, 5].

The GMR effect can be explained using a two-current model of electron transport. These two currents in the ferromagnet consist of majority and minority electrons which have their spin parallel or antiparallel to the magnetization. The conductance for both

[1] In addition to the work by Fert and Grünberg the field of semiconductor spintronics was initiated by the proposal for the spin transistor by Datta and Das [3].

channels differs since the density of states at the Fermi level is different for the two spin states. A higher density of localized states leads to more states to scatter to thereby lowering the conductivity. The result is that ferromagnets act as a spin filter for the current. Suppose that the resistance of a single ferromagnet for majority electrons is R_+ while that for minority electrons is R_-. When the magnetizations of the ferromagnets are parallel the total resistivity R_P for the current through the spin valve is given by two parallel series of R_+ and R_- resistances. Because majority electrons in the first magnet will also be majority electrons in the second ferromagnet. When the magnetization directions are antiparallel the total resistance R_AP is given by two series of R_+ and R_- resistances connected in parallel since the notion of majority and minority swaps, as shown in Fig. 1.1. The relative change in resistance between the parallel and antiparallel configuration is then given by $\eta = (R_\mathrm{AP} - R_\mathrm{P})/R_\mathrm{P}$, which is the so-called GMR ratio. In Fig. 1.1 $\eta = 1.5\%$ is observed in a trilayer at room temperature [1]. In multilayer structures at 4.2 Kelvin the group of Fert reported a change of almost 50% [2].

Based on GMR, spin valves can be used as a very sensitive magnetic field sensor. By pinning one of the ferromagnets in one direction, the other ferromagnet in the spin valve can easily align to small magnetic fields. The relative orientation can then be easily detected electrically using GMR. The work by Parkin [6] greatly contributed to the fact that technology based on GMR replaced other methods to read the magnetic orientation of a domain within the ten years following its original discovery. More recently, GMR stacks are being replaced by spin valves where the material between the ferromagnets forms a thin nonconducting barrier. These structures show a large tunneling magnetoresistance that can lead to doubling of the resistance of the spin valve depending on the relative orientation of the ferromagnets.

The understanding of the GMR crucially depends on a degree of freedom of the electrons that aligns to the magnetization. Spintronics seeks to utilize and study this property of the electron, namely its intrinsic angular momentum, *i.e.*, its spin. This intrinsic angular momentum is rooted in the fundamentals of quantum mechanics. Associated to the spin angular momentum is the magnetic moment of the electron $\boldsymbol{\mu}_s = -g\mu_B \boldsymbol{s}/\hbar$, where $\hbar$ is Planck's constant $g \approx 2$ is the g-factor and the Bohr magneton is given by $\mu_B = \hbar|e|/2m_e c$, where $-|e|$ and m_e are the charge and mass of the electron and c is the speed of light. The interaction of the spin degree of freedom with a magnetic field $\boldsymbol{H}$ is given by the Zeeman interaction which is given by $-\boldsymbol{H} \cdot \boldsymbol{\mu}_s$. Due to the magnetic moment of electrons we can in a simplified picture think of them as tiny bar magnets moving through materials, a picture we extend in the next Chapter.

In the discussion of the GMR we noted the polarizing effect the magnetization has on a current that passes through a conducting ferromagnet. An opposite effect in spin valves was introduced by Berger [7] and Slonczewksi [8]. Instead of considering the effect of the magnetization on the current, they considered the effect a spin-polarized current has on the ferromagnet. They predicted that switching the orientation of the magnetization ferromagnet was possible using a spin-polarized current [9, 10]. This is a result of the interaction of the spin-polarized current with the magnet via the spin-transfer torque. This torque arises due to the misalignment of the spin polarization of the current and

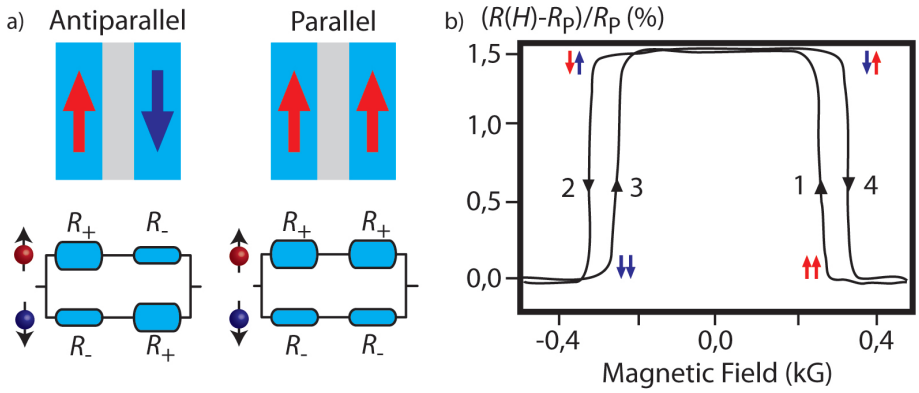

Figure 1.1: Illustration of the GMR. a) An illustration of a spin valve in parallel and antiparallel configuration. Below the resistance for majority and minority electrons. b) First observation of the GMR at room temperature in a single spin valve. The resistance is measured as a function of the magnetic field. The magnetization configuration changes four times as indicated in the figure. When the field decreases from high positive values one of the ferromagnets changes orientation thereby switching the valve to the antiparallel state. A magnetic field in the other direction also switches the other magnetic layer in the valve. Adapted from Ref. [1].

the magnetization. This misalignment will cause a transfer of angular momentum from the current to the magnetization. The relative change in angular momentum is then reflected in a modified spin polarization of the current and an equal but opposite change in the magnetization. For reviews see Refs. [11, 12]. Spin-transfer torques also exist in continuous magnetic textures. The interplay between (spin-polarized) current and such magnetic textures is the subject of this Thesis.

For the continuous systems where the magnetization is a function of the position in the ferromagnet we have to generalize the above picture. Spin torques can be understood in textured ferromagnets by assuming the spins align to the local magnetization adiabatically when the electrons move through the magnet. This adiabatic approximation is justified by considering the separation in timescales between the electronic degrees of freedom, which are on the order of picoseconds, and the timescale of magnetization dynamics which is typically nanoseconds. Above we argued that the spin-transfer torque arises from a transfer of angular momentum from the spin-polarized current to the ferromagnet. Here we formalize this statement. Consider a ferromagnet with a position dependent magnetization direction $\boldsymbol{m}(\boldsymbol{x})$. Like we discussed at the introduction of the GMR, a current through a ferromagnet will be spin polarized such that we can write for the spin current $\boldsymbol{j}_s$, up to zeroth order in gradients of the magnetization $\boldsymbol{j}_s = P\boldsymbol{m}(\boldsymbol{x})\boldsymbol{j}_c$, where $P = (\sigma_+ - \sigma_-)/(\sigma_+ + \sigma_-)$ is the spin polarization of the charge current $\boldsymbol{j}_c$ in terms of the conductivities of majority (σ_+) and minority (σ_-) electrons. Here $\boldsymbol{m}$ is a unit vector along the magnetization. In the absence of spin-relaxation processes the change

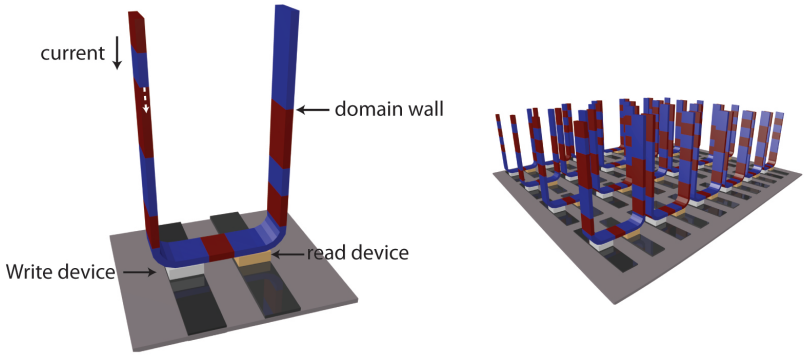

Figure 1.2: Illustration of the envisioned racetrack memory. By applying current pulses to the ferromagnetic wire all domain walls move in the same direction due to the spin-transfer torques. In this way the magnetic domains, that store the information, can be moved to the write and read devices.

in the spin angular momentum density associated with the moving electrons is given by the continuity equation $\partial \boldsymbol{s}/\partial t + \boldsymbol{\nabla} \cdot \boldsymbol{j}_s = 0$. The change in magnetization direction leads to a change in the angular momentum of the spins $\boldsymbol{\nabla} \cdot \boldsymbol{j}_s = P(\boldsymbol{j} \cdot \nabla)\boldsymbol{m}(\boldsymbol{x})$. Since the total angular momentum of the combined spin and magnetization system is conserved the angular momentum associated with the magnetization is changed by an equal amount. Thus the change in magnetization direction due to the spin current can be summarized as $\dot{\boldsymbol{m}}|_{\mathrm{STT}} = \boldsymbol{\tau}_{\mathrm{STT}}$, where the spin-transfer torque is given by [13, 14]

$$\boldsymbol{\tau}_{\mathrm{STT}} = \frac{g\sigma\mu_B P}{2|e|M_s}(\boldsymbol{E} \cdot \nabla)\boldsymbol{m}, \tag{1.1}$$

where M_s is the saturation magnetization of the ferromagnet, $\sigma = \sigma_+ + \sigma_-$ is the total conductivity of the magnet [15] and the charge current is written as the conductivity times the electric field $\sigma \boldsymbol{E}$. The factor $g\mu_B/2|e|$ is the magnetic moment associated with the spin current. This expression is first order in the texture gradient and hence is called the adiabatic spin-transfer torque. Note that the expression in Eq. (1.1) is even under time reversal when written in terms of a current, which means it is reactive [16–18].

In addition to the reactive adiabatic spin-transfer torque there also is the dissipative adiabatic spin-transfer torque, which is sometimes called confusingly the non-adiabatic spin-transfer torque. This torque breaks time-reversal symmetry and is associated with dissipative processes such as spin relaxation. The influence of these dissipative processes is captured by the dimensionless parameter β. At low temperatures the magnetization has a fixed modulus. This means that only torques perpendicular to the magnetization can influence it. It follows that there is only one possible direction for the dissipative adiabatic spin-transfer torque which is is obtained by taking the vector product with the reactive torque, thus we arrive at the total expression for the adiabatic torques,

$$\boldsymbol{\tau}_{\mathrm{STT}} = \frac{g\sigma\mu_B P}{2|e|M_s}\sigma\left[(\boldsymbol{E} \cdot \nabla)\boldsymbol{m} + \beta \boldsymbol{m} \times (\boldsymbol{E} \cdot \nabla)\boldsymbol{m}\right]. \tag{1.2}$$

Note that the dissipative torque is also referred to as the field-like torque in the literature.

The implications of spin-transfer torques in discrete or continuous ferromagnetic textures for technology are tremendous. The spin-transfer torque has the advantage over switching of the magnetic fields using the Oersted field associated with current, because it allows for far greater miniaturization. This is due to the scaling of the spin-transfer torques with the current density instead of the scaling with current of the Oersted field. Today the first commercially available magnetic random access memory can be bought that uses the tunnel magnetoresistance to read bits and uses, thermally assisted, spin-transfer torques to write [19]. Since the information is stored in the magnetization direction these magnetic random access memory devices retain their information even without a permanent current that is used in conventional random access memory devices. This has two advantages, namely lower power consumption when the bit is just stored and non-volatility. Another inspiring application of spin-transfer torques is the proposed racetrack memory device [20] . In this setup information can be stored in the third and unused dimension and data is transported using the spin-transfer torques through the ferromagnets. This allows for a very high information density in a nonvolatile memory.

The reverse effect of spin-transfer torques in continuous textures is the generation of charge current by dynamic magnetization. This effect is due to so-called spin motive forces, or is alternatively called spin pumping. Spin pumping into a non-magnetic metal can be done by a precessing homogeneous magnetization [21] but also by a time dependent magnetic texture such as moving domain walls [18, 22–25]. In the next Section we show that spin pumping and spin-transfer torques are related by Onsager's reciprocity relations [26], which shows that they are two manifestations of the same underlying coupling.

Above we introduced reactive and dissipative spin-transfer torques in magnetic textures, examples of such textures are described in Sec. 1.2. We sketched how these torques can be understood as the transfer of angular momentum from the spin current to the ferromagnet. The qualitative description we provided so far can be put on more formal footing. The spin-transfer torques can be understood as arising from the spin Berry phase [27, 28] that the spin accumulates as it traverses the magnetic texture. Another perspective on the transfer torques comes from making a local rotation of the spin quantization axis, choose the magnetization direction as the local spin quantization axis. Because the quantization axis depends on position and time, the transformation introduces an additional U(1) gauge field that the electron interacts with. Associated with these gauge fields are emergent or effective electric and magnetic fields that lead to the spin motive forces and, as we shall see later, on topological Hall effects.

The above frameworks allow for complementary viewpoints on spin-transfer torques and spin pumping, and these approaches are easily generalized to other textured systems. For example, in antiferromagnetic systems spin torques are predicted just as well. The spin torques in these systems are similar to their magnetic cousins in Eq. (1.2) but with the staggered magnetization or Néel vector $\boldsymbol{n}(\boldsymbol{x}, t)$ replacing the magnetization [29–31].

For systems with strong spin-orbit (SO) coupling the above introduced frameworks can be generalized. In addition to coupling to the local magnetization, the spins now also couple to the electron's momentum via SO coupling. The SO coupling can be interpreted

as a phase-space dependent magnetization $\boldsymbol{\Omega}(\boldsymbol{p})$ which also leads to spin torques and spin motive forces. These torques are also present in systems with a homogeneous magnetization, in contrast to the spin-transfer torques as introduced in Eq. (1.2) which depend crucially on the gradient in the magnetization [23, 32–36].

Temperature gradients can drive charge currents via the Seebeck effect, which is one of the well-known effects in thermoelectrics. Since the spin-transfer torques are induced by (polarized) currents it is interesting to see whether thermally induced spin torques can be explained by the spin-dependent Seebeck coefficients or whether also a contribution from polarized heat currents exists. The field that investigates the interactions between spin, charge and heat transport is called spin caloritronics [37]. The incorporation of temperature gradients in a microscopic description of spin transport requires the introduction of new concepts which we study in Chapter 4 of this Thesis.

1.1 Onsager reciprocity and hydrodynamics

The precise form of the parameters associated with spin-transfer torques and spin motive forces could be calculated using microscopic approaches such as scattering theory [38, 39], Kubo formalism [15], Keldysh [40] or other quantum kinetic theories [41, 42]. We can, however, also study the coupling between the magnetization and current on a phenomenological level within the framework of hydrodynamics [43, 44]. Within this framework we consider the linear response of the magnetization dynamics and charge current. The parameters are restricted by the general principle of thermodynamics that the entropy should on average increase in the system.

In this Section we formalize the notion that spin-transfer torques and spin pumping are reciprocal processes. In fact they are related by Onsager's reciprocity relations. These relations [45] describe how the response, close to equilibrium, of physical quantities is related. The relations are based on the transformation under time-reversal of these quantities. In this Thesis we are interested in the dynamics of the direction of magnetization described by its time-derivative $\dot{\boldsymbol{m}}$ and its relation with current density $\boldsymbol{j}_c$. In principle we are free to write down any linear response matrix that relates these fluxes to some (applied) forces. But for Onsager's relations to hold we need to use the thermodynamic conjugates to the fluxes ξ, which are defined as $F_i = \delta\mathcal{F}/\delta\xi^i$, where $\mathcal{F}$ is the free energy of the system. For the current density and magnetization these are $\boldsymbol{H}_{\text{eff}}$ the effective field and $\boldsymbol{E}$ the electric field, respectively. This means that the change in entropy for a system slightly out of equilibrium is given by $\dot{\mathcal{S}} = \dot{\boldsymbol{m}}\cdot\boldsymbol{H}_{\text{eff}} + \boldsymbol{j}_c\cdot\boldsymbol{E}$ where these conjugated quantities are related via the linear response matrix defined by

$$\begin{pmatrix} \boldsymbol{j}_c \\ \dot{\boldsymbol{m}} \end{pmatrix} = \begin{pmatrix} \boldsymbol{L}_{jj} & \boldsymbol{L}_{j\boldsymbol{m}} \\ \boldsymbol{L}_{\boldsymbol{m}j} & \boldsymbol{L}_{\boldsymbol{m}\boldsymbol{m}} \end{pmatrix} \begin{pmatrix} \boldsymbol{E} \\ \boldsymbol{H}_{\text{eff}} \end{pmatrix}. \tag{1.3}$$

Onsager's relations now imply that $L_{\boldsymbol{m}j}[\boldsymbol{m}] = -(L_{j\boldsymbol{m}})^T[-\boldsymbol{m}]$, where the superscript T means transposition of the matrix, which follow from $\boldsymbol{m} \to -\boldsymbol{m}$ under time reversal [46]. This means that current-induced torques on the magnetization are directly related

to currents induced by dynamics of the magnetization. Once we have an expression for current-induced torques we can easily obtain the associated spin motive forces and vice versa.

To be more explicit, we consider the Landau-Lifshitz-Gilbert (LLG) equation for the dynamics of the magnetization augmented with the adiabatic spin-transfer torques that were given in Eq. (1.2). The LLG equation now reads

$$\dot{\boldsymbol{m}} = -\gamma\mu_0 \boldsymbol{m} \times \boldsymbol{H}_{\text{eff}} + \alpha_G \boldsymbol{m} \times \dot{\boldsymbol{m}} + \boldsymbol{\tau}_{\text{STT}}, \tag{1.4}$$

where α_G is the Gilbert damping parameter that describes the magnetization relaxation effects within the ferromagnet. As discussed above, the adiabatic spin-transfer torques are linear in the external field $\boldsymbol{E}$, and correspond to the off-diagonal part of the response matrix given by $L_{\boldsymbol{mj}}$. Using the Onsager relation we are able to write down the effect the spin-dynamics has on the currents, which yield the form [26]

$$j_c^i = -\frac{\gamma\hbar}{2}\sigma P \boldsymbol{H}_{\text{eff}} \cdot \left[(1 + \beta \boldsymbol{m}\times)\nabla^i \boldsymbol{m}\right]. \tag{1.5}$$

Using the LLG equation we obtain the spin motive forces $\boldsymbol{F}_\pm = \pm F_s$ that act on the majority and minority electrons in opposite direction

$$F_s^i = \left(\frac{\partial \boldsymbol{m}}{\partial t} \times \frac{\partial \boldsymbol{m}}{\partial x^i}\right) \cdot \boldsymbol{m} + \beta \frac{\partial \boldsymbol{m}}{\partial t} \cdot \frac{\partial \boldsymbol{m}}{\partial x^i}. \tag{1.6}$$

1.2 Magnetic textures

For the hydrodynamic description of the magnetization dynamics we introduced the effective field $\boldsymbol{H}_{\text{eff}} = -\frac{\delta E_{\text{MM}}}{\delta \boldsymbol{m}(\boldsymbol{x}) M_s}$ as the derivative of the free-energy functional of the ferromagnetic texture. This free-energy functional determines also the stable magnetic textures. The form of the micromagnetic or free-energy functional depends on the microscopic interactions of the ferromagnetic moments with each other and the conduction electrons, which, in turn, depend on the underlying ionic lattice. Moreover, the long-range dipole forces also cause the magnetization to depend on the shape of the sample. A detailed description is beyond the scope of this work. However, we can understand the phenomenology of the free-energy functional from symmetry arguments using Ginzburg-Landau theory for the magnetization $\boldsymbol{M}(\boldsymbol{x})$.

For an isotropic ferromagnet, thus without external field or anisotropies only even powers of $\boldsymbol{M}(\boldsymbol{x}) \cdot \boldsymbol{M}(\boldsymbol{x})$ and $(\boldsymbol{\nabla M})^2$ are allowed in the free energy, since only those transform as scalars under rotations, and are, like the free energy, even under time reversal. We are interested in the magnetization at low temperatures where the magnetization has a fixed modulus, thus $\boldsymbol{M}(\boldsymbol{x}) = M_s \boldsymbol{m}(\boldsymbol{x})$. Therefore all terms without gradient, that govern the order of the phase transition are constant in our discussion. Since the form and crystal structure of the ferromagnet make the system anisotropic along some axes, but do not give a preferred direction, those terms should be (at least) quadratic in the magnetization direction. A preferred direction is introduced by an external magnetic field which results in a linear coupling to the magnetization. In realistic systems anisotropies

exist which we include up to second order in the magnetization. We retained only the lowest order term in the gradient of the magnetization, since it is enough for our discussion below.

The micromagnetic free-energy functional that suffices for our discussion of ferromagnetic textures is given by

$$E_{\mathrm{MM}} = \frac{1}{2}\int d\boldsymbol{x}\left\{J(\boldsymbol{\nabla}\boldsymbol{m}(\boldsymbol{x}))^2 + M_s\boldsymbol{m}(\boldsymbol{x})\cdot\overleftrightarrow{K}\cdot\boldsymbol{m}(\boldsymbol{x}) - \mu_0 M_s\boldsymbol{H}\cdot\boldsymbol{m}(\boldsymbol{x})\right\}, \tag{1.7}$$

where the exchange stiffness $J > 0$ expresses the energy cost of a non-collinear arrangement of the magnetization. The anisotropy depends on the crystal structure and/or exchange coupling to an adjacent layer. We consider uniaxial anisotropy here with a diagonal matrix $\overleftrightarrow{K}$ with an easy and hard axis anisotropy characterized by $K_e < 0$ and $K_h > 0$, respectively. The total magnetic field consists of the sum of the external applied field $\mu_0\boldsymbol{H}_{\mathrm{ext}}$ and the demagnetization field $\mu_0\boldsymbol{H}_d$, where μ_0 is the vacuum permeability. In principle, the demagnetization field should be determined from Maxwell's equations. Here, we assume a local relation so that the demagnetization field is related to the magnetization via the demagnetization tensor, $\boldsymbol{H}_d = -M_s\overleftrightarrow{N}\cdot\boldsymbol{m}(\boldsymbol{x})$. The demagnetization tensor depends on the geometry of the ferromagnet. For the thin ferromagnetic strips used in most experiments the component perpendicular to the strip dominates which results in an in-plane magnetization. The functional form of the demagnetization field is the same as the anisotropy so in the following we include its effects into the effective anisotropy $\overleftrightarrow{K}_{\mathrm{eff}} \equiv \overleftrightarrow{K} - \mu_0 M_s^2\overleftrightarrow{N}$ and refer to it simply as the anisotropy.

In the absence of an external applied field the ground state of the above free-energy functional is doubly degenerate, the solutions correspond to homogeneous magnetizations along the easy axis anisotropy. Between two different realizations of the ground state transient regions exist which are called domain walls. In the next Section we derive their form based on the energy functional we motivated above and study their motion under influence of driving forces such as an externally applied magnetic field and currents via the spin-transfer torques.

1.2.1 Domain walls

In this Section we consider the structure and dynamics of magnetic domain-wall configurations. The direction of the magnetization can be characterized by two domain-wall angles. We define these angles such that θ_{dw} is the angle with the easy axis and φ_{dw} the angle with the hard-axis anisotropy in the perpendicular plane. The ground states of the systems are characterized by $\theta_{\mathrm{dw}} \in \{0, \pi\}$. Using the micromagnetic energy we can calculate the form of the domain wall. For simplicity, we consider one-dimensional domain walls. The angle with the easy axis $\theta_{\mathrm{dw}}(x)$ is a function of coordinate along the strip, which smoothly interpolates between the ground state solutions. The domain-wall configurations with the lowest energy will always be in the plane perpendicular to the hard axis, this means that the other domain-wall angle is given by $\varphi_{\mathrm{dw}} = \pm\pi/2$. In Fig. 1.3 we show two different types of domain walls.

Variation of the energy functional as given in Eq. (1.7) with respect to the above conditions leads to the differential equation

$$\left(\frac{d\theta_{\mathrm{dw}}(x)}{dx}\right)^2 = \frac{K_e}{J}\sin^2\theta_{\mathrm{dw}}(x), \tag{1.8}$$

where the characteristic length scale of the domain wall, its width $\lambda_{\mathrm{dw}} = \sqrt{J/K_e}$, appears. By separation of variables we integrate the square root of Eq. (1.8) from the center of the wall where $\theta_{\mathrm{dw}} = \pi/2$ to θ_{dw} at position x and obtain

$$\log\left[\tan\frac{\theta_{\mathrm{dw}}}{2}\right] = Q\lambda_{\mathrm{dw}}(x - r_{\mathrm{dw}}), \tag{1.9}$$

where the domain-wall charge $Q = \pm 1$ indicates the two possible solutions of the quadratic equation. Physically these two solutions correspond to an up-down or a down-up domain wall. Inversion of the above equation gives the solution

$$\theta_{\mathrm{dw}}(x) = 2\arctan\left[\exp\left(Q\frac{x - r_{\mathrm{dw}}}{\lambda_{\mathrm{dw}}}\right)\right], \tag{1.10}$$

that describes the one-dimensional domain wall. In the above discussion we did not need to specify orientation of the anisotropy-axes. Therefore the domain-wall solution holds for the different types of domain wall we specify now. When the hard-axis anisotropy is along the x-direction the corresponding domain walls will be of the Bloch type. When the hard-axis is perpendicular to the x-direction the domain wall is of the Néel type. Now that we have the static solution for domain walls we consider its dynamics. As discussed in the previous Section, the equation of motion for the magnetization is given by the LLG equation, which in slightly rewritten form is given by

$$\left(\frac{\partial}{\partial t} + \boldsymbol{v}_s\cdot\boldsymbol{\nabla}\right)\boldsymbol{m}(\boldsymbol{x},t) = -\gamma\mu_0\boldsymbol{m}(\boldsymbol{x},t)\times\boldsymbol{H}_{\mathrm{eff}} + \boldsymbol{m}(\boldsymbol{x},t)\times\left(\alpha_G\frac{\partial}{\partial t} + \beta\boldsymbol{v}_s\cdot\boldsymbol{\nabla}\right)\boldsymbol{m}(\boldsymbol{x},t), \tag{1.11}$$

where we have rewritten the spin-transfer torques of Eq. 1.2 using the spin velocity $\boldsymbol{v}_s = g\mu_B P\sigma\boldsymbol{E}/2M_s|e|$, which is proportional to the applied electric field. Since we are concerned here with the motion of the domain-wall structure we want to solve the equation of motion under the constraint that the wall moves without changing its shape. Thus we need to find equations of motion for the position $r_{\mathrm{dw}}(t)$ and central angle with the hard axis $\varphi_{\mathrm{dw}}(t)$. This can be done by substitution of the domain-wall solution into the free-energy functional and subsequently vary with respect to these parameters [11]. Note that also a dissipation functional is needed in this approach to be able to obtain the dissipative contributions to the equations of motion. An equivalent approach, known as the Thiele method [47], is to project the LLG equation as given by Eq. (1.11) onto the translational modes of the texture. Using this method we substitute the solution for the domain wall $\boldsymbol{m}_{\mathrm{dw}}$ into Eq. (1.11) and multiply the equation with either $\partial\boldsymbol{m}_{\mathrm{dw}}/\partial r_{\mathrm{dw}}$ or $\partial\boldsymbol{m}_{\mathrm{dw}}/\partial\varphi_{\mathrm{dw}}$ which are the generators of translation for the two coordinates. By subsequent integration over the coordinate along the strip we arrive at the equations of

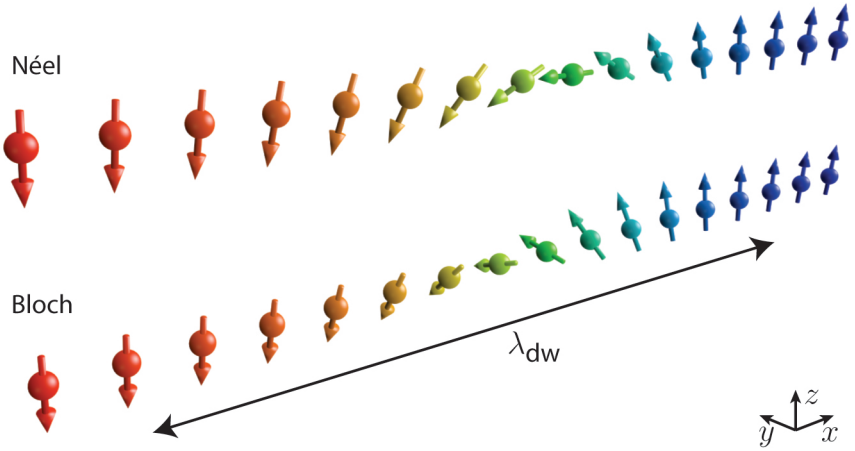

Figure 1.3: Illustration of a Néel wall and Bloch domain wall. The different configurations follow from the free-energy functional. For both walls the easy axis anisotropy is along the z-axis, thus in this figure $\theta_{\mathrm{dw}}(x)$ is the angle with the z-axis. For the Néel wall the hard axis is the y-axis and for the Bloch wall it is the x-axis. The other domain-wall angle φ_{dw} determines the angle of the central magnetic moment in the wall with the hard axis. The domain-wall width λ_{dw} is determined by the exchange stiffness and easy axis anisotropy. Both domain walls have the same charge, since they both turn from down to up as a function of position.

motion for these two conjugate variables [11]. The equations of motion are given by

$$\frac{\dot{r}_{\mathrm{dw}}}{\lambda_{\mathrm{dw}}} - \alpha_G Q \dot{\varphi}_{\mathrm{dw}} = Q\frac{K_h}{2\hbar}\sin 2\varphi_{\mathrm{dw}}(t) - \frac{v_s}{\lambda_{\mathrm{dw}}}; \tag{1.12}$$

$$\dot{\varphi}_{\mathrm{dw}} + \alpha_G Q \frac{\dot{r}_{\mathrm{dw}}}{\lambda_{\mathrm{dw}}} = -H_e + \beta Q \frac{v_s}{\lambda_{\mathrm{dw}}}, \tag{1.13}$$

where H_e is the magnetic field along the easy-axis of the anisotropy. We first eliminate $\dot{r}_{\mathrm{dw}}$ from the first equation and obtain an equation for the central domain-wall angle. This equation is given by

$$\dot{\varphi}_{\mathrm{dw}}(1+\alpha_G^2) = -H_e + Q(\alpha_G+\beta)\frac{v_s}{\lambda_{\mathrm{dw}}} - \alpha_G \frac{K_h}{2\hbar}\sin(2\varphi_{\mathrm{dw}}) \equiv -\frac{\partial V(\varphi_{\mathrm{dw}})}{\partial \varphi_{\mathrm{dw}}}, \tag{1.14}$$

where we defined the potential $V(\varphi_{\mathrm{dw}})$. This potential depends on a periodic part, coming from the anisotropy, that pushes the angle away from the hard axis and a driving force induced by the torques from applied external field along the easy axis and spin transfer. The resulting potential is a tilted washboard as shown in the insets in Fig. 1.4. The equation of motion for the angle has two qualitatively different solutions. When the driving forces do not tilt the washboard sufficiently the angle becomes time-independent and resides in a local minimum of the potential. When all local minima disappear due to strong tilting the motion of the angle becomes periodic, with a period set by the strength

of the anisotropy. We are mainly interested in the dynamics on larger timescales thus we consider the average motion of the domain wall. The equation of motion for the average velocity of the wall is given by

$$\alpha_G \frac{\langle \dot{r}_{\mathrm{dw}} \rangle}{\lambda_{\mathrm{dw}}} = -QH_e + \beta \frac{v_s}{\lambda_{\mathrm{dw}}} + Q\langle \dot{\varphi}_{\mathrm{dw}} \rangle. \tag{1.15}$$

Note that it is the dissipative spin torque that appears here together with the external applied field, illustrating the term field-like torque. Note that domain walls with opposite charge Q move in the same direction under the influence of the torque induced by the current, whereas they move in opposite directions due to the field along the easy axis H_e. This is crucial for the aforementioned racetrack memory. For a current-driven domain wall with charge $Q = 1$ the equations of motion result in the following expression for the average velocity of the domain wall

$$\frac{v_{\mathrm{dw}}}{\lambda_{\mathrm{dw}}} = \beta \frac{v_s}{\lambda_{\mathrm{dw}}} + \frac{1}{(1+\alpha_G^2)} \mathrm{sign}\left[(\alpha_G - \beta)\frac{v_s}{\lambda_{\mathrm{dw}}}\right] \mathrm{Re}\sqrt{\left((\alpha_G - \beta)\frac{v_s}{\lambda_{\mathrm{dw}}}\right)^2 - \left(\frac{v_c}{\lambda_{\mathrm{dw}}}\right)^2}, \tag{1.16}$$

where $v_c = \alpha_G \lambda_{\mathrm{dw}} K_h / 2\hbar$ is a critical velocity. In Fig. 1.4 we show this result for current driven domain-wall motion for different ratios of β/α_G which is crucial for the qualitative behavior of the domain-wall dynamics. When $\beta = 0$ the domain wall is intrinsically pinned up to Walker breakdown. Walker breakdown is reached at the cusps in Fig. 1.4 and corresponds to the point where the potential for the angle stops having local minima and the angle starts precessing. In Eq. (1.16) this corresponds to the point where the argument of the square root becomes positive.

Some domain-wall structures are inherently not one-dimensional such as vortex domain walls, see Fig. 1.5, which were observed in soft magnetic materials [48, 49]. The vortex configuration is stabilized by the magnetostatic energy. Another example is the transverse domain wall. We can think of a transverse domain wall as two half-vortices with opposite charge on the sides of the ferromagnetic strip [50].

Like a one-dimensional domain wall, a magnetic vortex is a topological structure, which means it cannot be deformed continuously into another state with different topological properties such as an homogeneous magnetization. Vortices can be characterized by its polarization $p = \pm 1$ which is the direction of the magnetization at the center $\boldsymbol{X}_v = (X(t), Y(t))$ of the vortex and the vorticity $q = \pm n$, where n is an integer, which specifies the number and orientation of windings around the vortex core. In Fig. 1.5 we have a vortex domain wall where the vortex core is characterized by a central moment pointing out of the plane and a clockwise winding around it. Textures with different topology can be classified using topological invariants, such as the Euler characteristic χ_{E} that one can use to distinguish donuts ($\chi_{\mathrm{E}} = 0$) and balls ($\chi_{\mathrm{E}} = 2$) mathematically. For magnetic textures we use the winding or skyrmion number W that measures how many times the structure covers the sphere. For two-dimensional textures the winding number is defined as

$$W = \int \frac{dxdy}{4\pi} \boldsymbol{m} \cdot \left(\frac{\partial \boldsymbol{m}}{\partial x} \times \frac{\partial \boldsymbol{m}}{\partial y}\right), \tag{1.17}$$

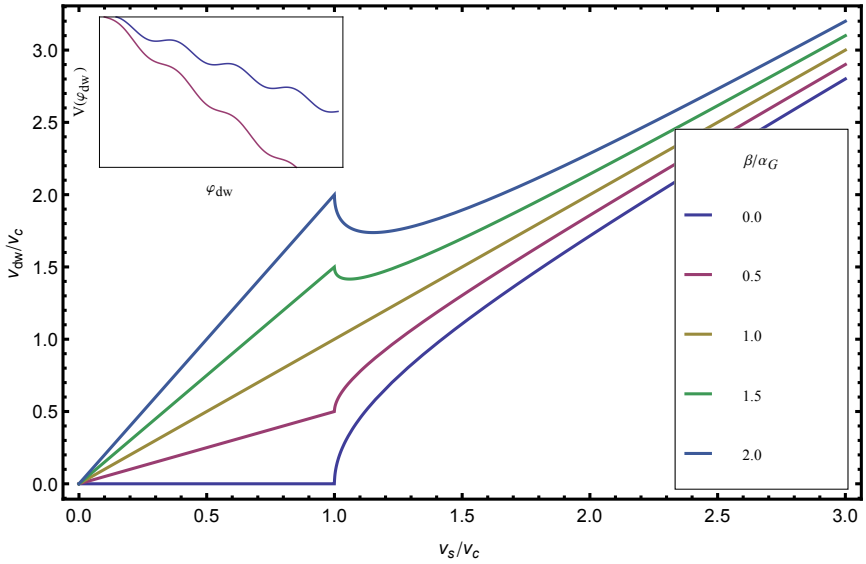

Figure 1.4: The velocity of the domain wall as a function of the spin velocity that scales linearly with the electric current for various ratios of β/α_G. At the critical velocity the internal angle of the domain wall starts precessing. In the inset we show the potential energy for the central angle of the domain wall. Below Walker breakdown the angle is fixed in a local minimum of the potential, when the energy is further tilted by the application of a current local minima cease to exist and the angle starts precessing. When $\beta = 0$ the domain wall only moves above the critical velocity. In the special case that the reactive and dissipative adiabatic spin tranfer torques are equal, *i.e.*, $\alpha_G = \beta$, the velocity depends linear on the applied current, however, even in this case there is a transition at the critical velocity where the central angle begins to precess.

The winding number of a single vortex is given in terms of its charge and vorticity, $W = pq/2$ which is half-integer valued because the magnetization is in-plane far away from the vortex core, and is independent of the precise form of the texture. The dynamics of the vortex walls, or isolated vortices in magnetic disks is different from one-dimensional domain-wall motion. A crucial difference is the absence of the intrinsic pinning associated with the central angle φ_{dw}. This allows for domain walls with a higher mobility. In the discussion of the one-dimensional walls we observed that the position and angle coordinates form a conjugate pair. For a vortex the two components of the vector denoting its position in the plane $\boldsymbol{X}_v(t)$ are conjugate. We use the Thiele method to find the equation of motion for the central position induced by an external field $\boldsymbol{H}$ and obtain

$$\left(\dot{\boldsymbol{X}} - \boldsymbol{v}_s\right) \times \boldsymbol{G} = \mu_0 \boldsymbol{H} - \alpha_G D \cdot \left(\dot{\boldsymbol{X}} - \frac{\beta}{\alpha_G}\boldsymbol{v}_s\right), \tag{1.18}$$

where the gyrovector $\boldsymbol{G} = 4\pi W/a^3 \boldsymbol{e}_z$ is related to the winding number of the vortex that is quantized and a^3 is the volume of the unit-cell of the lattice, the dissipative matrix is

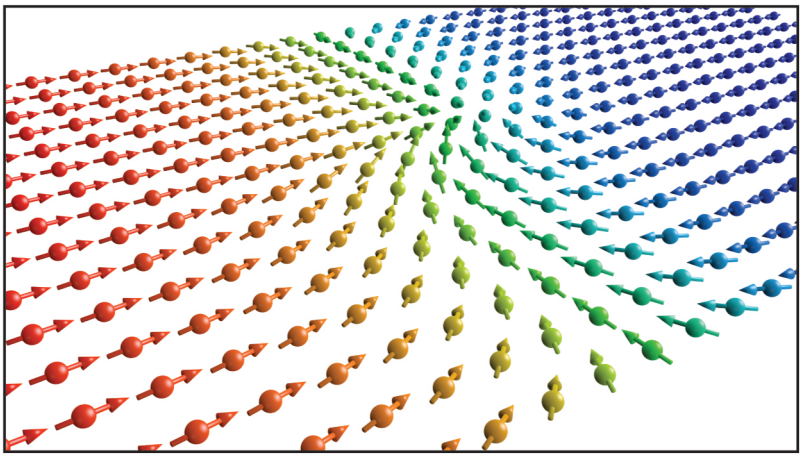

Figure 1.5: Illustration of a head-to-head vortex domain wall. In the core of the vortex the magnetization points out of the plane around it there is a clockwise winding of the magnetic moments. This defines the topology of the vortex.

not topological and given by

$$D^{ij} = \int d\boldsymbol{x} \left(\frac{\partial \boldsymbol{m}}{\partial x^i} \cdot \frac{\partial \boldsymbol{m}}{\partial x^j} \right). \tag{1.19}$$

The gyrovector points perpendicular to the plane which leads to a transverse response of the vortex to an applied force. Driven motion of magnetic vortices is explored in various works using AC driving fields leading to a rotating vortex [51–55] on a magnetic disk or motion through a wire [25, 56–60] and also spin pumping by vortices was investigated [61, 62].

Recently perpendicular magnetic anisotropy (PMA) structures received a lot of interest due to their promising technological applications. In these PMA structures the interaction between the ferromagnetic layer and the surrounding materials in the multilayer structure induce a strong easy axis anisotropy perpendicular to the plane, creating very narrow domain walls.

In these PMA multilayers other mechanisms that drive domain walls are starting to be explored. Since most of the PMA structures involve Pt layers the role of SO coupling is being investigated. The heavy element Pt shows a strong SO coupling that leads to the spin Hall effect [63]. This effect leads to the injection of a spin current into the ferromagnetic layer perpendicular to the current and interface normal which we take to be in the z direction, $\boldsymbol{j}_s \propto \boldsymbol{j}_c \times \boldsymbol{e}_z$. These injected spins then transfer their angular momentum to the ferromagnet, leading to a Slonczewski torque on the magnetization, $\boldsymbol{\tau} \propto \boldsymbol{m} \times \boldsymbol{j}_s \times \boldsymbol{m}$. Another interesting aspect of these multilayers structures is the breaking of structural inversion symmetry by the inequivalence of the bottom and top layers surrounding the ferromagnetic layer, or near the interface. Inversion asymmetry leads to Dzyaloshinskii-Moriya (DM) interactions [64, 65] that favor chiral ordering of

the magnetization, which we discuss further in the next Section. For domain walls the DM interactions imply a preferred sense of rotation, therefore they are called chiral domain walls. In PMA structures the symmetry breaking due to DM interactions lifts the degeneracy of the central angle $\varphi_{\mathrm{dw}} = \pm\pi/2$, leading to Néel walls that can be manipulated by the torque induced by the spin Hall effect [66–68].

In addition to the DM interactions caused by the symmetry breaking, there can be other mechanisms at work as well. In semiconductor spintronics breaking of inversion symmetry is known to lead to torques originating in SO coupling of the carriers. Recently these torques were also proposed to exist in the inversion symmetry breaking samples of PMA stacks [32]. In Sec. 1.3 we introduce SO coupling and in the following chapters we consider these torques in detail.

1.2.2 Chiral magnets

In the last part of the previous Section we discussed structures where the structural inversion symmetry is broken. For some materials this symmetry is broken by the crystal structure. For systems with broken inversion symmetry DM terms like $D_{abc}m^a\nabla_b m^c$ can be added to the free energy given in Eq. (1.7). The precise form of D_{abc} depends on the microscopic mechanisms involved, and depends on SO coupling in addition to the breaking of inversion symmetry.

When we consider the DM contribution $\boldsymbol{m}\cdot(\boldsymbol{\nabla}\times\boldsymbol{m})$ to the free energy the ground state of the system no longer is given by the homogeneous alignment with the external field but rather by the conical magnetic texture

$$\boldsymbol{m}_{\mathrm{con}}(\boldsymbol{x}) = \begin{pmatrix} \sin\theta\cos(\boldsymbol{q}\cdot\boldsymbol{x}) \\ \sin\theta\sin(\boldsymbol{q}\cdot\boldsymbol{x}) \\ \cos\theta \end{pmatrix}, \tag{1.20}$$

where the pitch vector $\boldsymbol{q}$ is parallel to the external field, with $|\boldsymbol{q}| = D/J$ and the angle $\theta = \arccos H_e J/3D^2$. This result interpolates between a helical magnetization for $H_e = 0$ via a conical magnetization for $H_e \approx 3D^2/J$ to a state where the magnetization aligns with the applied field for $H_e \to \infty$.

For the chiral, itinerant ferromagnet manganese silicide (MnSi) a different ground state structure was discovered in 2009. In the presence of an external field close to the critical temperature a skyrmion lattice turns out to be the ground state texture [69]. To a good approximation the skyrmion lattice is given by

$$\boldsymbol{m}(\boldsymbol{x},t) = M_c\boldsymbol{m} + \sum_{i=3} M_{\mathrm{hel}}\boldsymbol{m}_{\mathrm{hel}}(\boldsymbol{q}_j\cdot\boldsymbol{x} + \phi_j), \tag{1.21}$$

which is the sum of a constant magnetization in the direction of the external field and three helical magnetizations with the same amplitude and pitch vectors in the plane perpendicular to the external field that satisfy $\boldsymbol{q}_1 + \boldsymbol{q}_2 + \boldsymbol{q}_3 = \boldsymbol{0}$. In Fig. 1.6 a single skyrmion is shown. Skyrmions were introduced as a field configuration for pions by Skyrme[70] as a model for nucleons. The field configuration for skyrmions looks similar

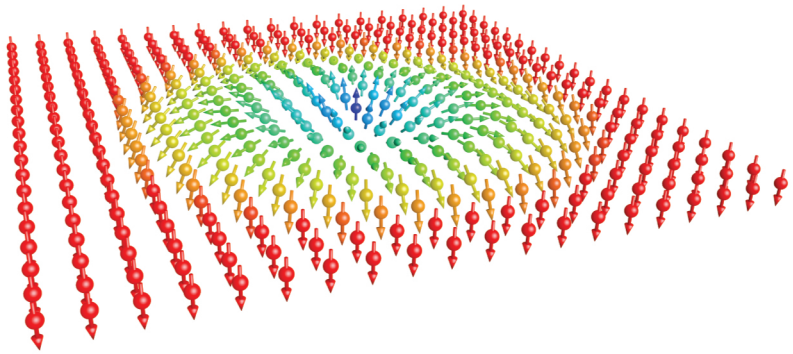

Figure 1.6: Illustration of a single skyrmion. Note the difference with the vortex core of the domain wall shown in Fig. 1.5. For a vortex the magnetization direction changes from perpendicular to the plane towards in plane as you go from the vortex core to infinity. For the skyrmion the magnetization rotates 180 degrees.

to that of magnetic vortices (see Fig. 1.5). We can think of a vortex as half a skyrmion since the winding number for a skyrmion, introduced in Eq.(1.17), is given by $W = pq$, which is integer-valued. The current-induced dynamics of the skyrmion lattice is similar to the dynamics of the vortices.

1.3 Spin-orbit coupling

In the above discussions we already encountered the notion of SO coupling. In this Section we introduce some of the basic notions of SO coupling that are relevant for this Thesis. SO coupling appears as a first-order correction in $(v/c)^2$ in the nonrelativistic approximation to the Dirac equation[71] it is given by the Pauli equation

$$H_{\mathrm{SO}} = \frac{\hbar}{4m^2c^2}\boldsymbol{p}\cdot(\boldsymbol{\sigma}\times\boldsymbol{\nabla}V)\,, \tag{1.22}$$

where $\boldsymbol{\nabla}V$ is the gradient of the potential energy and $\boldsymbol{\sigma}$ is the vector of Pauli matrices. This term can be understood by semi-classical arguments as well, which offer a more intuitive understanding of SO coupling.

In this context, it is interpreted as the sum of the Larmor and Thomas precession. The Larmor contribution can be understood by considering an electric field, for example of the nucleus, in the rest frame of a moving electron. In the rest frame of the electron the electric field results in an magnetic field as a consequence of the Lorentz boost between the static and comoving frame. This resulting magnetic field $\boldsymbol{B}_{\mathrm{SO}} = -\boldsymbol{p}\times\boldsymbol{\nabla}V/m_ec$ couples via the Zeeman interaction to the magnetic moment of the electron spin resulting in twice of that in Eq. (1.22). The overestimation of the SO coupling is due to fact that

we did not account for the Thomas precession which results in a SO coupling that is the opposite and half of the Larmor contribution [71, 72].

In condensed-matter theory we are dealing not with the field of a single nucleus but usually with a periodic arrangement of ions in a lattice. In such lattices the dynamics of electrons are described using Bloch states. Since only the electrons near the Fermi surface contribute to transport we write an effective Hamiltonian describing SO coupling,

$$H_{\mathrm{SO,eff}} = -\boldsymbol{\Omega}(\boldsymbol{k}) \cdot \boldsymbol{\sigma}, \tag{1.23}$$

where $\boldsymbol{\Omega}(\boldsymbol{k})$ is a momentum dependent vector-valued function. Here, we have assumed that two bands contribute. The Pauli matrices $\boldsymbol{\sigma}$ act in this internal space. The allowed form of $\boldsymbol{\Omega}(\boldsymbol{k})$ is governed by the symmetries of the system. For systems with time-reversal symmetry we have for a two-level system $\boldsymbol{\Omega}(\boldsymbol{k}) = -\boldsymbol{\Omega}(-\boldsymbol{k})$, since both (crystal) momentum and spin change sign under time reversal, *i.e.* $\boldsymbol{k} \to -\boldsymbol{k}$ and $\boldsymbol{\sigma} \to -\boldsymbol{\sigma}$. Inversion symmetry implies $\boldsymbol{\Omega}(\boldsymbol{k}) = \boldsymbol{\Omega}(-\boldsymbol{k})$. Together these symmetries result in $\boldsymbol{\Omega}(\boldsymbol{k}) = \boldsymbol{0}$. This means that in systems exhibiting both time-reversal and inversion symmetry we cannot have SO coupling of the form of Eq. (1.23). However, when inversion symmetry is broken we can, up to first order in $\boldsymbol{k}$, write

$$H_{\mathrm{SO}} = \lambda_{\mathrm{D}} \left(k_x \sigma_x - k_y \sigma_y\right) + \lambda_{\mathrm{R}} (\boldsymbol{k} \times \boldsymbol{e}_{\mathrm{as}}) \cdot \boldsymbol{\sigma}. \tag{1.24}$$

The first term is called (linear) Dresselhaus SO coupling[73]. The second term comes from inversion symmetry breaking in the direction $\boldsymbol{e}_{\mathrm{as}}$ and is called the Bychkov-Rashba or Rashba SO coupling[74, 75]. Note that Rashba SO coupling has the form of Eq. (1.22) where the electric field points in the symmetry breaking direction.

1.4 This Thesis

This Thesis is organised as follows. In Chapter 2 we consider a semi-classical model to get a phenomenological understanding of the effects considered throughout this Thesis.

In Chapter 3 we consider the combined effect of SO coupling and gradients in the magnetization direction. Via symmetry arguments we predict that much more torques are allowed by the symmetry of the system than the torques linear in the gradients of the magnetization or SO coupling alone. Furthermore we use the Boltzmann equation to calculate spin torques in the Rashba ferromagnet up to second order in SO coupling strength. We then compute the consequences of these new torques for the motion of various types of domain walls.

In Chapter 4 the effects of electric fields and thermal gradients on the currents and dynamics of the magnetization are studied using a diagrammatic approach. We discuss the subtraction procedure that is needed to remove unphysical divergences in the zero temperature limit for the thermal linear response coefficients. In the last part of this Section we apply the insights about the linear response coefficients to propose a ferromagnetic resonance experiment capable to determine the size of the calculated parameters using dissipation in the magnet.

In Chapter 5 we propose a new mechanism of spin injection into a paramagnetic metallic layer by means of a ferromagnet with a gradient in the magnetization. We show, using scattering theory, that a current through a magnetic texture leads to the injection of a pure spin current into an adjacent metallic layer. The direction of spin polarization is given by $\boldsymbol{m} \times (\boldsymbol{j}_c \cdot \nabla)\boldsymbol{m}$. Then we calculate the strength of this effect when it is measured using the inverse spin Hall effect. Subsequently we show that the ejection of a pure spin current from the ferromagnet causes spin torques that result in renormalized values of the α_G and β parameters. As we discussed in the introduction this ratio is of crucial importance for the qualitative response of the current driven domain wall.

In Chapter 6 we study domain-wall motion using computer simulations. Using the Ising model of ferromagnetism with random bond disorder we study field driven motion of a domain wall. In this systems for very low field strengths the velocity of the domain walls depends nonlinearly on this applied field.

Chapter 2

Toy model

In this Section we consider a semi-classical toy model to understand the interaction between spin-polarized currents and magnetic textures. The merits of this rather crude model are that it provides a clear physical picture and allows for an intuitive introduction of the relevant phenomena. We study classical electrons with a a classical spin direction $\boldsymbol{s}$. The coupling between the spin of these classical electrons and the magnetization is ferromagnetic. The model is the classical analog of the s-d model for ferromagnetism. In this model the magnetization and the spins of the electrons correspond to localized (d-wave) moments and mobile, or conducting, (s-wave) electrons, hence the name s-d model. The s-d model is accurate for diluted ferromagnetic semiconductors like $\mathrm{Ga_{1-x}Mn_xAs}$ where there is a clear separation between conducting electrons and localized states contributing to the ferromagnetism. For most transition metals this description is rather inaccurate due to the hybridization between different bands. For those systems the Stoner model of ferromagnetism would be a more accurate starting point. We use the s-d model since it allows for easy physical interpretation and leads to qualitatively correct results.

The semi-classical approach is adequate provided we are not interested in effects depending on the phase coherence of the constituents, such as localization. This enables us to use the Boltzmann equation to study transport properties and long wavelength magnetization dynamics. The equations of motion for the classical electrons which we derive after we make the adiabatic approximation are similar to the semi-classical results by Sundaram and Niu [76] who studied the equations of motion for the average position and momentum $\{\boldsymbol{r}_c, \boldsymbol{k}_c\}$ of wave packets of Bloch states in a single band. Tserkovnyak and Wong also obtained similar equations of motion for semi-classical degrees of freedom by using a quantum kinetic equation [42].

The Hamiltonian for the electrons takes the rather simple form

$$\mathcal{H}_{sd} = \frac{\boldsymbol{p}^2}{2m} - \Delta \boldsymbol{m}[\boldsymbol{q}(t), t] \cdot \boldsymbol{s}, \tag{2.1}$$

and consists of a kinetic part and the s-d coupling between the magnetization direction $\boldsymbol{m}$ and spin direction of the electron $\boldsymbol{s}$, the strength of the coupling between the spin and magnetization direction is given by Δ. The equations of motion for the electrons are

given by

$$\dot{\boldsymbol{q}} = \frac{\partial \mathcal{H}_{sd}}{\partial \boldsymbol{p}}, \tag{2.2}$$

$$\dot{\boldsymbol{p}} = -\frac{\partial \mathcal{H}_{sd}}{\partial \boldsymbol{q}}, \tag{2.3}$$

$$\dot{\boldsymbol{s}} = -\frac{1}{\hbar}\boldsymbol{s} \times \frac{\partial \mathcal{H}_{sd}}{\partial \boldsymbol{s}}, \tag{2.4}$$

where $\dot{\boldsymbol{q}}$ is the velocity of the electron. In addition to these equations of motion we also have the equation of motion for the magnetization dynamics as given by

$$\dot{\boldsymbol{m}} = -\gamma\mu_0 \boldsymbol{m} \times \boldsymbol{H}_{\text{eff}} + \alpha_G \boldsymbol{m} \times \dot{\boldsymbol{m}} + \frac{\Delta}{\hbar}\boldsymbol{m} \times \boldsymbol{s}\delta(\boldsymbol{x} - \boldsymbol{q}(t)), \tag{2.5}$$

where the first two terms are introduced in the previous Section and represent the dynamics of the magnetization in the absence of the electrons. The last term represents the torque due to a single electron with spin $\boldsymbol{s}$, which therefore only acts at the electron position $\boldsymbol{q}(t)$. Spin torques can be calculated from the induced average spin direction (see Chapter 3). In this Section we focus on spin motive forces and spin pumping.

Without the coupling of the spin to the magnetization or with a homogeneous magnetization the above equations of motion for the electrons are trivial, but the coupling to the texture leads to interesting dynamics. In the next Section we eliminate the spin dynamics and consider its effect on the motion of the electrons.

2.1 Adiabatic approximation

In this Section we make an adiabatic approximation for the spin dynamics of the electrons to obtain the corrections for the equations of motion of the position and momentum of the electrons. In order to be more general we add a dissipative term to the spin dynamics

$$\frac{d\boldsymbol{s}}{dt} = \frac{\Delta}{\hbar}\boldsymbol{s} \times \boldsymbol{m} - \frac{\alpha\Delta}{\hbar}\boldsymbol{s} \times (\boldsymbol{s} \times \boldsymbol{m}), \tag{2.6}$$

which leads to damped precessional motion of the spin around the (local) magnetization. We introduced a dimensionless damping parameter α that phenomenologically describes relaxation of the spin of the electron and is similar to the Gilbert damping of the magnetization. The time and length scales for the electron spin dynamics are much shorter than those of the magnetization. Therefore we can use an adiabatic approximation to describe the dynamics of the spin degree of freedom. We solve the dynamics of the spin degree of freedom up to first order in time derivatives and obtain two solutions, for the majority (+) and minority (-) electrons. The solutions are given by

$$\boldsymbol{s}_{\pm} = \pm\boldsymbol{m} \pm \frac{\hbar}{\Delta}\frac{d\boldsymbol{m}}{dt} \times \boldsymbol{m} - \frac{\hbar\alpha}{\Delta}\frac{d\boldsymbol{m}}{dt}, \tag{2.7}$$

The first term on the right-hand side of the equation describes the adiabatic alignment of the spin to the magnetic texture. The other terms follow from dynamics of the magnetic

texture or the motion of the spin through the texture due to the motion of the electron. These correction terms result in induced spin densities perpendicular to the local direction of magnetization. Note that the total time derivative of the magnetization should be taken with respect to the motion of the electron, thus

$$\frac{d\boldsymbol{m}}{dt} \equiv \frac{\partial \boldsymbol{m}}{\partial t} + (\dot{\boldsymbol{q}} \cdot \nabla)\boldsymbol{m}(\boldsymbol{x}, t). \tag{2.8}$$

We can use the first-order solutions for the spin dynamics to determine the effect of an inhomogeneous and/or time-dependent magnetic texture and, in particular, to determine the forces it induces on the electron by substitution of the solutions for the spin dynamics into Eq. (2.3) which leads to the forces

$$\begin{aligned} F^i_{\mathrm{smf}\pm} &= \Delta \frac{\partial \boldsymbol{m}}{\partial x^i} \cdot \boldsymbol{s}_\pm \\ &= \pm\hbar \left[\left(\frac{\partial \boldsymbol{m}}{\partial x^i} \times \frac{\partial \boldsymbol{m}}{\partial t} \right) \cdot \boldsymbol{m} + \dot{x}^j \left(\frac{\partial \boldsymbol{m}}{\partial x^i} \times \frac{\partial \boldsymbol{m}}{\partial q^j} \right) \cdot \boldsymbol{m} \right] \\ &\quad -\alpha\hbar \left[\frac{\partial \boldsymbol{m}}{\partial x^i} \cdot \frac{\partial \boldsymbol{m}}{\partial t} + \dot{x}^j \frac{\partial \boldsymbol{m}}{\partial x^i} \cdot \frac{\partial \boldsymbol{m}}{\partial x^j} \right]. \end{aligned} \tag{2.9}$$

The terms proportional to α are dissipative, the other terms are reactive. We can compare these expressions to the results for the spin motive forces we derived in the introduction using Onsager's reciprocity relations, as given in Eq. (2.9). It is clear that we obtain terms with the same form for this simple semi-classical model. Note that in Eq. (1.6) we worked in the thermodynamic limit and related the magnetization dynamics to the current, whereas we here only considered the influence on a single particle. In addition to the spin motive forces already considered in Eq. (1.6) we also find two additional contributions proportional to the velocity of the electron. We return to their meaning in Sec. 2.3. The spin transfer torques can be obtained in a similar way by considering the equation of motion for the magnetization and subsequently making the same substitution of the first-order solutions for the spin dynamics as given in Eq. (3.18). In this Section we derived the spin motive forces by solving the equation of motion for the dynamics of the spin degree of freedom by using an adiabatic approximation. In the next Section we make the same approximation but then on the level of the Lagrangian. In that way the relation with the Berry phase is more manifest and we elegantly obtain the effective magnetic and electric fields induced by the spin Berry phase. However, the derivation presented in this Section gives a nice physical intuition for the origin of the spin transfer torques and spin motive forces in these systems. It is also more straightforward to incorporate strong SO coupling into the adiabatic approximation at the level of the equations of motion, because we avoid problems with higher time derivatives in the Lagrangian.

2.2 Relation with the spin Berry phase

Although it may not be clear from the semi-classical description introduced in the previous Section, the spin motive forces are related to the spin Berry phase[27]. In this Section

we elucidate this relationship. The equation of motion for the spin of the electron as given in Eq. (2.4) is the classical counterpart of the SU(2) algebra of the spin-operators. This equation can be obtained from the Lagrangian

$$\mathcal{L}_s = \hbar \frac{d\boldsymbol{s}}{dt} \cdot \boldsymbol{A}_s(\boldsymbol{s}) + \Delta \boldsymbol{m} \cdot \boldsymbol{s}, \tag{2.10}$$

where $\boldsymbol{A}_s(\boldsymbol{s})$ is the vector potential of a monopole, which satisfies $\boldsymbol{\nabla}_s \times \boldsymbol{A}_s = \boldsymbol{s}$. The Euler-Lagrangian equations of motion for the spin read

$$\frac{d}{dt}\left(\frac{\partial \mathcal{L}_s}{\partial \dot{\boldsymbol{s}}}\right) - \frac{\partial \mathcal{L}_s}{\partial \boldsymbol{s}} = 0, \tag{2.11}$$

which results in the classical equation of motion for the spin degree of freedom as given in Eq. (2.4). The Euler-Lagrange equations describe the paths through phase space that correspond to stationary points of the action, which is the integral over time of the Lagrangian. The integral over time of the first term introduced in Eq. (2.10), which is called the kinetic term, can be represented as

$$\int_{t_0}^{t_f} dt \hbar \dot{\boldsymbol{s}} \cdot \boldsymbol{A}_s = \hbar \int_{\partial A} d\boldsymbol{l} \cdot \boldsymbol{A}_s = \hbar \int_A d\boldsymbol{s} \cdot \boldsymbol{s},$$

which measures the area A, with boundary ∂A, on the unit sphere enclosed by the path between $\phi_0 \equiv \phi(t_0)$ and ϕ_f. Note that we have a gauge degree of freedom in the definition of $\mathcal{A}_s$. This shows that the phase from the kinetic term only depends on the enclosed area and does not depend on the parameterization or time-dependence of the path along the boundary, indicating that it is the geometry of the adiabatic parameter, in this case the spin, that matters. This geometric factor is called the spin Berry phase factor.

In order to obtain the spin motive forces, as given in Eq. 2.9, we used the first-order solution in time-derivatives of the spin equation of motion. An elegant way to obtain the spin motive forces using the Lagrangian description of the problem is by making the adiabatic approximation on the level of the Lagrangian. Thus, we let the spin degree of freedom follow the local direction of the magnetization, thus we make the substitution $\boldsymbol{s}(t) \to \boldsymbol{m}(\boldsymbol{q}(t), t)$, where $\boldsymbol{q}(t)$ is the position of the electron carrying the spin. This gives us for an adiabatically slow, with respect to the spin degree of freedom, moving spin through a texture the spin Berry phase contribution

$$\int_{t_0}^{t_f} dt \hbar \dot{\boldsymbol{s}} \cdot \boldsymbol{A}_s[\boldsymbol{s}] \to \int_{t_0}^{t_f} dt \hbar \frac{d\boldsymbol{m}(\boldsymbol{q}, t)}{dt} \cdot \boldsymbol{A}_s[\boldsymbol{m}(\boldsymbol{q}, t)], \tag{2.12}$$

The comoving derivative that is implied in the total time derivative, *i.e.*, $(\dot{\boldsymbol{q}} \cdot \boldsymbol{\nabla})\boldsymbol{m}(\boldsymbol{q}, t)$, gives rise to an effective electromagnetic potential that is induced by the motion of the spin through the magnetic texture. Below we investigate this matter further.

In the semi-classical model that we work with in this Section the adiabatic response of the system can be obtained by substituting $\boldsymbol{s}(t) \to \boldsymbol{m}(\boldsymbol{q}(t), t)$ in the classical Lagrangian as given in Eq. (2.10). The full Lagrangian for the electron carrying a majority spin

after this substitution is then given by

$$\mathcal{L} = \hbar \frac{\partial \boldsymbol{m}}{\partial t} \cdot \boldsymbol{A}_s \left[\boldsymbol{m}(\boldsymbol{q},t)\right] + \dot{q}^i \left. \frac{\partial \boldsymbol{m}}{\partial x^i} \cdot \boldsymbol{A}_s \left[\boldsymbol{m}(\boldsymbol{q},t)\right] \right|_{\boldsymbol{x}=\boldsymbol{q}(t)} - \frac{m\dot{\boldsymbol{q}}^2}{2} + M, \tag{2.13}$$

This Lagrangian yields the spin motive forces as given in Eq. 2.9. Since we eliminated the spin direction of the particle we are left with a spinless electron interacting with effective scalar and vector potential. The effective vector potential couples to the velocity of the electron just as the electromagnetic vector potential. We recognize the scalar and vector potentials

$$V_{\text{eff}}(\boldsymbol{q},t) = \frac{\partial \boldsymbol{m}}{\partial t} \cdot \boldsymbol{A}_s[\boldsymbol{m}(\boldsymbol{q},t)] \quad ; \quad \boldsymbol{A}_{\text{eff}}(\boldsymbol{q},t) = \left. \frac{\partial \boldsymbol{m}}{\partial \boldsymbol{x}} \cdot \boldsymbol{A}_s[\boldsymbol{m}(\boldsymbol{x},t)] \right|_{\boldsymbol{x}=\boldsymbol{q}}. \tag{2.14}$$

From the Lagrangian given in Eq. (2.13) we find the reactive spin motive forces as given in Eq. (2.9), which can be written in the form of an effective Lorentz force

$$\dot{\boldsymbol{p}} = -|e| \left(\boldsymbol{E}_{\text{eff}} + \dot{\boldsymbol{q}} \times \boldsymbol{B}_{\text{eff}}\right), \tag{2.15}$$

where the effective electric field $\boldsymbol{E}_{\text{eff}} = -\nabla_{\boldsymbol{q}} V_{\text{eff}}(\boldsymbol{q}) - \partial_t \boldsymbol{A}_{\text{eff}}$ and effective magnetic field $\boldsymbol{B}_{\text{eff}} = \nabla_{\boldsymbol{q}} \times \boldsymbol{A}_{\text{eff}}$, are explicitly given by

$$E^i_{\text{eff}} = \frac{\hbar}{|e|} \left(\frac{\partial \boldsymbol{m}}{\partial x^i} \times \frac{\partial \boldsymbol{m}}{\partial t} \right) \cdot \boldsymbol{m}, \tag{2.16}$$

and

$$B^i_{\text{eff}} = \frac{\hbar}{|e|} \frac{\epsilon^{ijk}}{2} \left(\frac{\partial \boldsymbol{m}}{\partial x^i} \times \frac{\partial \boldsymbol{m}}{\partial x^j} \right) \cdot \boldsymbol{m}. \tag{2.17}$$

Note that the strength of the effective electromagnetic fields depends on $\hbar/|e|$ and that they have opposite signs for majority and minority electrons.

In the previous Section we also considered dissipative contributions. We can introduce dissipation via the dissipation function. The dissipation function leading to spin relaxation in Eq. (2.6) is given by $\mathcal{W} = \alpha \dot{\boldsymbol{s}}^2/2$ which for the adiabatic approximation becomes

$$\mathcal{W} = \frac{\alpha}{2} \left(\frac{\partial \boldsymbol{m}}{\partial t} + (\dot{\boldsymbol{q}} \cdot \boldsymbol{\nabla}) \boldsymbol{m} \right)^2. \tag{2.18}$$

The Euler-Lagrange equations including dissipation are of the form

$$\frac{d}{dt} \left(\frac{\delta \mathcal{L}}{\delta \dot{\boldsymbol{q}}} \right) - \frac{\delta \mathcal{L}}{\delta \boldsymbol{q}} = \frac{\delta \mathcal{W}}{\delta \dot{\boldsymbol{q}}}, \tag{2.19}$$

where we explicitly stated the equation of motion depending on the coordinate $\boldsymbol{q}$, similar equations hold for the momentum and magnetization. Note that the substitution of $\boldsymbol{s}(t) \to \boldsymbol{m}(\boldsymbol{q}(t),t)$ in the dissipation functional leads, by taken the functional derivative with respect to $\partial \boldsymbol{m}/\partial t$, to the adiabatic dissipative spin transfer torques to which the β parameter is associated. This shows again how intimately spin-motive forces and spin transfer torques are related.

Note that we do not have an equation of motion for the spin degree of freedom anymore. Therefore the calculation of the spin density within the approach sketched in this Section is not as straightforward as it was using the equation of motion approach we took previously. In addition to this, it is good to note that by making the approximation $\boldsymbol{s} \to \boldsymbol{m}$ we effectively reduced the dimensionality of the phase space of the system. In our discussion of the effects of the inclusion of strong SO coupling into the above framework we return to this matter. Here we continue by discussing the effective electric and magnetic fields induced by the Berry phase obtained by the spin.

2.3 Spin-transfer torques, spin motive forces and the topological Hall effect

In the previous Section we obtained the forces on conduction electrons induced by a magnetic texture. In the above discussions we were occupied by the dynamics of a single particle following the magnetization adiabatically. In this Section we connect the single-particle results to the spin transfer torques and spin motive forces we introduced in the previous Chapter when we discussed linear response theory. In order to get from single particle results to expressions for thermodynamic systems we use the Boltzmann approach. Therefore we need to introduce the phase space distribution function $f(\boldsymbol{p}, \boldsymbol{q}, \boldsymbol{s}, t)d\boldsymbol{p}d\boldsymbol{q}d\boldsymbol{s}$ that represents the amount of particles in an infinitesimal piece of phase space. In the above Sections we have considered purely classical dynamics. For the equilibrium distribution of the electrons we take the Fermi-Dirac distribution which makes our discussion truly semi-classical from this point onwards. After the adiabatic approximation our distribution function we have

$$\int f(\boldsymbol{p}, \boldsymbol{q}, \boldsymbol{s}, t)d\boldsymbol{p}d\boldsymbol{q}d\boldsymbol{s} \to \sum_{\sigma=\pm} \int f_\sigma(\boldsymbol{p}, \boldsymbol{x}, t)d\boldsymbol{p}d\boldsymbol{q},$$

where $f_\sigma(\boldsymbol{p}, \boldsymbol{q}, t)$ is the distribution function for the two spin states. The dynamics of the distribution of particles in phase-space is governed by the Boltzmann equation

$$\frac{\partial f}{\partial t} + \dot{\boldsymbol{q}} \cdot \frac{\partial f}{\partial \boldsymbol{q}} + \dot{\boldsymbol{p}} \cdot \frac{\partial f}{\partial \boldsymbol{p}} = I_{\text{coll}}[f], \tag{2.20}$$

where $I_{\text{coll}}[f]$ is the collision integral describing inter-particle collisions or collisions with impurities in the material. Using the Boltzmann equation we can obtain expression for the transport coefficients and spin transfer torques of the system. In the next Chapter we use this approach to calculate the spin torques for a Rashba ferromagnet. There we use the distribution function to calculate the average induced spin density. Here we would like to stress again that majority and minority electrons feel opposite effective fields. This shows why all expressions we introduced in the previous Section are proportional to the polarization P of the ferromagnet.

To illustrate this we consider the electromotive force induced by a moving domain wall [17, 61]. For the one-dimensional domain wall we introduced before, only two terms

in the equation of the spin motive forces [see Eq. (2.9)] are nonzero. The effective magnetic field and the dissipative contribution involving two spatial derivatives vanish because the domain-wall profile depends on a single coordinate. The forces on electrons with majority and minority spins come from the effective electric field and dissipative force and are given by

$$\pm F^i = \frac{\hbar}{2}\left[\boldsymbol{m}\cdot\left(\frac{\partial \boldsymbol{m}}{\partial t}\times\frac{\partial \boldsymbol{m}}{\partial x^i}\right)+\beta\left(\frac{\partial \boldsymbol{m}}{\partial t}\cdot\frac{\partial \boldsymbol{m}}{\partial x^i}\right)\right], \tag{2.21}$$

where we restored the β parameter for the dissipative contribution which depends on more dissipative processes than the spin relaxation we introduced above. For a slowly moving and wide domain wall we may assume that the steady state distribution of the electrons is given by $f_\sigma(\boldsymbol{p},\boldsymbol{x}) = f_{\mathrm{FD}}(\epsilon_{\boldsymbol{p}\sigma}-\mu(x))$, where $f_{\mathrm{FD}}(\epsilon) = (1+e^{\beta\epsilon})^{-1}$ is the Fermi-Dirac distribution function for electrons with energy $\epsilon_{\boldsymbol{p}\sigma} = \boldsymbol{p}^2/2m - \sigma M_s$ with a position dependent chemical potential $\mu(x)$, such that we have a local equilibrium. In this special case, the Boltzmann equation reduces to

$$\frac{\boldsymbol{p}}{m}\left(-\frac{\partial\mu}{\partial x}+\sigma\boldsymbol{F}\right)\frac{\partial f_{\mathrm{FD}}}{\partial\epsilon} = 0, \tag{2.22}$$

which implicitly gives an expression for the chemical potential gradient. Integration of the spatial coordinate yields the electrochemical potential difference $\Delta\mu$ along a ferromagnetic wire that is generated by a moving domain wall[61]

$$\Delta\mu = -\frac{\hbar P}{2|e|}\left(Q\dot{\varphi}_{\mathrm{dw}}+\beta\frac{\dot{r}_{\mathrm{dw}}}{\lambda_{\mathrm{dw}}}\right), \tag{2.23}$$

where the polarization enters from the addition of the opposite contributions coming form the majority and minority electrons. For a domain wall driven by an external field above the Walker breakdown threshold where the magnetization in the wall precesses, the moving magnetic texture causes a topological electromotive force on the electrons, described by the term proportional to $\dot{\phi}_{\mathrm{dw}}$ in the above equation. The precessing magnetic moments in the wall trace out a surface on the unit sphere and it is the rate with which this surface changes that causes the force. Therefore it does not depend on the detailed structure of the domain wall, but only on its charge as we showed in the discussion of the Berry phase. The dissipative contribution couples to the velocity of the wall and is present even below the Walker breakdown limit.

We have seen that besides the effective electric field a magnetic texture also leads to an effective magnetic field $\boldsymbol{B}_{\mathrm{eff}}$. Since electronic transport in the presence of a magnetic field leads, as a result of the Lorentz force, to the Hall effect, which is measured as a voltage drop perpendicular to both the bias voltage and the magnetic field. The expression for the effective magnetic field, as given in Eq. (2.17), is the same as the expression for the winding number [see Eq. (1.17)]. This means that for the skyrmion lattice the additional Hall response is of topological nature [77].

The force perpendicular to the direction of motion for the electrons has an analog in the physics of soccer. As many practitioners of ball games know, a spinning ball moving

through air follows path which is additionally curved due to the spin of the ball. This is due to the difference in relative velocities of the airflow on both sides of the spinning ball, leading to the Magnus force. For the electrons moving through the spin texture we have a similar effect.

2.4 Inclusion of strong spin-orbit coupling

We can generalize the semi-classical model to include strong SO coupling. We use a generalized exchange coupling of the spins that includes SO coupling. This means that for the Rashba-Dresselhaus Hamiltonian given by Eq. (1.24) together with the exchange coupling to the textured magnetization we can summarize the Hamiltonian for the spin as

$$\mathcal{H}_{\mathrm{SO}} + \mathcal{H}_{\mathrm{sd}} \equiv \frac{\boldsymbol{p}^2}{2m} - \boldsymbol{\Omega}(\boldsymbol{x}, \boldsymbol{p}, t) \cdot \boldsymbol{s}, \tag{2.24}$$

where $\boldsymbol{\Omega}(\boldsymbol{p}, \boldsymbol{x})$ is a phase-space dependent magnetization that consists of the exchange coupling to the magnetization and the coupling the momentum. Note that this generalized phase-space magnetization does not have a fixed length. We can again solve the equation of motion for the spin degree of freedom up to first order and then consider the equations of motion for position and momentum of the particle. Those read,

$$\dot{\boldsymbol{x}} = \frac{\partial \epsilon}{\partial \boldsymbol{p}} - \Gamma_{\boldsymbol{px}} \cdot \dot{\boldsymbol{x}} - \Gamma_{\boldsymbol{pp}} \cdot \dot{\boldsymbol{p}} - D_{\boldsymbol{pp}} \cdot \dot{\boldsymbol{p}} - D_{\boldsymbol{pq}} \cdot \dot{\boldsymbol{q}} - \boldsymbol{\Gamma}_{\boldsymbol{p}t} - \boldsymbol{D}_{\boldsymbol{p}t}; \tag{2.25}$$

$$\dot{\boldsymbol{p}} = -\frac{\partial \epsilon}{\partial \boldsymbol{x}} + \Gamma_{\boldsymbol{xx}} \cdot \dot{\boldsymbol{x}} + \Gamma_{\boldsymbol{xp}} \cdot \dot{\boldsymbol{p}} + D_{\boldsymbol{xx}} \cdot \dot{\boldsymbol{q}} + D_{\boldsymbol{xp}} \cdot \dot{\boldsymbol{p}} + \boldsymbol{\Gamma}_{\boldsymbol{x}t} + \boldsymbol{D}_{\boldsymbol{x}t}, \tag{2.26}$$

where the dispersion is given by $\epsilon = \epsilon_0(\boldsymbol{p}) - |\boldsymbol{\Omega}|$ and we have the tensors

$$\Gamma^{ij}_{\boldsymbol{\xi\zeta}} = \left(\frac{\partial \hat{\boldsymbol{\Omega}}}{\partial \xi^i} \times \frac{\partial \hat{\boldsymbol{\Omega}}}{\partial \zeta^j} \right) \cdot \hat{\boldsymbol{\Omega}}; \tag{2.27}$$

$$D^{ij}_{\boldsymbol{\xi\zeta}} = \alpha \frac{\partial \hat{\boldsymbol{\Omega}}}{\partial \xi^i} \cdot \frac{\partial \hat{\boldsymbol{\Omega}}}{\partial \zeta^j}, \tag{2.28}$$

where $\hat{\boldsymbol{\Omega}}$ is the unit vector in the direction of $\boldsymbol{\Omega}$. Note that these tensors reduce to the vectors in Eqs. (2.25) and (2.26) by replacing $\zeta^j \to t$. The tensors $\Gamma_{\boldsymbol{\xi\zeta}}$ are the the Berry curvature tensors in phase space. The results of this Section are in agreement with wave-packet dynamics [76, 78].

For static homogeneous magnets with SO coupling we have a contribution to the velocity of the particle of the form $\Gamma_{\boldsymbol{pp}} \cdot \dot{\boldsymbol{p}} \equiv \dot{\boldsymbol{p}} \times \mathcal{B}_{\boldsymbol{pp}}$, where $\mathcal{B}_{\boldsymbol{pp}}$ is the momentum space analogue of the effective magnetic field induced by a magnetic texture. This additional contribution to the velocity, which is perpendicular to an applied voltage bias is known in the literature as the anomalous velocity and was first introduced by Karplus and Luttinger [79]. It is responsible for the intrinsic contribution to the Anomalous Hall effect present in many ferromagnets. The nature of this anomalous Hall effect remained an open problem for quite some time and only recently consensus about its origins has

arrived [80, 81]. It is called intrinsic since it stems from the dispersion of the quasiparticles instead of asymmetric impurity scatterings that form the extrinsic contributions.

The intrinsic anomalous Hall conductivity is given by

$$\sigma^{ij}_{\mathrm{AH}} = -\frac{|e|^2}{\hbar}\epsilon^{ijk}\sum_{\sigma}\int \frac{d\boldsymbol{p}}{(2\pi\hbar)^2} f_{\sigma}(\boldsymbol{p},\boldsymbol{x})\mathcal{B}^{k}(\boldsymbol{p}), \tag{2.29}$$

which does not involve a relaxation time τ and in contrast to other transport coefficients in Fermi-liquid theory, involves the whole Fermi sea. This incongruity was solved by Haldane [82] who showed that the Berry phase contribution can also be expressed in terms of Fermi-surface properties only.

We discussed the topological Hall effect in the previous Section. There we noted that the effective magnetic field induced by a topological ferromagnetic texture, such as the skyrmion lattice, is of topological in nature. It depends on an invariant associated with the complex twisting and folding of the magnetization. There the winding or skyrmion number as given in Eq. 1.17 in the introduction classified the structure. For the anomalous Hall effect a similar topological invariant is used. It is called the Chern number,

$$C = \int_{BZ} \frac{d^2\boldsymbol{k}}{(2\pi)^2}\Gamma_{k_x k_y} \tag{2.30}$$

which is an integral over the first Brillouin zone. Note that the (intrinsic) anomalous Hall conductivity as given in Eq. (2.29) is, for fully occupied bands, the quantum of conductance $|e|^2/\hbar$ times the Chern number of that band. The topological expression for the anomalous Hall conductance was introduced in the context of a 2D insulating crystal in a strong perpendicular magnetic field by Thouless, Kohmoto, Nightingale and Den Nijs and is known as the TKKN invariant [83]. The use of topological invariants to make a classification of band structures led to the concept of topological insulators [84].

2.5 Thermal effects

Up to this point we only studied the charge and spin currents associated with the moving electrons and their effects. Heat currents are also of great technological relevance, for example in thermally assisted switching [85]. In this Section we briefly discuss how to understand some thermoelectric effects within our simple toy model. In thermoelectrics Mott relations exist between the conductivity and the thermal conductivity and Peltier coefficients at low temperature. The Peltier effect is the Onsager reciprocal of the Seebeck effect we discussed in the Introduction. The anomalous (Righi-Leduc) thermal conductance and Peltier coefficients should be related to the conductance as

$$\kappa^{ij}_{\mathrm{AH}} = \frac{\pi^2}{3}\frac{k_B^2 T}{|e|^2}\sigma^{ij}_{\mathrm{AH}}(\mu) \quad ; \quad \alpha^{ij}_{\mathrm{AH}} = -|e|\frac{\partial \kappa^{ij}_{\mathrm{AH}}}{\partial \mu}. \tag{2.31}$$

The expression of the anomalous Hall conductivity followed from the anomalous velocity term. For clarity we explicitly give here the equations of motion for the electrons for a

homogeneous ferromagnet with SO coupling in the simplest form,

$$\dot{\boldsymbol{x}} = \frac{\partial \epsilon(\boldsymbol{p},\boldsymbol{x})}{\partial \boldsymbol{p}} - \dot{\boldsymbol{p}} \times \boldsymbol{B}^{\boldsymbol{pp}}(\boldsymbol{p}); \tag{2.32}$$

$$\dot{\boldsymbol{p}} = -\frac{\partial \epsilon(\boldsymbol{p},\boldsymbol{x})}{\partial \boldsymbol{x}}, \tag{2.33}$$

where we omitted the dissipative terms as well (see Eqs. (2.25,2.26)). The expression for the conductivity follows from the expression for the current, which is given by

$$\boldsymbol{j}_c = -|e| \int d\boldsymbol{p} f(\boldsymbol{p}) \dot{\boldsymbol{x}}, \tag{2.34}$$

which is the average velocity of the all the particles. From this expression the anomalous Hall effect can be understood from the substitution of the expression for $\dot{\boldsymbol{p}}$ into the anomalous velocity term where the energy contains the electrostatic energy contribution $-|e|\boldsymbol{E}\cdot\boldsymbol{x}$. A question now arises how to incorporate statistical forces such as a temperature or chemical potential gradients using a Boltzmann description. Statistical forces do not enter in Eq. (2.33) which only depends on mechanical forces. Thus a temperature or chemical potential gradient does not lead to a contribution to the current independent of a relaxation time τ. In order to solve this paradox (since a chemical potential gradient should lead to the same response as an electric field) we reconsider the expression for the current.

For a canonical system, hence a system without anomalous velocity contributions, we can define the phase-space density as the derivative with respect to the chemical potential of the free energy per momentum $\boldsymbol{p}$, *i.e.*, $f(\boldsymbol{p}) = -\partial \mathcal{F}_{\surd}/\partial\mu$. Thus we can interpret Eq. (2.34) as

$$\boldsymbol{j}_c = -|e| \int d\boldsymbol{p} \left\{\boldsymbol{x}, \mathcal{F}_{\boldsymbol{p}}\right\}, \tag{2.35}$$

where $\{.,.\}$ are the canonical Poisson brackets and $\mathcal{F}_{\boldsymbol{p}} = \log(1+\exp\beta(\epsilon_{\boldsymbol{p}}-\mu))/\beta$, where $\beta = 1/k_B T$ is the inverse thermal energy. In this expression for the current the free energy density replaces the Hamiltonian in the equation for the velocity $\dot{\boldsymbol{x}} = \{\boldsymbol{x}, H\}$. The equations of motion after the adiabatic approximation have a non-canonical form. Therefore we need to be careful with using Eq.(2.34) and have to use Eq. (2.35) as our starting point. We can, however, bring the general equations of motion of Eqs. (2.25) and (2.26) in a canonical form. The Poisson brackets in this form are induced by the restriction of the spin degree of freedom. Before the adiabatic approximation the Poisson brackets are defined as

$$\{A,B\}_\omega = \frac{\partial A}{\partial X^a}\omega_{X^a X^b}(\boldsymbol{X})\frac{\partial B}{\partial X^a} \quad ; \quad \omega_{X^a X^b}(\boldsymbol{X}) = \begin{pmatrix} 0 & \delta^{ab} & 0 \\ -\delta^{ab} & 0 & 0 \\ 0 & 0 & \epsilon^{abc}s^c \end{pmatrix},$$

where $\boldsymbol{X} = (\boldsymbol{x},\boldsymbol{p},\boldsymbol{s})$ is the phase space vector and we introduced the matrix ω that encodes the symplectic structure of the phase space. The adiabatic restriction, thus

$\boldsymbol{s}(t) \to \boldsymbol{\Omega}(\boldsymbol{p}, \boldsymbol{x})$, reduces the dimensionality of phase space and induces a different symplectic structure, which in turn leads to a different form of the Poisson brackets[86]. We can obtain the induced symplectic structure from the relation

$$\tilde{\omega}^{\xi^a \xi^b}(\boldsymbol{\xi}) = \frac{\partial X^i}{\partial \xi^a} \frac{\partial X^j}{\partial \xi^b} \omega_{X^a X^b}(\boldsymbol{X}), \tag{2.36}$$

which yields the correct equations of motion as given in Eqs. (2.25) and (2.26), via $\tilde{\omega}(\boldsymbol{\xi}) \cdot \dot{\boldsymbol{\xi}} = \partial_{\boldsymbol{\xi}} \epsilon(\boldsymbol{\xi})$. Note that the Poisson brackets after the adiabatic approximation are related to the inverse matrix $\tilde{\omega}_{\boldsymbol{\xi}\xi}$ of $\tilde{\omega}^{\boldsymbol{\xi}\xi}$ given in Eq. (2.36). For the simple situation we have presented in our discussion of thermal effects associated with the anomalous Hall effect we obtain for the current

$$\boldsymbol{j}_c = -|e| \int d\boldsymbol{p} \, \{\boldsymbol{x}, \mathcal{F}\}_{\tilde{\omega}} = -|e| \int d\boldsymbol{p} f(\boldsymbol{p}) \frac{\partial \epsilon}{\partial \boldsymbol{p}} + \boldsymbol{\nabla} \times \int d\boldsymbol{p} \boldsymbol{B}^{pp}(\boldsymbol{p}) \mathcal{F}_{\boldsymbol{p}}, \tag{2.37}$$

which treats the addition of the electrostatic energy to the energy and chemical potential on the same footing and also leads to the correct Mott relation for the Peltier coefficient. Note that the above discussion is not meant as a rigorous derivation of the thermal response of systems with a nonzero spin Berry phase, but rather as a way to interpret more careful calculations.

Note that in the discussion of wave-packet dynamics the additional contribution to the current follows from the orbital magnetization of the wave packets [86–88] which is reflected in a modified density of states. Application of the Kubo formalism to thermal Hall effects also proves to be difficult. The reason lies in properly accounting for equilibrium currents in these systems [89, 90]. These equilibrium currents are related to the curl of the magnetization and cannot contribute to transport. This view is supported by the treatment of temperature gradients using Luttinger's fictitious gravitational field [91–93]. In Chapter 4 we return to these effects in the context of the Rashba ferromagnet. In this Chapter we introduced a semi-classical model to understand much of the phenomenology associated with currents coupling to magnetization dynamics. We have seen that this model gives a nice intuition for the different processes.

Chapter 3

Current-induced torques in textured Rashba ferromagnets

Abstract

In systems with small spin-orbit coupling, current-induced torques on the magnetization require inhomogeneous magnetization textures. For large spin-orbit coupling, such torques exist even without gradients in the magnetization direction. Here, we consider current-induced torques in ferromagnetic metals with both Rashba spin-orbit coupling and inhomogeneous magnetization. We first phenomenologically construct all torques that are allowed by the symmetries of the system, to first order in magnetization-direction gradients and electric field. Second, we use a Boltzmann approach to calculate the spin torques that arise to second order in the spin-orbit coupling. We apply our results to current-driven domain walls and find that the domain-wall mobility is strongly affected by torques that result from the interplay between spin-orbit coupling and inhomogeneity of the magnetization texture.

3.1 Introduction

Current-induced torques on the magnetization in conducting ferromagnets are one of the main topics of research in spintronics. In addition to being fundamentally interesting, these torques are also key to developments in memory technology[20]. Current-induced torques can be used to move domain walls through a ferromagnetic wire. When a domain wall is present the direction of the magnetization depends on the position in the wire. This spatial dependence of the magnetization gives rise to a mismatch between the electron spin polarization and local magnetization resulting in the adiabatic reactive [7, 8] and dissipative (also known as non-adiabatic) spin transfer torques (STTs) [15, 17, 40, 41, 94–96]. The occurrence of these two spin torques is well established but their relative magnitude, parametrized by the dimensionless parameter β which describes the relative strength of the dissipative torque with respect to the reactive one, is hard to measure[54, 97–99] and calculate [100].

That there exist other current-induced torques related to spin-orbit (SO) coupling of the carriers has been proposed recently [32, 33, 39, 101, 102]. In these works systems with SO coupling and homogeneous magnetization are considered. Recent experiments

can be interpreted using these current-induced torques originating from the SO coupling of the carriers [34, 35, 103–106] that, unlike the adiabatic STT mentioned above, do not require magnetization gradients. (Note, however, that these observations can also be described via the Spin-Hall effect in Pt as argued in Ref. [105].) For Rashba SO coupling two current-induced torques have been found in the situation where there is no magnetization gradient. In the experimental works, however, a domain wall is present. This implies that the description in terms of a homogeneous magnetization is incomplete and a more systematic description including both SO coupling and an inhomogeneous magnetization is called for.

It is the purpose of this Chapter to give such an inclusive description that incorporates both SO coupling and inhomogeneous magnetization textures. For definiteness, we focus on the Rashba SO coupling. In Sec. 3.2 we consider all current-induced torques which are allowed by the symmetries of the system. As the number of allowed torques is considerable, and because the symmetry considerations do not yield their relative magnitudes, we investigate these within a semi-classical Boltzmann description. In Sec. 3.6 the results for the torques are used to calculate their effect on domain-wall dynamics. We find that the current-induced domain-wall velocity depends strongly on wall geometry. Furthermore, the domain-wall mobility depends strongly on the inclusion of torques that result from the interplay of SO coupling and gradients in the magnetization.

3.2 Symmetry considerations

In this Section we use symmetry considerations to obtain all allowed current-induced torques. To illustrate our method we begin with the adiabatic spin torques in the absence of SO coupling. Subsequently we investigate the situation with SO coupling. We use the *s*-*d* model since this is a convenient model to get the qualitative description of current-induced torques. In this model the magnetization resides on the *d*-orbitals and transport is due to the mobile *s*-electrons. We investigate the system well below the Curie temperature, which means the magnetization is represented using a unit-vector field since fluctuations in its magnitude are negligible.

3.2.1 Absence of spin-orbit coupling

Within the *s*-*d* model the Hamiltonian is given by

$$\mathcal{H}_{sd} = \mathcal{H}_0(\boldsymbol{x}, \boldsymbol{p}) - \frac{\Delta}{2}\boldsymbol{m}\cdot\boldsymbol{s}, \tag{3.1}$$

where $\mathcal{H}_0$ is the Hamiltonian that describes the motion of the itinerant electrons and depends on electron momentum $\boldsymbol{p}$ and position $\boldsymbol{x}$. We have an exchange coupling between the magnetic texture $\boldsymbol{m}(\boldsymbol{x}, t)$ and the electron spin $\boldsymbol{s}(t)$ specified by the exchange splitting Δ. The total Hamiltonian $\mathcal{H}_{sd}$ is invariant under two *independent* rotations of the spin and physical space, parameterized by the rotation matrices $\mathcal{R}_{\mathrm{S}}^{ij}$ and $\mathcal{R}^{ij}$ respectively. (We neglect the coupling between the magnetization and the orbit of the electrons that occurs

via the Lorentz force. We neglect this effect for the moment because the magnetic field induced by the magnetization is very small.) Moreover, in this description we neglect the ionic lattice. We explicitly have for the rotations

$$\tilde{s}^i = \mathcal{R}_{\mathrm{S}}^{ij} s^j, \qquad \tilde{m}^i = \mathcal{R}_{\mathrm{S}}^{ij} m^j; \tag{3.2}$$

$$\tilde{x}^i = \mathcal{R}^{ij} x^j, \qquad \tilde{p}^i = \mathcal{R}^{ij} p^j. \tag{3.3}$$

Note that we use the summation convention of summing over repeated indices. The invariance of the Hamiltonian implies $\mathcal{H}_{sd}(\tilde{\boldsymbol{p}}, \tilde{\boldsymbol{x}}, \tilde{\boldsymbol{s}}, \tilde{\boldsymbol{m}}) = \mathcal{H}_{sd}(\boldsymbol{p}, \boldsymbol{x}, \boldsymbol{s}, \boldsymbol{m})$. This means that these symmetries should be respected at the level of the equations of motion. We are interested in the (linear-response-) current-induced torques, hence our expressions for the torques should be linearly dependent on the applied electric field $\boldsymbol{E}$. The possible torques that are first order in the electric field $\boldsymbol{E}$, which transforms under the action of $\boldsymbol{R}$, should involve an inner-product with another vector that transforms under the same rotation and in this way creates an invariant scalar. The only other vector that transforms in this way for this system is the gradient ∇ that acts on the magnetization. These constraints lead to the two possible current-induced torques

$$\left.\frac{\partial \boldsymbol{m}}{\partial t}\right|_{\mathrm{ST}} \propto (\boldsymbol{E}\cdot\nabla)\boldsymbol{m} + \beta \boldsymbol{m}\times(\boldsymbol{E}\cdot\nabla)\boldsymbol{m}. \tag{3.4}$$

For a treatment of spin transfer torques that incorporates the symmetries of the lattice see Ref. [107]. These terms are frequently written in terms of the current but we choose to put in the electric field here as the external perturbation, to be consistent with the rest of this Chapter. Note the parameter β which is defined as the ratio of the dissipative and reactive spin transfer torques.

The two torques in Eq. (3.4) are mutually perpendicular. Moreover they transform differently under time reversal, since they differ by a factor $\boldsymbol{m}$ which is odd under time-reversal. This difference in behavior under time-reversal symmetry implies the torques form a pair where one is reactive and the other is dissipative.

3.2.2 spin-orbit coupling

In the presence of SO coupling the Hamiltonian for the spin of the s-electron couples the spin and the momentum of the electron. We represent SO coupling for spin-$\frac{1}{2}$ carriers via the Hamiltonian

$$\mathcal{H}_{\mathrm{SO}} = -\boldsymbol{\Omega}(\boldsymbol{x}, \boldsymbol{p})\cdot\boldsymbol{s}, \tag{3.5}$$

where $\boldsymbol{\Omega}$ contains both the exchange interaction of Eq. (3.1) and SO coupling, and can be seen as a position and momentum dependent effective exchange splitting.

For definiteness, and motivated by experiments [103–105], we study the simplest form of SO coupling described by the Rashba Hamiltonian[75] $\mathcal{H}_{\mathrm{R}} = -\lambda(\boldsymbol{p}\times\boldsymbol{e}_z)\cdot\boldsymbol{s}$. The Rashba coupling together with the exchange interaction results in

$$\boldsymbol{\Omega}(\boldsymbol{x}, \boldsymbol{p}) = \frac{\Delta}{2}\boldsymbol{m}(\boldsymbol{x}) + \lambda \boldsymbol{p}\times\boldsymbol{e}_z. \tag{3.6}$$

Rashba SO coupling occurs in two-dimensional electron systems with inversion asymmetry along the direction perpendicular to the two-dimensional electron gas (which we choose as our z-axis). The SO coupling breaks the invariance of the Hamiltonian under separate rotations of the spin and orbital parts of the motion. Total angular momentum is still conserved due to the invariance of the Hamiltonian under combined rotations of spin and physical space, parameterized by $\mathcal{R}_{\mathrm{S}}^{ij} = \mathcal{R}^{ij}$.

The linear-response matrix $L_{\mathrm{cit}}(\boldsymbol{m}, \boldsymbol{e}_z, \nabla\boldsymbol{m})$ that describes the current-induced torques is defined by

$$\dot{m}^i = L_{\mathrm{cit}}^{ij}(\boldsymbol{m}, \boldsymbol{e}_z, \nabla\boldsymbol{m})E^j, \tag{3.7}$$

where $\boldsymbol{E}$ is the electric field in the plane and $\boldsymbol{e}_z$ is a unit vector in the z-direction. The linear-response matrix depends on this direction since inversion symmetry is broken along this direction. The Hamiltonian is invariant under parity transformations which implies that the linear response matrix should obey

$$-L_{\mathrm{cit}}(\boldsymbol{m}, -\boldsymbol{e}_z, -\nabla\boldsymbol{m}) = L_{\mathrm{cit}}(\boldsymbol{m}, \boldsymbol{e}_z, \nabla\boldsymbol{m}).$$

This shows that there can be torques on the magnetization without a gradient in the magnetization. These torques $\tau_{\mathrm{ST}}i = L_{ij}(\boldsymbol{m}, \boldsymbol{e}_z)E^j$ have been found before[33] and are given by

$$\boldsymbol{\tau}_{\mathrm{ST}}^{(1)} \propto \boldsymbol{m} \times (\boldsymbol{E} \times \boldsymbol{e}_z); \tag{3.8}$$

$$\boldsymbol{\tau}_{\mathrm{ST}}^{(1\perp)} \propto \boldsymbol{m} \times (\boldsymbol{m} \times (\boldsymbol{E} \times \boldsymbol{e}_z)). \tag{3.9}$$

The spin torques are perpendicular to $\boldsymbol{m}$ because it is a unit-vector field. Since the magnetization is embedded in three-dimensional space there is a two-dimensional plane perpendicular to it. This means that any spin torque $\boldsymbol{\tau}_{\mathrm{ST}}^{(i)}$ allowed by the symmetry of the system immediately defines another torque via $\boldsymbol{\tau}_{\mathrm{ST}}^{(i\perp)} = \boldsymbol{m} \times \boldsymbol{\tau}_{\mathrm{ST}}^{(i)}$. These pairs differ by a factor $\boldsymbol{m}$ which changes its sign under time-reversal, hence the two torques form a reactive-dissipative pair, like the STTs in Eq. (3.4). In the following we will show only one of the pair. All terms to first order in the gradient of the magnetization that do not involve $\boldsymbol{e}_z$, are given by

$$\boldsymbol{\tau}_{\mathrm{ST}}^{(2)} \propto (\boldsymbol{E} \cdot \nabla)\boldsymbol{m}; \tag{3.10}$$

$$\boldsymbol{\tau}_{\mathrm{ST}}^{(3)} \propto ((\boldsymbol{m} \times \boldsymbol{E}) \cdot \nabla)\boldsymbol{m}; \tag{3.11}$$

$$\boldsymbol{\tau}_{\mathrm{ST}}^{(4)} \propto (\boldsymbol{m} \cdot \boldsymbol{E})(\boldsymbol{m} \cdot \nabla)\boldsymbol{m}; \tag{3.12}$$

$$\boldsymbol{\tau}_{\mathrm{ST}}^{(5)} \propto E^a(\boldsymbol{m} \times \nabla)\boldsymbol{m}^a; \tag{3.13}$$

$$\boldsymbol{\tau}_{\mathrm{ST}}^{(6)} \propto (\boldsymbol{m} \times \boldsymbol{E})^a(\boldsymbol{m} \times \nabla)\boldsymbol{m}^a; \tag{3.14}$$

$$\boldsymbol{\tau}_{\mathrm{ST}}^{(7)} \propto \boldsymbol{m} \times \boldsymbol{E}(\nabla \cdot \boldsymbol{m}); \tag{3.15}$$

$$\boldsymbol{\tau}_{\mathrm{ST}}^{(8)} \propto (\boldsymbol{m} \times \boldsymbol{E})\,(\boldsymbol{m} \cdot (\nabla \times \boldsymbol{m}))\,, \tag{3.16}$$

In the first line the familiar STT[7, 8] describing the current-induced torque in systems with inhomogeneous magnetization is obtained. Together with the dissipative STT[15,

17, 40, 41, 94–96] that is associated with it ($\tau_{\mathrm{ST}}^{2\perp}$) those torques describe the weak SO coupling situation. In the second line we find a STT due to a Hall current. The other torques do not have a straightforward physical interpretation.

Up to this point we have explicitly given the torques to first order in either $\boldsymbol{e}_z$ or ∇. There are more torques that involve an even number of $\boldsymbol{e}_z$'s and are first order in ∇. We will not list them because the list will be to long to be illuminating. We proceed by actually calculating the torques in the next Section. The reason we do this is twofold. First, having demonstrated the existence of many spin torques due to the combined effects of SO coupling and magnetization gradients, we now explicitly calculate which torques occur within a semi-classical approach to the Rashba model. The second reason is to give an estimate of the relative magnitude of the various current-induced torques which cannot be found using symmetry arguments.

3.3 Semi-classical framework

In order to investigate microscopically which current-induced torques appear for the textured Rashba ferromagnet we use a semi-classical approach. This approach has proved its merit in the description of the anomalous Hall effect [80, 108, 109]. We describe the system by the Hamiltonian

$$\mathcal{H} = \frac{\boldsymbol{p}^2}{2m_e} - \boldsymbol{\Omega}(\boldsymbol{x}, \boldsymbol{p}) \cdot \boldsymbol{s} + E_{\mathrm{MM}}[\boldsymbol{m}], \tag{3.17}$$

where $\boldsymbol{\Omega}(\boldsymbol{x}, \boldsymbol{p})$ is the effective Zeeman field, given in Eq. (3.6), that incorporates the Rashba SO coupling and the exchange coupling, and $E_{\mathrm{MM}}[\boldsymbol{m}]$ is the micromagnetic energy functional for the magnetization. Furthermore, m_e is the effective mass of the electron. The equation of motion for the spin degree of freedom is written as

$$\frac{d\boldsymbol{s}}{dt} = \frac{1}{\hbar}\boldsymbol{s} \times \boldsymbol{\Omega} - \frac{\alpha}{\hbar}\boldsymbol{s} \times (\boldsymbol{s} \times \boldsymbol{\Omega}),$$

where we introduced a damping term proportional to α that describes relaxation of the spin into the direction of the effective Zeeman field. The spin dynamics is much faster than the motion of the electrons such that we can solve the above equation of motion up to first order in time derivatives of $\boldsymbol{\Omega}$. We obtain the following solutions

$$\boldsymbol{s}_s = s\hat{\boldsymbol{\Omega}} + s\frac{\hbar}{\sqrt{\boldsymbol{\Omega} \cdot \boldsymbol{\Omega}}}\frac{d\hat{\boldsymbol{\Omega}}}{dt} \times \hat{\boldsymbol{\Omega}} - \frac{\hbar\alpha}{\sqrt{\boldsymbol{\Omega} \cdot \boldsymbol{\Omega}}}\frac{d\hat{\boldsymbol{\Omega}}}{dt}, \tag{3.18}$$

where $s = \pm 1$ describe the majority($s = +$)/minority($s = -$) electrons, and $\hat{\boldsymbol{\Omega}} = \boldsymbol{\Omega}/|\boldsymbol{\Omega}|$. The first term describes the adiabatic following of the effective magnetization texture by the electron-spins. The other terms describe the slight mismatch of the spins with the effective magnetization. We find the dynamics of the itinerant electrons by inserting the first order solutions of the spin degree of freedom, given in Eq. (3.18), into the Hamilton

equations of motion for the electrons. We obtain

$$\begin{aligned}\dot{x}_s^i &= \frac{\partial \epsilon_s}{\partial p^i} - s\hbar\left(\frac{\partial \hat{\mathbf{\Omega}}}{\partial p^i}\times\frac{d\hat{\mathbf{\Omega}}}{dt}\right)\cdot\hat{\mathbf{\Omega}} + \alpha\hbar\frac{\partial\hat{\mathbf{\Omega}}}{\partial p^i}\cdot\frac{d\hat{\mathbf{\Omega}}}{dt};\\ \dot{p}_s^i &= -\frac{\partial\epsilon_s}{\partial x^i} + s\hbar\left(\frac{\partial\hat{\mathbf{\Omega}}}{\partial x^i}\times\frac{d\hat{\mathbf{\Omega}}}{dt}\right)\cdot\hat{\mathbf{\Omega}} - \alpha\hbar\frac{\partial\hat{\mathbf{\Omega}}}{\partial x^i}\cdot\frac{d\hat{\mathbf{\Omega}}}{dt} - |e|\boldsymbol{E}^i,\end{aligned}$$

where $\epsilon_s = \boldsymbol{p}^2/2m_e - s|\mathbf{\Omega}|$ is the dispersion for the majority($s=+$)/minority($s=-$) electrons. Note that we added an electric field to induce a transport current. The total time derivatives on $\hat{\mathbf{\Omega}}$ should be understood as

$$\frac{d\hat{\mathbf{\Omega}}}{dt} = \dot{x}_s^i\frac{\partial\hat{\mathbf{\Omega}}}{\partial x^i} + \dot{p}_s^i\frac{\partial\hat{\mathbf{\Omega}}}{\partial p^i}.$$

Now that we have this semi-classical description of the single particle dynamics we calculate the spin torques using the Boltzmann equation for the distribution function $f_s(\boldsymbol{x},\boldsymbol{p},t)$ of the particles, which, in the relaxation-time (τ_r) approximation, is given by,

$$\frac{d}{dt}f_s(\boldsymbol{x},\boldsymbol{p},t) = -\frac{f_s(\boldsymbol{x},\boldsymbol{p},t) - f^{\mathrm{FD}}(\epsilon_s)}{\tau_r}, \tag{3.19}$$

where $f^{\mathrm{FD}}(\epsilon) = (1+e^{\beta\epsilon})^{-1}$ is the Fermi-Dirac distribution function. The relaxation-time approximation is the simplest description of the Boltzmann collision integral. We make the relaxation-time approximation here for convenience. A detailed study of the collision-integral in the presence of strong SO coupling is beyond the scope of this work. We refer to the work by Pesin and MacDonald in Ref. [34] for more details on the situation of homogeneous magnetization. The left-hand side in Eq. (3.19) should be read as

$$\frac{df_s}{dt} = \frac{\partial f_s(\boldsymbol{x},\boldsymbol{p},t)}{\partial t} + \frac{\partial f_s(\boldsymbol{x},\boldsymbol{p},t)}{\partial\boldsymbol{p}}\cdot\dot{\boldsymbol{p}}_s + \frac{\partial f_s(\boldsymbol{x},\boldsymbol{p},t)}{\partial\boldsymbol{x}}\cdot\dot{\boldsymbol{x}}_s.$$

The equation of motion for the magnetization is the Landau-Lifshitz-Gilbert (LLG) equation

$$\frac{\partial\boldsymbol{m}}{\partial t} = -\gamma\boldsymbol{m}\times\boldsymbol{H}_{\mathrm{eff}} + \alpha_G\boldsymbol{m}\times\frac{\partial\boldsymbol{m}}{\partial t} + \boldsymbol{\tau}_{sd}, \tag{3.20}$$

where γ is the gyromagnetic ratio and the torques due to the s-d coupling

$$\boldsymbol{\tau}_{sd} = \Delta/(2\hbar)\boldsymbol{m}\times\langle\boldsymbol{s}\rangle$$

, contain the spin torques of interest and a renormalization of the parameters in the LLG[94] equation which we discuss in this Section. The current-induced torques are proportional to the electric field and will be given in Sec. 3.5. The renormalized LLG equation we obtain is given by

$$(1-\eta)\frac{\partial\boldsymbol{m}}{\partial t} = -\gamma\boldsymbol{m}\times\boldsymbol{H}'_{\mathrm{eff}} + \alpha'_G\boldsymbol{m}\times\frac{\partial\boldsymbol{m}}{\partial t} + \boldsymbol{\tau}_{\mathrm{ST}}, \tag{3.21}$$

where $\boldsymbol{\tau}_{\mathrm{ST}}$ contains all terms of $\boldsymbol{\tau}_{\mathrm{sd}}$ proportional to the electric field and $\boldsymbol{H}'_{\mathrm{eff}}$ is defined as the effective magnetic field acting on the magnetization which acquires an additional term from the coupling to the electrons

$$\boldsymbol{H}'_{\mathrm{eff}} = -\frac{\delta E_{\mathrm{MM}}}{\delta \boldsymbol{m}} + \alpha \frac{m_e^2 a^2 \lambda_R^2}{2\gamma\pi\hbar^2}(1 + \frac{4\epsilon_F^2}{\Delta^2})(\dot{\boldsymbol{m}} \cdot \boldsymbol{e}_z)\boldsymbol{e}_z, \tag{3.22}$$

and the renormalized quantities in Eq. (3.21) are given by

$$\eta = \frac{m_e a^2}{\pi\hbar^2}\left(\frac{\Delta}{2} - 4\frac{m_e \lambda^2 \epsilon_F}{\Delta} m_z^2\right);$$

where a is the lattice constant. The additional term in Eq. (3.22) is an anisotropic damping term which for the typical parameters (see Table 3.2) we use in the calculation of the domain wall dynamics is negligible, moreover these parameters also imply $\eta \ll 1$. Furthermore we obtain that the observed Gilbert damping constant is given by

$$\alpha'_G = \alpha_G - \alpha \frac{a^2 m_e}{\pi\hbar^2}\left(\epsilon_F - \frac{m_e\lambda^2}{2}(1 - \frac{4\epsilon_F^2}{\Delta^2}(1 + 4m_z^2))\right). \tag{3.23}$$

Note that α_G phenomenologically describes the damping of the magnetization due to interactions other than the *s-d* coupling, such as relaxation due to magnon-phonon interactions. Before we calculate the spin torques within this semi-classical framework we determine the current as a function of electric field within this simple model. We need this later on to express the spin torques in terms of the current.

3.4 Conductivity

In this Section we give the conductivity for the Rashba system. Note that the conductivity we find here is only correct within this simple *s-d* description. We need the conductivity in order to interpret the current-induced torques in the next Section. The conductivity σ_{ij} is defined as $j_c^i = \sigma^{ij} E^i$, where $\boldsymbol{j}_c$ is the charge-current density. We calculate the conductivity up to first order in the gradient of the magnetization and up to second order in the SO coupling strength. The expression for the charge-current density is given by

$$\boldsymbol{j}_c = -|e| \sum_{s=\pm} \int \frac{d^2\boldsymbol{p}}{(2\pi\hbar)^2} f_s(\boldsymbol{x}, \boldsymbol{p}, t)\dot{\boldsymbol{x}}_s. \tag{3.24}$$

Using the relaxation-time approximation described in the previous Section we find that the conductivity has three contributions $\sigma = \sigma_0 + \sigma_{\mathrm{AH}} + \sigma_{\mathrm{AMR}}$ corresponding to the diagonal, anomalous Hall effect and anisotropic magnetoresistance, respectively. The diagonal conductivity is given by

$$\frac{\sigma_0^{ij}}{G_0} = \left(\frac{\epsilon_F \tau_r}{\hbar} + \alpha \frac{4 m_e \lambda^2 \epsilon_F}{\Delta^2}\right)\delta^{ij}, \tag{3.25}$$

where $G_0 = 2|e|^2/h$ is the quantum of conductance. The second contribution

$$\frac{\sigma^{ij}_{\rm AH}}{G_0} = \left(\frac{2m_e\lambda^2}{\Delta} m_z + \lambda\tau_r(\boldsymbol{m}\cdot(\nabla\times\boldsymbol{m}) - \alpha\frac{2\epsilon_F}{\Delta}(\nabla\cdot\boldsymbol{m})) \right)\epsilon^{ijz}, \tag{3.26}$$

which is the anomalous Hall response generalized to inhomogeneous magnetization. The last contribution to the conductivity is

$$\frac{\sigma^{ij}_{\rm AMR}}{G_0} = m_e\lambda^2 \left(\alpha\frac{4\epsilon_F}{\Delta^2} - \frac{\tau_r}{\hbar} \right) \epsilon^{iaz}\epsilon^{jbz} m^a m^b, \tag{3.27}$$

which depends on the relative orientation of the electric field and the magnetization and hence corresponds to anisotropic magnetoresistance. For later reference we also define the current polarization via

$$\mathcal{P}\boldsymbol{j}_c \equiv -|e| \sum_{s=\pm} \int \frac{d^2\boldsymbol{p}}{(2\pi\hbar)^2} f(\epsilon_s) s\dot{\boldsymbol{x}}_s.$$

3.5 Current-induced torques

In this Section we give the current-induced torques for the Rashba model, introduced in Sec. 3.3. The current-induced torques can be calculated from the current-induced spin density. They are given by

$$\begin{aligned} \boldsymbol{\tau}_{\rm ST} &= \frac{\Delta}{2\hbar}\boldsymbol{m}\times\langle\boldsymbol{s}\rangle \\ &= \frac{\Delta a^2}{2\hbar}\boldsymbol{m}\times\sum_{s=\pm}\int\frac{d^2\boldsymbol{p}}{(2\pi\hbar)^2} f_s(\boldsymbol{x},\boldsymbol{p},t)\boldsymbol{s}_s, \end{aligned} \tag{3.28}$$

where $\boldsymbol{\tau}_{\rm ST}$ is the sum of all the separate spin torques we list below. We evaluate the integral in Eq. (3.28) up to first order in the damping parameter α and gradient of the magnetization and up to second order in the spin-orbit coupling strength λ. Note that we only include terms linear in the electric field, and that we take $\partial\boldsymbol{m}/\partial t = 0$. Taking into account this time-dependence gives rise to renormalization of damping and gyromagnetic ratio that we already discussed in the previous Section.

In agreement with our phenomenological arguments [see Eqs. (3.8, 3.9)], we obtain two spin torques that are zeroth order in the gradient of the magnetization which are given by

$$\boldsymbol{\tau}^{(1)} = \frac{|e|m_e\lambda a^2}{\pi\hbar^2}\left(\frac{\Delta\tau_r}{2\hbar} - \alpha\frac{2\epsilon_F}{\Delta}\right)(\boldsymbol{E}\times\boldsymbol{e}_z)\times\boldsymbol{m}; \tag{3.29}$$

$$\boldsymbol{\tau}^{(1\perp)} = \frac{|e|m_e\lambda a^2}{\pi\hbar^2}((\boldsymbol{E}\times\boldsymbol{e}_z)\times\boldsymbol{m})\times\boldsymbol{m}. \tag{3.30}$$

The dependence on the magnetization of these homogeneous SO induced spin torques where derived before [32–34, 106]. However, there is a major difference with all earlier

results. Note that Eq. (3.30) does not depend on the relaxation in the system and is an intrinsic torque that can be associated to the Berry curvature due to SO coupling[110]. In addition, for $\alpha \neq 0$, we find another contribution to these torques coming from spin relaxation. Note that the two torques given above form a perpendicular pair, one dissipative one reactive. In what follows we will group the torques into these pairs when both reactive and dissipative torques emerge to second order in SO coupling.

All other torques are first order in the gradient of the magnetization. The first two torques we find are given by

$$\boldsymbol{\tau}^{\mathrm{STT}} = -\frac{|e|\tau_r a^2}{\pi\hbar^2}\left(\frac{\Delta}{2}+2\frac{\alpha\hbar m_e\lambda^2}{\tau_r\Delta}-12m_e\lambda^2\frac{\epsilon_F}{\Delta}\right)(\boldsymbol{E}\cdot\nabla)\boldsymbol{m}; \tag{3.31}$$

$$\boldsymbol{\tau}^{\mathrm{STT}\perp} = \frac{|e|\alpha\tau_r a^2}{\pi\hbar^2}\left(\epsilon_F+\frac{m_e\lambda^2}{2}\left(7+\frac{4\epsilon_F^2}{\Delta^2}\left(3+4m_z^2\right)\right)\right)\boldsymbol{m}\times(\boldsymbol{E}\cdot\nabla)\boldsymbol{m}, \tag{3.32}$$

which are the well known STTs that also occur in systems with negligible SO coupling, see Eq. (3.4), and are due to the spin-polarized current in the direction of the electric field. The ratio of these two torques defines the β parameter. We find that

$$\beta = -\frac{2\alpha}{\Delta}\left(\epsilon_F+m\lambda_R^2\left(\frac{7}{2}+\frac{\epsilon_F^2}{\Delta^2}(30+8m_z^2)\right)\right). \tag{3.33}$$

In the previous Section we showed that the current can be decomposed into three components. Several of the torques we find can be interpreted as the ordinary spin transfer torques [Eq. (3.4)] with current response modified due to the SO coupling. First, we have the torques

$$-\frac{4|e|m_e\epsilon_F\lambda^2a^2}{\pi\Delta^2\hbar}(\boldsymbol{m}\cdot\boldsymbol{e}_z)((\boldsymbol{E}\times\boldsymbol{e}_z)\cdot\nabla)\boldsymbol{m};$$
$$\frac{2|e|m_e\alpha\lambda^2a^2}{\pi\Delta\hbar}(\boldsymbol{m}\cdot\boldsymbol{e}_z)\boldsymbol{m}\times((\boldsymbol{E}\times\boldsymbol{e}_z)\cdot\nabla)\boldsymbol{m},$$

which are due to the anomalous Hall current, $j^i_{\mathrm{AH}}\equiv\sigma^{ij}_{\mathrm{AH}}E^j$, and can therefore be written as

$$\boldsymbol{\tau}^{\mathrm{AH}} = \mathcal{P}(\boldsymbol{j}_{\mathrm{AH}}\cdot\nabla)\boldsymbol{m}; \tag{3.34}$$

$$\boldsymbol{\tau}^{\mathrm{AH}\perp} = \mathcal{P}\frac{\alpha\Delta}{2\epsilon_F}\boldsymbol{m}\times(\boldsymbol{j}_{\mathrm{AH}}\cdot\nabla)\boldsymbol{m}. \tag{3.35}$$

Two torques can be interpreted to be a generalization of the STTs coming from the anisotropic magnetoresistance response given by Eq.(3.27). These torques are

$$\boldsymbol{\tau}^{\mathrm{AMR}} = -\frac{2|e|m_e\lambda^2a^2}{\pi\Delta\hbar}\left(\alpha-24\frac{\epsilon_F\tau_r}{\hbar}\right)((\boldsymbol{E}\times\boldsymbol{e}_z)\cdot\boldsymbol{m})((\boldsymbol{m}\times\boldsymbol{e}_z)\cdot\nabla)\boldsymbol{m}; \tag{3.36}$$

$$\boldsymbol{\tau}^{\mathrm{AMR}\perp} = -\frac{|e|m_e\lambda^2\alpha\tau_r a^2}{\pi\hbar^2}(5+16\frac{\epsilon_F^2}{\Delta^2})((\boldsymbol{E}\times\boldsymbol{e}_z)\cdot\boldsymbol{m})\boldsymbol{m}\times((\boldsymbol{m}\times\boldsymbol{e}_z)\cdot\nabla)\boldsymbol{m}. \tag{3.37}$$

The next torque, given by

$$\boldsymbol{\tau}^{\mathrm{Hall}} = -\frac{|e|m_e\lambda^2\alpha\tau_r a^2}{2\pi\hbar^2}(1+4\frac{\epsilon_F^2}{\Delta^2})((\boldsymbol{E}\times\boldsymbol{m})\cdot\nabla)\boldsymbol{m}, \tag{3.38}$$

has the symmetry of a STT due to a normal Hall response. This is not the normal Hall response because it is quadratic in the SO coupling parameter. In our description we did not include the normal Hall response of the system, due to the smallness of the effect.

The torques obtained up to this point could be interpreted as the known SO coupling induced spin torques for Eqs. (3.29, 3.30) and the STTs [in Eqs. (3.31)–(3.38)] with a current response that is modified due to SO coupling. Now we will list the torques that cannot be interpreted as known current-induced torques. We have the pairs

$$\boldsymbol{\tau}^{\mathrm{a}} = \frac{2|e|m_e\lambda^2a^2}{\pi\Delta\hbar}\left(\frac{\epsilon_F\tau_r}{\hbar}-\alpha\right)(\boldsymbol{m}\times(\boldsymbol{E}\times\boldsymbol{e}_z))^a\boldsymbol{m}\times(\boldsymbol{e}_z\times\nabla)m^a; \tag{3.39}$$

$$\boldsymbol{\tau}^{\mathrm{a}\perp} = -\frac{4|e|m_e\epsilon_F\lambda^2a^2}{\pi\Delta^2\hbar}(\boldsymbol{m}\times(\boldsymbol{E}\times\boldsymbol{e}_z))^a\boldsymbol{m}\times(\boldsymbol{m}\times(\boldsymbol{e}_z\times\nabla))m^a, \tag{3.40}$$

and

$$\boldsymbol{\tau}^{\mathrm{b}} = -2\frac{\alpha|e|m_e\lambda^2a^2}{\pi\hbar}\frac{\tau_r}{\hbar}(\boldsymbol{E}\times\boldsymbol{e}_z)^a\boldsymbol{m}\times(\boldsymbol{e}_z\times\nabla)m^a; \tag{3.41}$$

$$\boldsymbol{\tau}^{\mathrm{b}\perp} = \frac{2|e|m_e\lambda^2a^2}{\pi\Delta\hbar}\left(\alpha-\frac{\epsilon_F\tau_r}{\hbar}\right)(\boldsymbol{E}\times\boldsymbol{e}_z)^a\boldsymbol{m}\times(\boldsymbol{m}\times(\boldsymbol{e}_z\times\nabla))m^a. \tag{3.42}$$

We also have four torques that do not form reactive-dissipative pairs, listed below:

$$\boldsymbol{\tau}^{\mathrm{c}} = 4\frac{|e|m_e\epsilon_F\lambda^2\tau_ra^2}{\pi\Delta\hbar^2}(\boldsymbol{m}\cdot\nabla\boldsymbol{m}\cdot\boldsymbol{e}_z)\boldsymbol{m}\times(\boldsymbol{E}\times\boldsymbol{e}_z); \tag{3.43}$$

$$\boldsymbol{\tau}^{\mathrm{d}} = -4\frac{|e|m_e\epsilon_F\lambda^2\tau_ra^2}{\pi\Delta\hbar^2}(\boldsymbol{E}\times\boldsymbol{e}_z)^a(\boldsymbol{m}\cdot\nabla)m^a(\boldsymbol{m}\times\boldsymbol{e}_z); \tag{3.44}$$

$$\boldsymbol{\tau}^{\mathrm{e}} = \frac{|e|m_e\lambda^2\alpha\tau_ra^2}{\pi\hbar^2}(1+4\frac{\epsilon_F^2}{\Delta^2})E^a(\boldsymbol{m}\times\nabla)m^a; \tag{3.45}$$

$$\boldsymbol{\tau}^{\mathrm{f}} = \frac{3|e|m_e\lambda^2\alpha\tau_ra^2}{2\pi\hbar^2}(1+4\frac{\epsilon_F^2}{\Delta^2})\boldsymbol{e}_z^a(\boldsymbol{m}\times\boldsymbol{e}_z)(\boldsymbol{E}\cdot\nabla)m^a. \tag{3.46}$$

When we discussed all the possible torques in Sec. 3.2.2 we always obtained pairs of a reactive and a dissipative torque. There we only looked at the torques that respect the symmetries of the system. That not all the torques we obtained via the semi-classical approximation form reactive-dissipative pairs means that within this approximation some of the allowed torques are not realized. Note that the above torques are of second order in $\boldsymbol{e}_z$, and have therefore not been explicitly written down in Sec. 3.2.2. The current-induced spin torques in this Section are the central result of this Chapter. From the list of torques we presented here it is clear that the interplay of SO coupling and an inhomogeneous magnetization gives rise to many spin torques. In the next Section we consider their effect on current-induced domain-wall motion.

3.6 Domain-wall motion

In this Section we investigate the effect the spin torques have on current-induced domain-wall dynamics. We study the domain-wall dynamics by employing the one-dimensional rigid domain-wall model. Within this model the dynamics is captured by the collective

coordinates of the wall which are its position $r_{\rm dw}$ and central angle $\varphi_{\rm dw}$. We study three different realizations of domain walls summarized in Table 3.1. Due to the SO coupling the current-driven motion of the three walls differs. In order to arrive at the equations of motion for the collective coordinates we describe the direction of the magnetization $\boldsymbol{m} = (\cos\varphi_{\rm dw}\sin\theta_{\rm dw}, \sin\varphi_{\rm dw}\sin\theta_{\rm dw}, \cos\theta_{\rm dw})$ using two angles $\theta_{\rm dw}$ and $\varphi_{\rm dw}$. We use $\theta_{\rm dw}(x,t) = 2\arctan\left[\exp(x - r_{\rm dw}(t))/\lambda_{\rm dw}\right]$ and the time-dependent but spatially homogeneous $\varphi_{\rm dw}(t)$, where $\lambda_{\rm dw} = \sqrt{J/K}$ is the domain-wall width in terms of the exchange stiffness J and the easy axis anisotropy K. This description of the domain wall is rigid, that is, the domain wall can only move or rotate. The direction of the electric field is specified by the angle ϕ_E with the x-axis in the x-y plane. The known[14, 101, 111] equations of motion for the collective coordinates $r_{\rm dw}$ and $\varphi_{\rm dw}$ are augmented by terms obtained from the current-induced torques of the previous Section. In the calculations we make use of the parameter values as given in Table 3.2. These parameters are typical for metallic ferromagnets, and the value of the spin-orbit coupling is taken from Ref. [103, 104]. Furthermore, we give the results as a function of the critical field E_c and velocity v_c for the case without SO coupling, which are defined as[14]

$$v_c = \frac{K_\perp}{\hbar}\lambda_{\rm dw}; \qquad E_c = \frac{v_c}{\mu_s^0}, \tag{3.47}$$

where the spin mobility in absence of SO coupling is defined as

$$\mu_s^0 = -\frac{|e|\tau_r \Delta a^2}{2\pi\hbar^2},$$

which is the zero SO coupling ($\lambda \to 0$) limit of Eq. (3.31). In Eq. (3.21) we introduced the renormalized Gilbert damping parameter α_G' which is the Gilbert damping parameter that will be measured in experiments. We expect that the Gilbert damping α_G for the magnetization and the damping α for the itinerant spins are of the same order of magnitude. In the Appendix we give the equations of motion for the Néel(x) and Bloch(y) wall configurations. Here we explicitly address the Néel(z) wall.

The equations of motion for the collective coordinates are obtained by inserting the Néel(z) domain-wall *ansatz*, as given above, into the equation of motion for the magnetization, see Eq. (3.21). To get the equations of motion we take the inner-product with $\delta\boldsymbol{m}_{\rm Néel(z)}/\delta r_{\rm dw}$, for one equation of motion and similar for $\delta\boldsymbol{m}_{\rm Néel(z)}/\delta\varphi_{\rm dw}$. Subsequently we integrate those two equations over all space. The two equations of motion we obtain

Table 3.1: Magnetic anisotropy configuration and the corresponding domain wall structures.

	Easy Axis (K)	Hard Axis ($K_\perp$)	Configuration
Néel(z)	z	y	$\uparrow\rightarrow\downarrow$
Bloch(x)	x	z	$\rightarrow\otimes\leftarrow$
Bloch(y)	y	x	$\otimes\uparrow\odot$

Table 3.2: The parameters used in this Chapter for the results shown in the figures.

ϵ_F	=	1 eV	Δ	=	0.1 eV
$m\lambda^2$	=	9 meV	α'_G	=	0.05
α	=	0.05	τ	=	30 fs
$\lambda_{\rm dw}$	=	10 nm	a	=	0.3 nm

in this way are given below

$$\frac{\dot{r}_{\rm dw}}{\lambda_{\rm dw}} - \alpha'_G\dot{\varphi}_{\rm dw} = \frac{K_\perp}{\hbar}\sin 2\varphi_{\rm dw} + \left(\frac{\pi}{2}\tau^{(1)} + \frac{6\tau^{\rm a}+4\tau^{\rm c}}{6\lambda_{\rm dw}}\cos\varphi_{\rm dw} - \frac{\tau^{\rm e}}{3\lambda_{\rm dw}}\sin\varphi_{\rm dw}\right)E\cos(\phi_E-\varphi_{\rm dw}) + \frac{2\tau^{{\rm b}\perp}-4\tau^{\rm AMR}}{6\lambda_{\rm dw}}E\sin(\phi_E-\varphi_{\rm dw})\sin\varphi_{\rm dw} - \frac{\tau^{\rm STT}}{\lambda_{\rm dw}}E\cos\phi_E; \quad (3.48)$$

$$\dot{\varphi}_{\rm dw} + \alpha'_G\frac{\dot{r}_{\rm dw}}{\lambda_{\rm dw}} = \left(\frac{\pi}{2}\tau^{(1\perp)} - \frac{\tau^{{\rm a}\perp}}{\lambda_{\rm dw}}\cos\varphi_{\rm dw}\right)E\cos(\phi_E-\varphi_{\rm dw}) + \frac{4\tau^{{\rm AMR}\perp}+2\tau^{\rm b}}{3\lambda_{\rm dw}}E\sin(\phi_E-\varphi_{\rm dw})\sin\varphi_{\rm dw} + \frac{2\tau^{\rm f}+3\tau^{{\rm STT}\perp}}{3\lambda_{\rm dw}}E\cos\phi_E. \quad (3.49)$$

The scalars $\tau^{(i)}$ are defined as the prefactors in front of the vector quantities of the torques in Section 3.5.

The boundary conditions for the current through the ferromagnet are such that only a current in the x-direction is present. In the figures we took $\phi_E = 0$, since the off-diagonal contributions in the conductivity give rise to a small ($< 1\%$ of the external field for the parameters used) voltage gradient in the y-direction. The average domain-wall velocity is defined as $v_{\rm dw} = \langle\dot{r}_{\rm dw}\rangle$, where the brackets denote a long-time average.

3.6.1 Interpretation of domain-wall motion

The results in Figs. 3.1 and 3.2 show that the inclusion of spin torques due to the combined effect of SO coupling and an inhomogeneous magnetization changes the domain-wall mobility $\mu_{\rm dw} = dv_{\rm dw}/dE$ completely as compared to the situation without these torques.

In Fig. 3.1 we show the average Néel(z)-wall velocity as a function of the applied electric field in the x-direction. The different lines correspond to the following situations: The blue dashed and dot-dashed lines correspond to current-driven domain-wall motion without torques induced by SO coupling, *i.e.*, only the STTs. The dashed line is the result of the limit $\lambda_R \to 0$ of Eqs. (3.48, 3.49).

In Sec. 3.3 we obtained a renormalized version of the LLG equation (see Eq. (3.21)) due to SO coupling and in Sec. 3.5 we showed that the parameter β also on the strength of the SO coupling as can be seen from Eq. (3.33). The dot-dashed line shows the

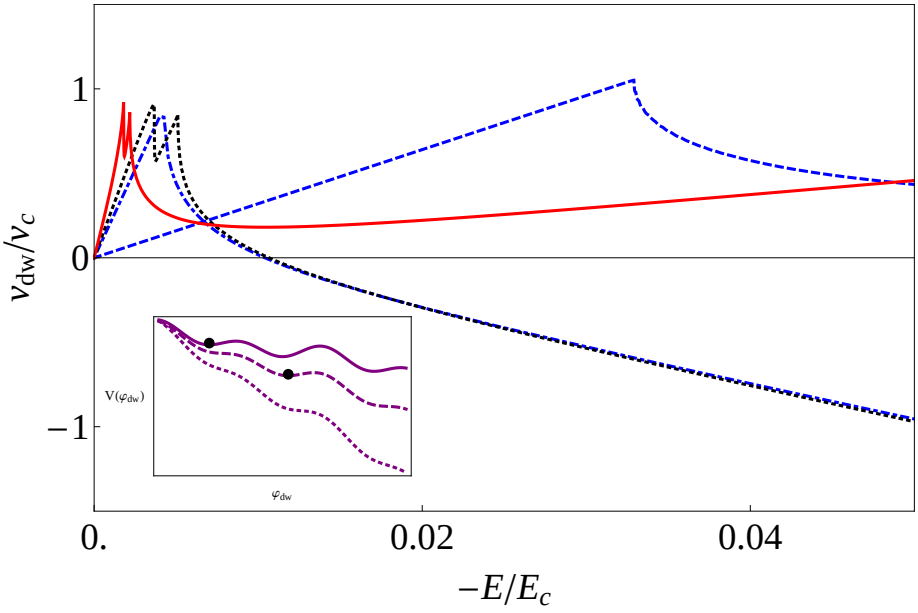

Figure 3.1: Average velocity of a Néel(z) wall as a function of the applied field. The dashed blue line is the situation without SO coupling ($\lambda_R = 0$), the dot-dashed blue line represents current-driven domain-wall motion without torques induced by the SO coupling but with the parameters renormalized by the SO coupling, the dotted black line shows the results with only the homogeneous SO torques, *i.e.* $\boldsymbol{\tau}^{(1)}$ and $\boldsymbol{\tau}^{(1\perp)}$ added to the STTs. The solid red line shows the result of the solution of the equations of motion including all spin torques. The parameters used to obtain these results are given in Table 3.2. The inset is an illustration of the tilted washboard potential of the $\varphi_{\rm dw}$ coordinate for increasing values of applied field. Due to the SO coupling there are inequivalent local minima. The angle points in the direction of first local minimum, with slightly more field the angle makes a fast rotation to the second minima. Above Walker breakdown there are no more local minima and the angle rotates in time.

result for keeping only the STTs in the equation of motion but with the parameters renormalized by the SO coupling. The dotted black line is the result with the STTs and the homogeneous SO coupling induced torques in Eqs. (3.29, 3.30). The solid red line is the result for the full equations of motion in Eqs. (3.48, 3.49).

In Fig. 3.1 we see that the SO coupling splits the Walker breakdown in two. Before Walker breakdown the domain-wall angle is time-independent $\varphi_{\rm dw}(t) = \phi_{\rm dw}$, where $\phi_{\rm dw}$ is the local minimum of a tilted washboard potential as shown in the inset. This tilted washboard potential $V(\varphi_{\rm dw})$ is obtained by eliminating $\dot{r}_{\rm dw}$ from Eqs. (3.48, 3.49), such that we obtain the equation of motion $\dot{\varphi}_{\rm dw} = -dV(\varphi_{\rm dw})/d\varphi_{\rm dw}$. When the domain-wall angle is in a local minimum of the washboard potential $\dot{\varphi}_{\rm dw} = 0$. Without SO coupling the washboard is formed by the anisotropy energy only and the tilting is due to the

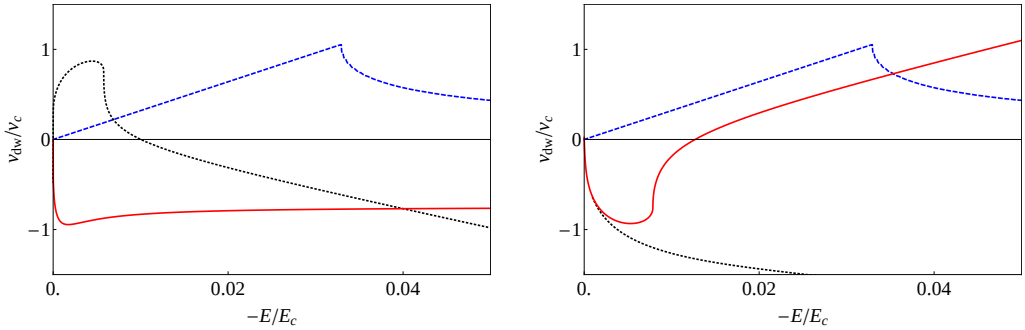

Bloch(x) domain wall Bloch(y) domain wall

Figure 3.2: Average domain-wall velocity as a function of applied electric field for the Bloch(x) and Bloch(y) domain-wall configurations. The dashed blue lines represent the situation without SO coupling ($\lambda_R = 0$), the dotted black lines show the results with only the homogeneous SO torques, *i.e.* $\boldsymbol{\tau}^{(1)}$ and $\boldsymbol{\tau}^{(1\perp)}$ added to the STTs. The solid red lines show the result of the solution of the equations of motion including all spin torques. The equations of motion can be found in the Appendix to this Chapter.

applied field E. When we add SO coupling to the equation the field also changes the washboard potential leading to inequivalent local minima. This explains the splitting of the Walker breakdown for the Néel(z) domain wall structure.

After Walker breakdown the asymptotic domain-wall velocities are determined by the effective mobility, which is simply μ_s^0 in the case without SO coupling. The effective mobility for the case with only the homogeneous SO induced torques is the same as the mobility for renormalized current-induced domain-wall motion with STTs only, which can be seen by the asymptotic behavior of the dot-dashed and dotted lines. When we include all torques induced by the SO coupling not only the magnitude but also the sign of this effective mobility changes with respect to the previously discussed cases. The effective mobility is hard to calculate since the tilted washboard potential for the domain-wall angle is nonlinearly dependent on the applied field.

In Fig. 3.2 we show the results for the Bloch(x) and Bloch(y) walls respectively. It is clear that also in these cases the additional torques induce qualitatively different behavior of the domain-wall motion compared to the situation with only the torques induced by SO coupling for homogeneous magnetization.

3.7 Discussion

In this Chapter we considered Rashba SO coupling. Our results can be generalized straightforwardly to linear Dresselhaus SO coupling [73], which is linear in momentum too. For linear Dresselhaus coupling the dispersion of the carriers is the same as for Rashba coupling. The effective magnetization for the Dresselhaus SO coupling is given by $\boldsymbol{\Omega}_{\mathrm{D}}(\boldsymbol{x},\boldsymbol{p}) = \Delta\boldsymbol{m}/2 + \lambda_{\mathrm{D}}(-p_x, p_y, 0)^T$. This means $\boldsymbol{p} \times \boldsymbol{e}_z \to (-p_x, p_y, 0)^T$ when

we go from the Rashba to the Dresselhaus coupling. The current-induced torques we found in Sec. 3.5 involve factors $\boldsymbol{v} \times \boldsymbol{e}_z$, where $\boldsymbol{v}$ is a vector. For clarity we consider $\boldsymbol{\tau}^{(1)} \propto (\boldsymbol{E} \times \boldsymbol{e}_z) \times \boldsymbol{m}$ (given in Eq. (3.29)), for the Dresselhaus system the torque would be in the direction $(\boldsymbol{E} \times \boldsymbol{e}_z) \times \boldsymbol{m} \to (-E_x, E_y, 0) \times \boldsymbol{m}$. In this way we obtain the results for the textured Dresselhaus ferromagnet. The results for combined Rashba-Dresselhaus SO coupling are less straightforward to obtain since the dispersion of the carriers changes.

Another obvious place to look for the appearance of additional torques due to SO coupling would be in dilute magnetic semiconductor systems, where the effective Hamiltonian for the carriers also has strong SO coupling. In Ref. [112] spin torques for the dilute limit are calculated for this system. In that work one of the current-induced torques is interpreted as an anisotropic dissipative STT. This anisotropic torque can as well be interpreted as the torque given by Eq. (3.15). It would be very interesting to see which other torques would appear in those systems.

The reciprocal physical mechanism associated with current-induced torques are currents driven by non-equilibrium magnetization dynamics, often referred to as spin-motive forces. We obtain these using the Onsager reciprocal relations [43]. We do this via the linear response matrix

$$\begin{pmatrix} \dot{m}^i \\ j_c^i \end{pmatrix} = \begin{pmatrix} m^k \epsilon^{ijk} & L_{\text{cit}}^{ij}(\boldsymbol{m}, \boldsymbol{e}_z, \nabla \boldsymbol{m}) \\ L_{\text{smf}}^{ij}(\boldsymbol{m}, \boldsymbol{e}_z \nabla \boldsymbol{m}) & \sigma^{ij}(\boldsymbol{m}, \boldsymbol{e}_z, \nabla \boldsymbol{m}) \end{pmatrix} \cdot \begin{pmatrix} H_{\text{eff}}^j \\ E^j \end{pmatrix},$$

where $L_{\text{cit}}^{ij}(\boldsymbol{m}, \boldsymbol{e}_z, \nabla \boldsymbol{m})$ is the (3×3) matrix that gives the current induced torques as defined in Eq. (3.7) and $L_{\text{smf}}^{ij}(\boldsymbol{m}, \boldsymbol{e}_z, \nabla \boldsymbol{m})$ gives the spin motive forces. These two matrices are related via Onsager reciprocity which yields

$$L_{\text{cit}}^{ij}(\boldsymbol{m}, \boldsymbol{e}_z, \nabla \boldsymbol{m}) = L_{\text{smf}}^{ji}(-\boldsymbol{m}, \boldsymbol{e}_z, -\nabla \boldsymbol{m}).$$

3.8 Conclusion

We considered current-induced torques in systems that have SO coupling and a textured magnetization. The effects of these torques on domain-wall motion have been investigated. We have shown that the effects of the interplay between the SO coupling and the gradients in the magnetization are qualitatively important for domain-wall dynamics. In particular, we showed that the inclusions of all torques typically changes the domain-wall mobility as compared to including only the spin transfer torques that occur at weak spin-orbit coupling and/or the homogeneous spin torques due to SO coupling. The results of this work may be used to discriminate between Rashba SO coupling and injection of a spin current via the spin Hall effect, because the latter will only show the homogeneous current-induced torques.

In future work we intend to explore the spin motive forces that arise due to SO coupling in more detail. Another interesting direction for future research is the inclusion of thermal gradients and heat currents.

3.A Different domain-wall configurations

In this appendix we give the equations of motion for the Bloch(x) and Bloch(y) domain-wall configurations. The magnetic anisotropy configuration corresponding to these different walls is given in Table 3.1.

Bloch(x) Wall

The Bloch(x) wall is parameterized as

$$\boldsymbol{m} = (\cos(\theta(\boldsymbol{x},t)), \cos\varphi_{\mathrm{dw}}(\boldsymbol{x},t)\sin(\theta(\boldsymbol{x},t)), \sin\varphi_{\mathrm{dw}}(\boldsymbol{x},t)\sin(\theta(\boldsymbol{x},t)))^T.$$

The equations of motion are obtained as explained in Sec. 3.6 of the main text. The equations of motion for the collective coordinates are given by

$$\begin{aligned}\frac{\dot{r}_{\mathrm{dw}}}{\lambda_{\mathrm{dw}}} - \alpha'_G\dot{\varphi}_{\mathrm{dw}} = \frac{K_\perp}{\hbar}\sin\varphi_{\mathrm{dw}} \\ - \left(\tau^{(1\perp)} + \frac{1}{3\lambda_{\mathrm{dw}}}\tau^{\mathrm{e}}\cos^2\varphi_{\mathrm{dw}} + \frac{\pi}{4\lambda_{\mathrm{dw}}}\left(\tau^{\mathrm{AH}} - \tau^{\mathrm{b}} + \tau^{\mathrm{Hall}}\right)\sin\varphi_{\mathrm{dw}}\right) E\sin\phi_E \\ - \left(\frac{\pi}{2}\tau^{(1)}\sin\varphi_{\mathrm{dw}} + \frac{1}{3\lambda_{\mathrm{dw}}}\left(\tau^{\mathrm{b}\perp} + \tau^{\mathrm{d}} - 2\tau^{\mathrm{AMR}}\right)\cos^2\varphi_{\mathrm{dw}}\right. \\ \left. - \frac{1}{3\lambda_{\mathrm{dw}}}(3\tau^{\mathrm{a}} + \tau^{\mathrm{c}})\sin^2\varphi_{\mathrm{dw}} + \frac{\tau^{STT}}{\lambda_{\mathrm{dw}}}\right) E\cos\phi_E,\end{aligned}$$

$$\begin{aligned}\dot{\varphi}_{\mathrm{dw}} + \alpha'_G\frac{\dot{r}_{\mathrm{dw}}}{\lambda_{\mathrm{dw}}} = \left(\frac{\pi}{2}\left(\frac{1}{2}\tau^{\mathrm{e}} - \lambda_{\mathrm{dw}}\tau^{(1\perp)}\right)\sin\varphi_{\mathrm{dw}}\right. \\ \left. - \frac{1}{3}\left(\left(2\tau^{\mathrm{AMR}} + \tau^{\mathrm{b}}\right)\cos^2\varphi_{\mathrm{dw}} - \left(-3\tau^{\mathrm{a}\perp} + \tau^{\mathrm{f}}\right)\sin^2\varphi_{\mathrm{dw}}\right) + \tau^{\mathrm{STT}\perp}\right)\frac{E\cos\phi_E}{\lambda_{\mathrm{dw}}} \\ + \left(\tau^{(1)} + \frac{\pi}{16\lambda_{\mathrm{dw}}}\left(4\tau^{\mathrm{AH}\perp} - 4\tau^{\mathrm{b}\perp} - \tau^{\mathrm{c}} - \tau^{\mathrm{d}}\right)\sin\varphi_{\mathrm{dw}}\right) E\sin\phi_E.\end{aligned}$$

Bloch(y) Wall

For the Bloch(y) wall the magnetization is parameterized as

$$\boldsymbol{m} = (\cos\varphi_{\mathrm{dw}}(\boldsymbol{x},t)\sin(\theta(\boldsymbol{x},t)), \cos(\theta(\boldsymbol{x},t)), \sin\varphi_{\mathrm{dw}}(\boldsymbol{x},t)\sin(\theta(\boldsymbol{x},t)))^T.$$

The equations of motion are

$$\begin{aligned}\frac{\dot{r}_{\mathrm{dw}}}{\lambda_{\mathrm{dw}}} - \alpha'_G\dot{\varphi}_{\mathrm{dw}} - \frac{K_\perp}{\hbar}\sin 2\varphi_{\mathrm{dw}} = \\ \frac{1}{3\lambda_{\mathrm{dw}}}\left(\tau^{\mathrm{AMR}} - 2\tau^{\mathrm{b}} - 3\tau^{\mathrm{STT}} - \tau^{\mathrm{d}}\sin^2\varphi_{\mathrm{dw}} + 3\lambda_{\mathrm{dw}}\tau^{(1)\perp}\right)E\cos\phi_E \\ -\left(\frac{2}{3\lambda_{\mathrm{dw}}}\tau^{\mathrm{e}} + \frac{\pi}{4}\left(\tau^{\mathrm{AH}} - \tau^{\mathrm{a}\perp} + \tau^{\mathrm{Hall}} + 2\lambda_{\mathrm{dw}}\tau^{(1)}\right)\cos\varphi_{\mathrm{dw}}\right)E\sin\phi_E,\end{aligned}$$

$$\begin{aligned}\dot{\varphi}_{\mathrm{dw}} + \alpha'_G\frac{\dot{r}_{\mathrm{dw}}}{\lambda_{\mathrm{dw}}} = \\ -\frac{1}{3\lambda_{\mathrm{dw}}}\left(\tau^{\mathrm{AMR}\perp} + 2\tau^{\mathrm{b}} + 3\lambda_{\mathrm{dw}}\tau^{(1)} - 3\tau^{\mathrm{STT}\perp} - \tau^{\mathrm{f}}\cos^2\varphi_{\mathrm{dw}}\right)E\cos\phi_E \\ +\frac{\pi}{32\lambda_{\mathrm{dw}}}\left(8\tau^{\mathrm{a}} + 8\tau^{\mathrm{AH}\perp} + \tau^{\mathrm{c}} + \tau^{\mathrm{d}} - 16\lambda_{\mathrm{dw}}\tau^{(1\perp)} - (\tau^{\mathrm{c}} + \tau^{\mathrm{d}})\cos 2\varphi_{\mathrm{dw}}\right)\cos\varphi_{\mathrm{dw}}E\sin\phi_E.\end{aligned}$$

Chapter 4

Thermal spin torques in Rashba ferromagnets

Abstract

In a ferromagnet with spin-orbit coupling a uniform spin polarization accompanies an electric current. This spin polarization exerts a torque on the magnetization. These new types of current-induced torques are known as spin-orbit torques. In this Chapter, we consider spin-orbit torques induced by a temperature gradient, microscopically. A general formula is obtained that relates thermally induced torques to electrically induced torques, which reduces to the so-called Mott formula at low temperature. Furthermore, as an application, we consider heat production at ferromagnetic resonance in the presence of these additional torques.

4.1 Introduction

Spin caloritronics is the field connecting spintronics and thermoelectrics. Where spintronics investigates the manipulation of spin (polarized) currents and magnetization dynamics via applied voltages and vice versa, spin caloritronics adds heat flow and temperature gradients to its object of study [37]. It is the logical extension of spintronics since dissipation of energy associated with electron transport or magnetization dynamics leads to local heating in the mesoscopic or nanoscale devices. The richness of the field's physical content is reflected by the list of phenomena studied recently of which some are thought to be technological relevant. Examples are the spin Seebeck effect [113], thermal spin torques [114] and the spin-dependent Seebeck and Peltier effects [115] that can also be studied in the context of cold atoms [116].

Charge currents can induce magnetization dynamics via spin transfer torques [7, 8, 15, 17, 40, 41, 94–96]. These torques result from the adiabatic following of the magnetization texture by the spins transported by the current. This process can be viewed as adaptation of the spins to the local magnetization. Rashba spin-orbit (SO) coupling gives rise, in the presence of a current, to a momentum dependent preferential direction of spins. The orientation of the spins in the direction of the SO field, which can be seen as a local adaptation of the spins in momentum space, causes a spin torque [32, 33, 39, 101, 102]. In contrast to the well known spin transfer torques these torques are present in monodomain

ferromagnets. In the previous Chapter it was shown that in the presence of SO coupling and an inhomogeneous magnetization, allows for many more spin torques to be present in the system[36].

In this work we investigate spin torques induced by a temperature gradient for an homogeneous magnetization in the presence of Rashba SO coupling. In addition, we study the contribution of the Rashba SO torques on dissipation in the ferromagnet which could be used to determine the magnitude of the thermal SO torque parameters.

Within the *s-d* model the Landau-Lifshitz-Gilbert (LLG) equation has an additional-effective field contribution coming from the induced spin density of the transport *s*-electrons. This non-equilibrium spin-density can be induced either electrically or thermally. The LLG equation augmented with the additional spin torques is given by

$$\dot{\boldsymbol{m}} = -\gamma \boldsymbol{m} \times \mu_0 \boldsymbol{H}_{\text{eff}} + \alpha_G \boldsymbol{m} \times \dot{\boldsymbol{m}} + \boldsymbol{t}_{sd}, \tag{4.1}$$

where $\boldsymbol{m}$ is a unit-vector field representing the localized d-spin direction, which we refer to as the magnetization throughout this Chapter. The first two terms of the above equation represent the precessional torque induced by the effective field and Gilbert damping term, with α_G the damping constant. These terms are present even in the absence of conduction electrons. The third term is given by

$$\boldsymbol{t}_{sd} = \frac{2M}{\hbar^2} \boldsymbol{m} \times \langle \boldsymbol{s} \rangle, \tag{4.2}$$

which is the torque induced by the spin density, given by $\langle \boldsymbol{s} \rangle \equiv \hbar \langle c^\dagger(\boldsymbol{x}) \boldsymbol{\sigma} c(\boldsymbol{x}) \rangle / 2$ where $\boldsymbol{\sigma}$ is the vector of Pauli matrices and $c^{(\dagger)}(\boldsymbol{x})$ are the creation (annihilation) operators for the electrons. The torque is proportional to the exchange coupling of the spins to the magnetization which is taken to be M. The spin density can be induced by applying an electric field or temperature gradient. In linear response we have

$$\langle \hat{s}^i \rangle = L^{ij}_{sc} E^j + L^{ij}_{sQ} \left(-\frac{\nabla^j T}{T} \right), \tag{4.3}$$

where $\boldsymbol{E}$ is the electric field and T is the temperature and we use the summation convention for repeated indices. It is the purpose of this article to calculate the coefficients L^{ij}_{sc} and L^{ij}_{sQ}. We compare the (thermally) induced torques to the induced charge and heat currents. These are given by the linear response relations

$$j^i_c = L^{ij}_{cc} E^j + L^{ij}_{cQ} \left(-\frac{\nabla^j T}{T} \right); \tag{4.4}$$

$$j^i_Q = L^{ij}_{Qc} E^j + L^{ij}_{QQ} \left(-\frac{\nabla^j T}{T} \right), \tag{4.5}$$

where we introduced the matrices L^{ij}_{ab}, with $a, b \in \{c, Q\}$ that describe the thermoelectric response.

We consider a ferromagnet with Rashba-type SO coupling described by the following Hamiltonian,

$$\mathcal{H} = \int d^2\boldsymbol{x}\, h(\boldsymbol{x}), \tag{4.6}$$

where the local energy density operator is given by

$$h(\boldsymbol{x}) = c^\dagger(\boldsymbol{x}) \left\{ -\frac{\hbar^2 \nabla^2}{2m} - M\boldsymbol{m}\cdot\boldsymbol{\sigma} + i\hbar\lambda(\nabla \times \boldsymbol{e}_z)\cdot\boldsymbol{\sigma} + V_{\rm imp}(\boldsymbol{x}) \right\} c(\boldsymbol{x}), \tag{4.7}$$

where m is the mass of the electrons and λ is the strength of the SO coupling, which using this definition has the units of a velocity. In this Chapter, we are interested in a homogeneous magnetization. Therefore, it suffices to consider the case that the magnetization is static and spatially uniform. The impurity potential is given by,

$$V_{\rm imp}(\boldsymbol{x}) = \sum_i u(\boldsymbol{x} - \boldsymbol{R}_i), \tag{4.8}$$

where $\boldsymbol{R}_i$ is the position of the i-th impurity and $u(\boldsymbol{x}) = u_0\delta(\boldsymbol{x})$ is the potential due to a single impurity. The Gaussian average over impurity positions is given by

$$\overline{V_{\rm imp}(\boldsymbol{x})V_{\rm imp}(\boldsymbol{x}')} = n_i u_0^2 \delta(\boldsymbol{x} - \boldsymbol{x}'), \tag{4.9}$$

where n_i is the concentration of the impurities.

In order to calculate the linear response coefficients for the induced spin density and currents we need the charge and energy current operators. These are given by

$$\hat{\boldsymbol{j}}_c(\tau) = -|e| \sum_{\boldsymbol{k}} c^\dagger_{\boldsymbol{k}}(\tau)\hat{\boldsymbol{v}}_{\boldsymbol{k}} c_{\boldsymbol{k}}(\tau); \tag{4.10}$$

$$\hat{\boldsymbol{j}}_E(\tau) = \frac{1}{2}\sum_{\boldsymbol{k}} \lim_{\tau'\to\tau} \left(\partial_{\tau'} - \partial_\tau\right) c^\dagger_{\boldsymbol{k}}(\tau)\hat{\boldsymbol{v}}_{\boldsymbol{k}} c_{\boldsymbol{k}}(\tau'), \tag{4.11}$$

where $|e|$ is the absolute value of the electric charge and the velocity operator has spin structure due to the SO coupling and is given by

$$\hat{\boldsymbol{v}} = \frac{\hbar\boldsymbol{k}}{m} - \frac{1}{\hbar}\frac{\partial}{\partial \boldsymbol{k}}\boldsymbol{\Omega}\cdot\boldsymbol{\sigma} \tag{4.12}$$

where we introduced the vector

$$\boldsymbol{\Omega} = M\boldsymbol{m} - \hbar\lambda\boldsymbol{k}\times\boldsymbol{e}_z,$$

which can be viewed as a momentum dependent exchange field. The definition of the heat-current operator in terms of the imaginary-time derivatives can be understood by using the Schrödinger equation to rewrite the time derivatives in terms of the Hamiltonian. However, the present form serves our purpose better in the calculation of the thermal responses.

4.2 Thermal response

In this Chapter we calculate the thermally induced spin torques and current-densities for systems with SO coupling. These calculations are performed in parallel with the linear response to an electric field $\boldsymbol{E}$. In order to calculate the thermal response using

the Kubo formula we introduce, following Luttinger [91], a gravitational potential $\psi(\boldsymbol{x})$ which couples to the local heat density $Q(\boldsymbol{x}) = h(\boldsymbol{x}) - \mu n(\boldsymbol{x})$, where $n(\boldsymbol{x})$ and $h(\boldsymbol{x})$ are the number density and energy density respectively. With this definition a gradient in the gravitational potential $-\nabla\psi$ drives a heat current $\boldsymbol{j}_Q = \boldsymbol{j}_E - \mu\boldsymbol{j}$ in the system. In the presence of the gravitational potential the local energy density is changed according to[90]

$$h^{\psi}(\boldsymbol{x}) = (h(\boldsymbol{x}) - \mu n(\boldsymbol{x}))\,(1 + \psi(\boldsymbol{x})). \tag{4.13}$$

The linear response of the system in the presence of the gravitational potential can be summarized by the equations

$$\left\langle \hat{s}^i \right\rangle = L_{sc}^{ij}\left(E^j + \frac{1}{|e|}\nabla^j\mu\right) + L_{sQ}^{ij}\left(-\nabla^j\psi - \frac{\nabla^j T}{T}\right); \tag{4.14}$$

$$\left\langle \hat{j}_a^i \right\rangle = L_{ac}^{ij}\left(E^j + \frac{1}{|e|}\nabla^j\mu\right) + L_{aQ}^{ij}\left(-\nabla^j\psi - \frac{\nabla^j T}{T}\right), \tag{4.15}$$

where $\hat{\boldsymbol{j}}_a(\boldsymbol{x})$ with $a \in \{a, Q\}$ can be the charge $\hat{\boldsymbol{j}}_c(\boldsymbol{x})$ or heat $\hat{\boldsymbol{j}}_Q(\boldsymbol{x})$ current density. In the above equations the gravitational field and thermal gradient couple via the same linear response coefficient due to the Einstein relation. Since the gravitational field acts as a mechanical force we can use the standard Kubo formula to calculate the linear response. We can obtain the linear response due to a temperature gradient by the replacement $\nabla\psi \to \nabla T/T$ at the end of the calculation. In order to understand the line of this Chapter we give a preview here to the results of the calculation of the response coefficients using the Kubo formula, which we do in Sec. 4.4.2. For the system we consider, the Kubo formula yields Fermi surface and Fermi sea contributions to the linear response coefficients. The Fermi surface response coefficients for the charge current induced electrically and gravitationally (thermally) are given by

$$L_{cc}^{\text{surface}} = \int d\epsilon \left(-\frac{\partial f}{\partial \epsilon}\right) A(\epsilon); \tag{4.16}$$

$$L_{cQ}^{\text{surface}} = \int d\epsilon \left(-\frac{\partial f}{\partial \epsilon}\right) \epsilon A(\epsilon), \tag{4.17}$$

which are related via the Wiedemann-Franz law and the thermal response vanishes for $T \to 0$, as expected. In the above the function A follows from the microscopic calculation. In addition to the above Fermi surface contributions we obtain Fermi sea terms of the form

$$L_{cc}^{\text{sea}} = \int d\epsilon f(\epsilon)\partial_\epsilon C(\epsilon); \tag{4.18}$$

$$L_{cQ}^{\text{sea}} = \int d\epsilon f(\epsilon)\epsilon\partial_\epsilon C(\epsilon), \tag{4.19}$$

using partial integration these can be brought to the form

$$L_{cc}^{\text{sea}} = \int d\epsilon \left(-\frac{\partial f}{\partial \epsilon}\right) C(\epsilon); \tag{4.20}$$

$$L_{cQ}^{\text{sea}} = \int d\epsilon \left(-\frac{\partial f}{\partial \epsilon}\right) \epsilon C(\epsilon) - \int d\epsilon f(\epsilon) C(\epsilon). \tag{4.21}$$

In the low temperature limit the last term in Eq. (4.21) does not vanish, leading to an unphysical divergence by invoking the Einstein relation $\nabla\psi \to \nabla T/T$. This problematic divergence has to be removed in order to make a theoretical analysis of the response of systems showing these Fermi sea contributions. This issue is rooted in the fact that the charge current also contains unobservable rotating currents in equilibrium that have to be properly subtracted from the Kubo result [89, 90]. Recent progress was made by Qin, Niu and Shi [93] that relate the thermal contributions to the magnetization in the system and give a set of differential equations for this magnetization, for details see their paper[93]. We follow their approach and sketch their argument here.

Consider the charge current for a system in equilibrium and in the absence of external fields. Since we should have a divergenceless expectation value of the current, thus $\nabla \cdot \boldsymbol{j}_c^0 = 0$, we write down the contribution to the current

$$\boldsymbol{j}_c^0 = \nabla \times \boldsymbol{M}^0(\mu, T), \tag{4.22}$$

as the curl of the equilibrium orbital magnetization $\boldsymbol{M}^0$, which does not contribute to transport. The introduction of the gravitational potential (see Eq. (4.13)) modifies the definition of the charge current, such that $\boldsymbol{j}_c^\psi = (1+\psi)\boldsymbol{j}_c^0$. A gradient in the gravitational potential, with the addiational contribution to the current as given in Eq. (4.22), induces a current via

$$\boldsymbol{j}_c^\psi = L_{cQ}(-\nabla\psi) + (1+\psi)\nabla \times \boldsymbol{M}^0(\mu, T); \tag{4.23}$$

$$= \left(L_{cQ} + \boldsymbol{M}^0\times\right)(-\nabla\psi) + \nabla \times \boldsymbol{M}^\psi(\mu, T), \tag{4.24}$$

where in the second line we defined $\boldsymbol{M}^\psi(\mu, T) = (1+\psi)M^0(\mu, T)$. The last term in the above equation is the equilibrium current that does not contribute to transport in the presence of the gravitational potential. However, due to the presence of this term we find a correction to the linear response coefficient coming from the Kubo formula. Below we show that this term precisely cancels the divergent contribution in the Fermi sea term. The magnetization that we introduced in Eq. (4.22) can be calculated using static response theory[93, 117]. Thus in the presence of a temperature gradient or a gradient in the chemical potential the expectation values of the spin density and current densities consist of two parts

$$\langle \hat{\boldsymbol{s}} \rangle = \langle \hat{\boldsymbol{s}} \rangle_{\text{leq}} + \langle \hat{\boldsymbol{s}} \rangle_{\text{kubo}}; \tag{4.25}$$

$$\langle \hat{\boldsymbol{j}}_a \rangle = \langle \hat{\boldsymbol{j}}_a \rangle_{\text{leq}} + \langle \hat{\boldsymbol{j}}_a \rangle_{\text{kubo}}, \tag{4.26}$$

where the first parts with subscript "leq" lead to the correction terms that remove the unphysical divergences from the Kubo formula. In the next Section we use static response theory to calculate the orbital magnetization and an analogous quantity that is associated with the induced spin density.

4.3 Local equilibrium components

In the previous Section we introduced the problem of the divergent contributions that appear using the Kubo formula. In this Section we will calculate the magnetization $\boldsymbol{M}^0(\mu, T)$ and spin current $\mathcal{J}_s^{0;ij}(\mu, T)$ that lead to the correction terms that remove the divergences in the calculations for the charge current and spin density respectively. Note that this spin current will turn out to have the form of a spin current in momentum space.

Using static response theory[93, 117] we calculate the local equilibrium response to small *static* variations in the chemical potential $\mu(\boldsymbol{x}) \approx \mu_0 + \delta\mu(\boldsymbol{x})$ and temperature $1/T(\boldsymbol{x}) \approx 1/T_0 + \delta(1/T(\boldsymbol{x}))$. Application of static response theory yields

$$\begin{aligned}
\langle \hat{\boldsymbol{s}}(\boldsymbol{x})\rangle_{\text{leq}} &= \langle \hat{\boldsymbol{s}}(\boldsymbol{x})\rangle_0 + \int d\boldsymbol{x}' \left\{ \boldsymbol{\chi}_{sc}(\boldsymbol{x},\boldsymbol{x}')\delta\mu(\boldsymbol{x}') - \boldsymbol{\chi}_{sQ}(\boldsymbol{x},\boldsymbol{x}')T_0\delta\left(\frac{1}{T(\boldsymbol{x}')}\right)\right\};\\
\langle \hat{\boldsymbol{j}}_a(\boldsymbol{x})\rangle_{\text{leq}} &= \langle \hat{\boldsymbol{j}}_a(\boldsymbol{x})\rangle_0 + \int d\boldsymbol{x}' \left\{ \boldsymbol{\chi}_{ac}(\boldsymbol{x},\boldsymbol{x}')\delta\mu(\boldsymbol{x}') - \boldsymbol{\chi}_{aQ}(\boldsymbol{x},\boldsymbol{x}')T_0\delta\left(\frac{1}{T(\boldsymbol{x}')}\right)\right\},
\end{aligned}$$

where the first terms in both equations just correspond to the expectation values for systems with constant chemical potential μ_0 and temperature T_0 and we introduced the static response functions $\boldsymbol{\chi}(\boldsymbol{x},\boldsymbol{x}')$, which are given by,

$$\boldsymbol{\chi}_{sa}(\boldsymbol{x},\boldsymbol{x}') \equiv \beta \langle \Delta\hat{\boldsymbol{s}}(\boldsymbol{x})\Delta\hat{n}_a(\boldsymbol{x}')\rangle_0\,; \tag{4.27}$$

$$\boldsymbol{\chi}_{ba}(\boldsymbol{x},\boldsymbol{x}') \equiv \beta \left\langle \Delta\hat{\boldsymbol{j}}_b(\boldsymbol{x})\Delta\hat{n}_a(\boldsymbol{x}')\right\rangle_0, \tag{4.28}$$

where $a, b \in \{c, Q\}$ and $\Delta\hat{n}_c = \hat{n} - n$ is the density operator minus its expectation value, and a similar expression holds for the energy density $\Delta\hat{n}_Q$. Note the difference with the ordinary response functions. Expansion of the the Fourier transform of the static response function $\boldsymbol{\chi}_{ab}(\boldsymbol{q})$ up to first order in momentum as $\chi^i_{ab}(\boldsymbol{q}) \approx \chi^i_{ab}(0) + (iq^j)\chi^{ij}_{ab}$ yields the response to a gradient in the perturbations, where we have defined

$$\chi^{ij}_{ab} \equiv -i\left.\frac{\partial\chi^i_{ab}}{\partial q^j}\right|_{\boldsymbol{q}=0}. \tag{4.29}$$

Using the above definitions we can write for the static response function for the spin density with respect to variations in the chemical potential

$$\chi^{ij}_{sc} = -i\beta\frac{\partial}{\partial q^j}\sum_{\boldsymbol{k}}\left\langle \hat{s}^i(\boldsymbol{k}+\boldsymbol{q})\hat{n}(\boldsymbol{k}-\boldsymbol{q})\right\rangle_0, \tag{4.30}$$

which yields

$$\chi^{ij}_{sc} = -\hbar\int_{-\infty}^{\infty}\frac{d\epsilon}{2\pi}f(\epsilon)\text{Im}\sum_{\boldsymbol{k}}\text{tr}\left[\Lambda^i_s\frac{\partial\mathcal{G}^R_{\boldsymbol{k}}}{\partial k^j}\Lambda_0\mathcal{G}^R_{\boldsymbol{k}} - \Lambda^i_s\mathcal{G}^R_{\boldsymbol{k}}\Lambda_0\frac{\partial\mathcal{G}^R_{\boldsymbol{k}}}{\partial k^j}\right], \tag{4.31}$$

where we introduced the retarded Green's function $\mathcal{G}^R_{\boldsymbol{k}}(\epsilon)$ and the vertices Λ_0 and Λ^i_s for the density and spin density vertex respectively. Note that in the absence of disorder these

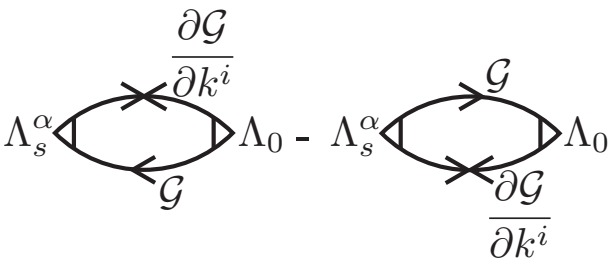

Figure 4.1: Bubble diagrams contributing to the static response functions.

reduce to $\Lambda_0 = 1$ and $\Lambda_s^i = \hbar\sigma^i/2$. In Fig. 4.1 we show the diagrammatic representation of the above equation, note that the Green's functions both depend on the same Matsubara frequency, this in contrast to the usual Kubo formula where we have an external frequency for one of the Green's functions. The cross on the full propagator means $\partial\mathcal{G}/\partial k^j$. For the thermal response we need to include an additional energy factor ϵ that comes from the energy density $\Delta\hat{n}_Q$. We have similar expressions for the (heat) current density.

We evaluate the above expression in the absence of disorder. The Rashba Hamiltonian has the energy eigenvalues

$$\epsilon_{\boldsymbol{k}\sigma} = \frac{\hbar^2\boldsymbol{k}^2}{2m} - \sigma|\boldsymbol{\Omega}(\boldsymbol{k})|, \tag{4.32}$$

where $\sigma = \pm 1$. Using the associated retarded Green's function Eq. (4.31) results in

$$\langle\hat{\boldsymbol{s}}\rangle \;=\; \frac{\hbar}{4}\sum_{\boldsymbol{k}\sigma}\frac{\sigma}{|\boldsymbol{\Omega}(\boldsymbol{k})|}f(\beta(\epsilon_{\boldsymbol{k},\sigma}-\mu))\left(\frac{\partial\hat{\boldsymbol{\Omega}}}{\partial k^j}\times\hat{\boldsymbol{\Omega}}\right)(\nabla^j\mu), \tag{4.33}$$

where we used the notation $\hat{\boldsymbol{\Omega}} = \boldsymbol{\Omega}/|\boldsymbol{\Omega}|$ for unit vectors. The local equilibrium contribution coming from the variation of the temperature $T(\boldsymbol{x})$ has a similar expression, both results can be summarized by

$$\langle\hat{s}^i\rangle_{\rm leq} = \nabla^j\mathcal{J}_s^{ij}(\mu(\boldsymbol{x}), T(\boldsymbol{x})), \tag{4.34}$$

where the right-hand side can be interpreted as the divergence of the equilibrium spin current density, which is defined as

$$\mathcal{J}_s^{ij}(\mu,T) = \frac{\hbar}{4\beta}\sum_{\boldsymbol{k},\sigma}\sigma\frac{1}{|\boldsymbol{\Omega}(\boldsymbol{k})|}\log(1+e^{-\beta(\epsilon_{\boldsymbol{k}\sigma}-\mu)})\left(\frac{\partial\hat{\boldsymbol{\Omega}}}{\partial k^j}\times\hat{\boldsymbol{\Omega}}\right)^i. \tag{4.35}$$

For the current we obtain the result,

$$\langle j_c^i\rangle_{\rm leq} = \nabla\times\boldsymbol{M}(\mu(\boldsymbol{x}), T(\boldsymbol{x})), \tag{4.36}$$

with the orbital magnetization

$$M^c(\mu,T) = \frac{|e|}{\hbar\beta}\frac{\epsilon^{abc}}{2}\sum_{\boldsymbol{k}\sigma}\sigma\log\left(1+e^{-\beta(\epsilon_{\boldsymbol{k}\sigma}-\mu)}\right)\left(\frac{\partial\hat{\boldsymbol{\Omega}}}{\partial k^a}\times\frac{\partial\hat{\boldsymbol{\Omega}}}{\partial k^b}\right)\cdot\hat{\boldsymbol{\Omega}}, \tag{4.37}$$

that was obtained before [87, 92, 93]. The expression for the spin current $\mathcal{J}_s^{ij}(\mu, T)$ is one of the main results of this Chapter. We shall see below that this equilibrium spin current removes the divergent terms from the Kubo formula, similar to the way in which divergent contributions to the charge current density are removed [93].

Note that the orbital magnetization is related to the anomalous Hall effect, as we have shown Chapter 2. That is, it results in a transport current perpendicular to the applied electric field that does not depend on the relaxation in the system, *i.e.* it is intrinsic. Likewise, the induced spin density that comes from the equilibrium spin current density in momentum space results in an intrinsic spin torque. We already obtained such an intrinsic spin torque in Chapter 3, it is further discussed in Ref. [110].

4.4 Calculations

In this Section we use the Kubo formula to calculate the (thermal) spin torques for the Rashba ferromagnet. We will show that the divergent contributions that will be obtained using the Kubo formula are exactly canceled by the contributions from the local-equilibrium expectation values. Moreover, we explicitly include the effects of disorder using the first-order Born approximation for the self-energy and take the magnetization in the z-direction. We first calculate the disorder averaged Green's function.

4.4.1 Green's function

The Green's function including self-energy, $\Sigma = \Sigma_0 \mathbf{1} + \boldsymbol{\Sigma} \cdot \boldsymbol{\sigma}$, is given by

$$\begin{aligned} \mathcal{G}_{\boldsymbol{k}}(i\hbar\omega_n) &= [i\hbar\omega_n - (\mathcal{H}_R - \mu) - \Sigma(i\hbar\omega_n)]^{-1} \\ &\equiv D_{\boldsymbol{k}}(i\omega_n)\left(g_0(i\omega_n, \boldsymbol{k})\mathbf{1} + \boldsymbol{g}(i\omega_n, \boldsymbol{k}) \cdot \boldsymbol{\sigma}\right), \end{aligned} \tag{4.38}$$

where we introduced the functions

$$g_0(i\hbar\omega_n, \boldsymbol{k}) = i\hbar\omega_n + \mu - \frac{\hbar^2 \boldsymbol{k}^2}{2m} - \Sigma_0(i\hbar\omega_n); \tag{4.39}$$

$$\boldsymbol{g}(i\hbar\omega_n, \boldsymbol{k}) = -(\boldsymbol{\Omega}(\boldsymbol{k}) - \boldsymbol{\Sigma}(i\hbar\omega_n)); \tag{4.40}$$

$$D_{\boldsymbol{k}}(i\omega_n) = (g_0^2 - \boldsymbol{g}^2)^{-1}. \tag{4.41}$$

We calculate the self-energy in first-order Born approximation

$$\Sigma^{\pm}(\epsilon) = n_i u_0^2 \sum_{\boldsymbol{k}} \mathcal{G}^{\pm}_{0;\boldsymbol{k}}(\epsilon), \tag{4.42}$$

where $\pm$ denote the retarded (+) and advanced (-) branches that come form the analytic continuation $i\hbar\omega_n \to \epsilon \pm i\eta$. Note that $\hat{\mathcal{G}}^{\pm}_{0;\boldsymbol{k}}$ is the disorder free version of the self-energy. Also note that the self-energy only depends on the energy ϵ and not on momentum $\boldsymbol{k}$. We are only interested in the imaginary part of the self-energy, since the real part can be absorbed in the definition of the chemical potential. The imaginary part of the self-energy

is given by $\Sigma^{\pm}(\epsilon) = i\gamma_0^{\pm}(\epsilon) + i\gamma_z^{\pm}(\epsilon)\sigma_z$. We have

$$\begin{aligned}\gamma_0^{\pm}(\epsilon) &= \pm\gamma\frac{\epsilon+\mu}{\Delta_0}\left[\Theta(\zeta_{0+}) - \mathrm{sign}(M+(\mu+\epsilon))\Theta(\zeta_{0-})\right] \\ &\mp \frac{\gamma}{\Delta_0}\left(\zeta_{0+}\Theta(\zeta_{0+}) - \mathrm{sign}(M+(\mu+\epsilon))\zeta_{0-}\Theta(\zeta_{0-})\right); \\ \gamma_z^{\pm}(\epsilon) &= \mp\frac{\gamma M}{\Delta_0}\left[\Theta(\zeta_{0+}) - \mathrm{sign}(M+(\mu+\epsilon))\Theta(\zeta_{0-})\right],\end{aligned} \tag{4.43}$$

where the scattering rate

$$\hbar\gamma = \frac{n_i u_0^2 m}{\pi^2\hbar}, \tag{4.44}$$

and Δ_0 is defined in the appendix to this Chapter using Eq. (4.107) with $\gamma_0, \gamma_z = 0$. We obtained these results using the integrals in appendix 4.B. In real systems the spin-orbit coupling energy $m\lambda^2 \ll M$, so that

$$\Theta(\zeta_{0+}) - \mathrm{sign}(M+(\mu+\epsilon))\Theta(\zeta_{0-}) = \Theta(M^2 - (\epsilon+\mu)^2).$$

In Fig. 4.2 we show the results for the function γ_0 and γ_z as a function of the chemical potential for the two distinct cases $m\lambda^2 < M$ and $m\lambda^2 > M$, below we show the dispersion of the Rashba ferromagnet with the magnetization in the z-direction. Note that in the first-order Born approximation that we use here, even weak disorder scattering leads to large imaginary parts of the self-energy when the energy associated with SO coupling is larger than the exchange coupling $m\lambda^2 > M$. For a consistent treatment of this regime a more elaborate approximation seems necessary. However, since this is not the regime of interest we drop this issue for the remainder of this Chapter.

Below, we prove that the local equilibrium contribution exactly cancels the divergent Fermi sea contribution. In this proof we need the appropriate vertex corrections that we define here

$$\Lambda_a = \Lambda_{0,a} + n_i u_0^2 \sum_{\boldsymbol{k}} \mathcal{G}_{\boldsymbol{k}}\Lambda_a\mathcal{G}_{\boldsymbol{k}}, \tag{4.45}$$

where $\Lambda_{0,a}$ is the bare vertex. Note that this is an equation of 2×2 matrices. We use the notation Λ_s^i for the spin vertex with $\Lambda_{0,s}^i = \hbar\sigma^i/2$, Λ_c^i for the currents with $\Lambda_{c,0}^i = -|e|v^i$, where the velocity is given by Eq.(4.12). The results we present in Sec. 4.5 are obtained without vertex corrections, we will motivate this later in this Chapter.

4.4.2 Kubo-formula

The linear response coefficients for the spin density with respect to the mechanical perturbations E_j and $-\nabla_j\psi$ are given by the standard Kubo formula

$$L_{sb,\,\mathrm{kubo}}^{ij} = \lim_{\omega\to 0}\frac{K_{sb}^{ij}(\omega+i0) - K_{sb}^{ij}(0)}{i\omega}; \tag{4.46}$$

$$\tag{4.47}$$

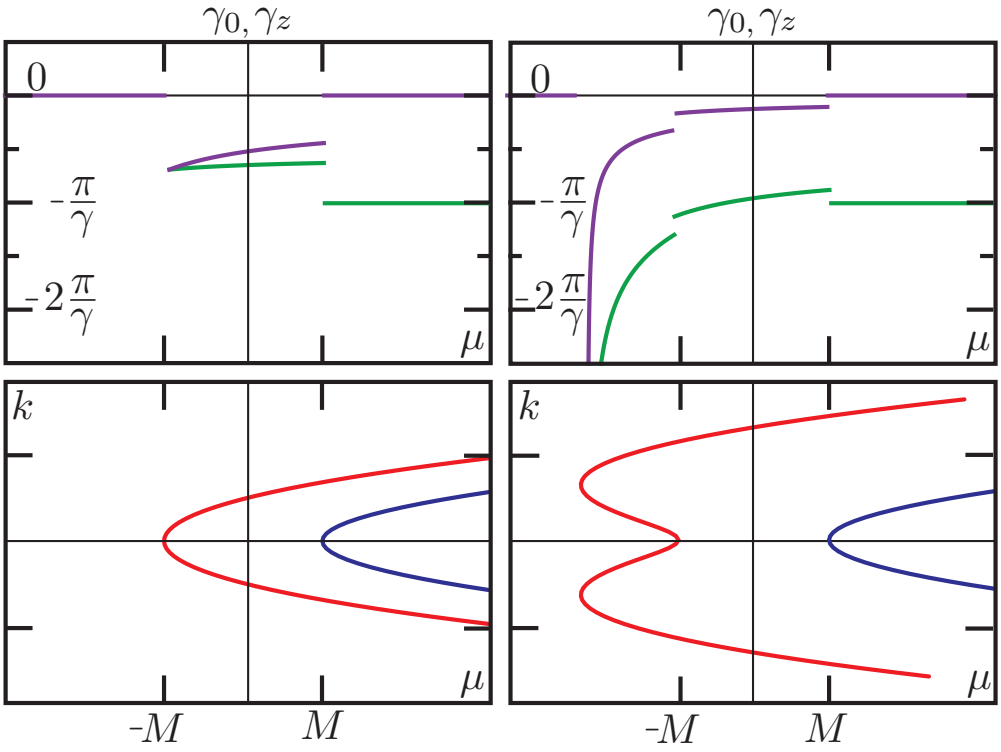

Figure 4.2: Imaginary part of the self-energy in first Born approximation (top) and dispersion (bottom) of the Rashba ferromagnet with $\boldsymbol{m} = \boldsymbol{e}_z$ for $m\lambda^2 < M$ (left) and $m\lambda^2 > M$ (right). The green line represents γ_0 and the purple line represents γ_z.

where the response functions are given by

$$K_{sb}^{\alpha j}(i\omega_\lambda) = \int_0^{\hbar\beta} d\tau e^{i\omega_\lambda \tau} \langle T_\tau \hat{s}^\alpha(\tau) \hat{J}_b^j(0) \rangle, \tag{4.48}$$

and a similar expression for the currents in terms of K_{ab}^{ij} defined via

$$K_{ab}^{ij}(i\omega_\lambda) = \int_0^{\hbar\beta} d\tau e^{i\omega_\lambda \tau} \langle T_\tau \hat{J}_a^i(\tau) \hat{J}_b^j(0) \rangle, \tag{4.49}$$

where $\hat{\boldsymbol{J}}_{a,b}$ can represent the charge or heat-current operators. To be clear, the conductivity can be obtained from $K_{cc}^{ij}(i\omega_\lambda)$ and the heat conductivity is obtained from $K_{QQ}^{ij}(i\omega_\lambda)$. In Fig. 4.3 the bubble diagrams that contribute to the response functions as given in Eqs. (4.48,4.49) are shown. These results can be summarized using the function

$$\varphi_{ab}^{ij}(i\omega_n^+, i\omega_n) = \sum_{\boldsymbol{k}} \mathrm{tr}\left[\Lambda_a^i \mathcal{G}_{\boldsymbol{k}}^+ \Lambda_b^j \mathcal{G}_{\boldsymbol{k}}\right], \tag{4.50}$$

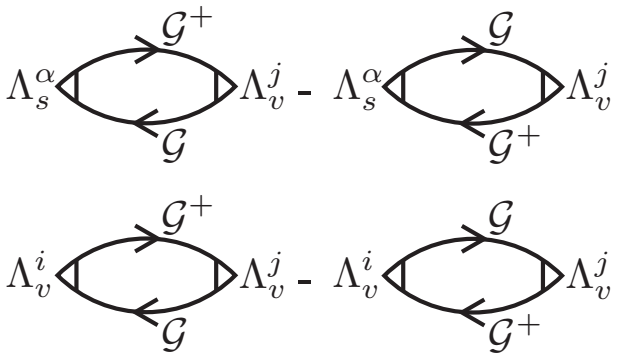

Figure 4.3: Bubble diagrams contributing to the current-spin (top) and current-current (bottom) response functions.

where the Green's function, $\mathcal{G}^+$ is the Green's function with frequency argument $i\omega_n + i\omega_\lambda$ and ω_n are the odd Matsubara frequencies and Λ_a^i denote the different vertices. Which can be the spin vertex Λ_s^i, the current vertex Λ_c^i or the heat-current vertex Λ_Q^i, which is defined as $\Lambda_Q^i = -(i\omega_n + i\omega_\lambda/2)\Lambda_c^i/|e|$. We used the relation

$$\left\langle T_\tau c(\tau)\dot{c}^\dagger \right\rangle = -\left\langle T_\tau \dot{c}(\tau)c^\dagger \right\rangle = \frac{d}{d\tau}\mathcal{G}(\tau) + \delta(\tau),$$

together with the definition of the heat-current density as given in Eq. (4.11) to obtain this result. The response functions can now conveniently be expressed using

$$K_{ab}^{ij}(i\omega_\lambda) = \frac{1}{\beta}\sum_n \varphi_{ab}^{ij}(i\omega_n^+, i\omega_n). \tag{4.51}$$

After the analytic continuation $i\omega_\lambda \to \omega + i0$, up to first order in ω we obtain (suppressing the spatial indices ij)

$$\begin{aligned} & K_{ab}(\omega + i0) - K_{ab}(0) \\ = \; & \frac{i\hbar\omega}{2\pi\beta}\int_{-\infty}^{\infty} d\epsilon \left(-\frac{\partial f}{\partial \epsilon}\right)\left\{\mathrm{Re}\left[\varphi_{ab}^{\mathrm{RR}}(\epsilon,\epsilon)\right] - \varphi_{ab}^{\mathrm{RA}}(\epsilon,\epsilon)\right\} \\ & -\frac{\hbar\omega}{2\pi\beta}\int_{-\infty}^{\infty} d\epsilon f(\epsilon)\,(\partial_\epsilon - \partial_{\epsilon'})\,\mathrm{Im}\left[\varphi_{ab}^{\mathrm{RR}}(\epsilon,\epsilon')\right]\big|_{\epsilon'=\epsilon} \end{aligned} \tag{4.52}$$

where $\varphi_{ab}^{\mathrm{XX}}$ is the analytic continuation of Eq. (4.50) with the superscripts $\mathrm{X} = \mathrm{R}, \mathrm{A}$ denoting the branch, retarded or advanced, of the analytic continuation in the two arguments. Analytic continuation of terms involving the heat-current operator yield $\varphi_{aQ}^{\mathrm{XX}}(\epsilon,\epsilon') = -\frac{1}{2|e|}(\epsilon+\epsilon')\varphi_{ac}^{\mathrm{XX}}(\epsilon,\epsilon')$.

Ward identities

Before we turn to the evaluation of Eq. (4.52) we connect the results of the Kubo formula to the local equilibrium contributions we calculated in the previous Section. Recall that

the Fermi sea contributions in Eq. (4.52) can be represented as

$$L_{sc,\mathrm{Kubo}} = \int d\epsilon f(\epsilon)\partial_\epsilon C(\epsilon); \tag{4.53}$$

$$L_{sQ,\mathrm{Kubo}} = \int d\epsilon f(\epsilon)\epsilon\partial_\epsilon C(\epsilon), \tag{4.54}$$

where we implicitly defined $\partial_\epsilon C(\epsilon)$. The term that causes the divergence is then given by

$$\int d\epsilon f(\epsilon) C(\epsilon). \tag{4.55}$$

From the discussion in the previous Section we know that the linear response coefficient for the spin density induced by a temperature gradient should be defined as

$$L_{sQ}^{ij} - \mathcal{J}_s^{ij}, \tag{4.56}$$

where $\mathcal{J}_s^{ij}$ is obtained from the static response function, see Eq. (4.31), and is given by

$$\mathcal{J}_s^{ij} = \int_{-\infty}^{\mu} d\mu' \int_{-\infty}^{\infty} \frac{d\epsilon}{2\pi} f(\epsilon) \mathrm{Im} \sum_{\boldsymbol{k}} \mathrm{tr}\left[\Lambda_s^i \frac{\partial \mathcal{G}_{\boldsymbol{k}}^R}{\partial k^j} \Lambda_0 \mathcal{G}_{\boldsymbol{k}}^R - \Lambda_s^i \mathcal{G}_{\boldsymbol{k}}^R \Lambda_0 \frac{\partial \mathcal{G}_{\boldsymbol{k}}^R}{\partial k^j}\right], \tag{4.57}$$

which follows from Eq. (4.34). Note that we implicitly assume that the integral over the chemical potential converges. We claim that this contribution precisely cancels the divergent contribution and show this by considering the trace in Eq. (4.57), which can be manipulated as

$$\begin{aligned}
& \mathrm{tr}\left[\Lambda_a^i \frac{\partial \mathcal{G}}{\partial k^j} \Lambda_0 \mathcal{G} - \Lambda_0 \frac{\partial \mathcal{G}}{\partial k^j} \Lambda_a^i \mathcal{G}\right] \\
= \; & \mathrm{tr}\left[\Lambda_a^i \frac{\partial \mathcal{G}}{\partial k^j} \mathcal{G}^{-1} \frac{\partial \mathcal{G}}{\partial \epsilon} - \frac{\partial \mathcal{G}}{\partial k^j} \Lambda_a^i \frac{\partial \mathcal{G}}{\partial \epsilon} \mathcal{G}^{-1}\right] \\
= \; & \mathrm{tr}\left[\Lambda_a^i \mathcal{G} \Lambda_c^j \frac{\partial \mathcal{G}}{\partial \epsilon} - \Lambda_c^j \mathcal{G} \Lambda_a^i \frac{\partial \mathcal{G}}{\partial \epsilon}\right] \\
= \; & \mathrm{tr}\left[\left(\Lambda_a^i \mathcal{G} \Lambda_c^j - \Lambda_c^j \mathcal{G} \Lambda_a^i\right) \frac{\partial \mathcal{G}}{\partial \epsilon}\right],
\end{aligned} \tag{4.58}$$

where $a \in \{s, c, Q\}$ represent spin and (heat) current densities, where we used the Ward identities

$$\mathcal{G}\Lambda_0\mathcal{G} = \frac{\partial \mathcal{G}}{\partial \epsilon} \quad ; \quad \mathcal{G}\Lambda_c^i\mathcal{G} = \frac{\partial \mathcal{G}}{\partial k^i}, \tag{4.59}$$

that relate the self-energy and vertex corrections and should hold for a consistent theory that respects the continuity equation. The last line in Eq. (4.58) corresponds to the Fermi sea term in Eq. (4.52). Thus we can express the spin current as

$$\mathcal{J}_s^{ij} = \int_{-\infty}^{\mu} d\mu' \int_{-\infty}^{\infty} \frac{d\epsilon}{2\pi i} f(\epsilon) \partial_\epsilon C(\epsilon), \tag{4.60}$$

where we used the defintion of ∂_ϵ that was implied by Eq. (4.53) from Eq. (4.52). Note that $C(\epsilon)$ is a function of $\epsilon + \mu'$, such that, via partial integration, we obtain

$$\mathcal{J}_s^{ij} = -\int_{-\infty}^{\infty} d\epsilon f(\epsilon) C(\epsilon), \tag{4.61}$$

which exactly cancels the divergent contribution given in Eq. 4.55 as long as the Ward identities are satisfied. Note that for the current and heat currents the subtraction procedure concerning $\boldsymbol{M}$ was already shown before for free fermions [87, 93, 118] and with interactions[92].

In this Section we have developed a general framework to calculate the linear response coefficients for systems with strong SO coupling. Note that the expressions given in this Section did not depend on the precise form of the SO coupling. In the next Section we calculate the torques and currents for the Rashba ferromagnet.

4.5 Results

The main purpose of this Chapter is to investigate thermal spin torques for systems with SO coupling. In the preceding Sections we made progress in the interpretation and handling of the divergences that appear in the naive application of the Kubo formula to systems with SO coupling. In this Section we give explicit results for the Rashba ferromagnet with the magnetization fixed in the z-direction. For this particular model the self-energy associated with disorder scattering is momentum independent, allowing us to safely ignore the vertex corrections without violating the Ward identities.

Recall that the induced torques are found from the induced spin density, see Eq. (4.2). Note that we investigate here the induced torques and not the spin density we discussed in the above for reasons that become clear below. We define

$$\begin{aligned} \boldsymbol{j}_c &= (A_0 - (B_0 - C_0)\, \boldsymbol{e}_z \times)\, \boldsymbol{E} && (4.62)\\ &+ (A_1 - (B_1 - C_1 + c)\, \boldsymbol{e}_z \times)\, (-\boldsymbol{\nabla}\psi), && (4.63) \end{aligned}$$

for the charge current and similar expressions for the heat current given by

$$\begin{aligned} \boldsymbol{j}_Q &= -\frac{1}{|e|}\, (A_1 - (B_1 - C_1 + c_0)\, \boldsymbol{e}_z \times)\, \boldsymbol{E} && (4.64)\\ &+ -\frac{1}{|e|}\, (A_2 - (B_2 - C_2 + c_1)\, \boldsymbol{e}_z \times)\, (-\boldsymbol{\nabla}\psi). && (4.65) \end{aligned}$$

In addition for the torques we define

$$\begin{aligned} \boldsymbol{t}_c &= (A_{s,0} - (B_{s,0} - C_{s,0}) \boldsymbol{e}_z \times)\, (\boldsymbol{E}); && (4.66)\\ \boldsymbol{t}_\psi &= -\frac{1}{|e|}\, (A_{s,1} - (B_{s,1} - C_{1,s} + c_s)\, \boldsymbol{e}_z \times)\, (-\boldsymbol{\nabla}\psi), && (4.67) \end{aligned}$$

where the response coefficients are evaluated below and follow from Eq. (4.52). Since SO coupling couples the spin direction to the motion of the electrons it has to be expected

that the coefficients for charge and heat transport are related to the spin torques. Before we discuss this relation further we define

$$A_n = A_{c,n} - \frac{|e|\hbar\lambda}{Ma^2} A_{s,n}, \tag{4.68}$$

where a is the lattice constant, this factor appears because we compare current densities to the total torque on the magnetization, and similar expressions for the other response coefficients. The functions $A_{a,n}$, $B_{a,n}$ and $C_{a,n}$ are defined as

$$A_{a,n} = \int_{-\infty}^{\infty} d\epsilon \left(-\frac{\partial f}{\partial \epsilon}\right) \epsilon^n A_a(\epsilon), \tag{4.69}$$

for $a \in \{s, c\}$. The divergent terms are given by

$$c_{a,n} = \int_{-\infty}^{\infty} d\epsilon f(\epsilon)(1+n)\epsilon^n C_a(\epsilon).$$

From the above discussion we know how to interprete the contribution c_s and that it is cancelled by the local equilibrium spin-density. In the absence of this term we can safely use the Einstein relation and make the replacement $-\boldsymbol{\nabla}\psi - \boldsymbol{\nabla}T/T$ to obtain the thermal torques. Using the form of Eqs. (4.66) and (4.67) we can relate the thermal torques to the electric torques as

$$\begin{aligned} \boldsymbol{t}_{\text{th}} &= \int d\epsilon \left(-\frac{\partial f}{\partial \epsilon}\right) \epsilon \boldsymbol{t}_c(\epsilon)|_{|e|\boldsymbol{E}\to\boldsymbol{\nabla}T/T} && (4.70) \\ &\approx \frac{\pi^2}{3}(k_B T)^2 \frac{d}{d\epsilon_F} \boldsymbol{t}_c(\epsilon_F)\Big|_{|e|\boldsymbol{E}\to\boldsymbol{\nabla}T/T}, && (4.71) \end{aligned}$$

where the first equality holds at all temperatures and the second line follows from the Sommerfeld approximation at low temperatures.

Before we give the explicit expressions for the linear response coefficients we introduced above we discuss the relation between the torques and currents. As shown by Eq. (4.68) the conductivity of the Rashba ferromagnet receives a contribution from the induced spin density via the SO coupling. To see the origin of this consider the current induced by an electric field, From Eq. (4.68) we see that

$$\boldsymbol{j}_c = \sigma_c \boldsymbol{E} - \frac{|e|\hbar\lambda}{Ma^2} \boldsymbol{t}_c(\boldsymbol{E}), \tag{4.72}$$

where σ_c is the matrix containing all the A_c, B_c and C_c terms and $\boldsymbol{t}(\boldsymbol{E})$ are the electric field induced torques. Since we took the magnetization in the z-direction we have

$$\boldsymbol{t}_c(\boldsymbol{E}) = \frac{2M}{\hbar^2} \boldsymbol{e}_z \times \langle \boldsymbol{s} \rangle(\boldsymbol{E}),$$

which is the contribution to the current coming from the SO coupling. Thus the above relation crucially depends on the magnetization being parallel to the symmetry breaking direction.

The functions $A_a(\epsilon)$ $B_a(\epsilon)$ and $C_a(\epsilon)$ are obtained from Eq. (4.52). They are explicitly given by

$$A_a(\epsilon) = \mathrm{Re}\left[\Gamma_a^{\mathrm{RR}}(\epsilon)\right] - \Gamma_a^{\mathrm{RA}}(\epsilon), \tag{4.73}$$

where

$$\Gamma_c^{\mathrm{RX}} = \frac{\hbar|e|^2}{2\pi\beta}\sum_{\boldsymbol{k}}\left\{\frac{\hbar^2\boldsymbol{k}^2}{m^2}\mathrm{tr}\left[\hat{\mathcal{G}}_{\boldsymbol{k}}^{\mathrm{R}}\hat{\mathcal{G}}_{\boldsymbol{k}}^{\mathrm{X}}\right] - \lambda\frac{\hbar k^i}{m}\mathrm{tr}\left[\hat{\sigma}^j\hat{\mathcal{G}}_{\boldsymbol{k}}^{\mathrm{R}}\hat{\mathcal{G}}_{\boldsymbol{k}}^{\mathrm{X}}\right]\epsilon^{ijz}\right\}; \tag{4.74}$$

$$\Gamma_s^{\mathrm{RX}} = \frac{|e|Ma^2}{2\pi\beta}\sum_{\boldsymbol{k}}\left\{\frac{\hbar k^i}{m}\mathrm{tr}\left[\hat{\sigma}^j\hat{\mathcal{G}}_{\boldsymbol{k}}^{\mathrm{R}}\hat{\mathcal{G}}_{\boldsymbol{k}}^{\mathrm{X}}\right]\epsilon^{ijz} - \lambda\mathrm{tr}\left[\hat{\sigma}^i\hat{\mathcal{G}}_{\boldsymbol{k}}^{\mathrm{R}}\hat{\sigma}^j\hat{\mathcal{G}}_{\boldsymbol{k}}^{\mathrm{X}}\right]\delta_\perp^{ij}\right\}, \tag{4.75}$$

and

$$B_c(\epsilon) = \frac{\hbar|e|^2}{2\pi\beta}\sum_{\boldsymbol{k}}\lambda\frac{\hbar k^i}{m}\mathrm{tr}\left[\hat{\sigma}^j\hat{\mathcal{G}}_{\boldsymbol{k}}^{\mathrm{R}}\hat{\mathcal{G}}_{\boldsymbol{k}}^{\mathrm{A}}\right]\delta_\perp^{ij};$$

$$B_s(\epsilon) = -\frac{|e|Ma^2}{2\pi\beta}\sum_{\boldsymbol{k}}\left\{\frac{\hbar k^i}{m}\mathrm{tr}\left[\hat{\sigma}^j\hat{\mathcal{G}}_{\boldsymbol{k}}^{\mathrm{R}}\hat{\mathcal{G}}_{\boldsymbol{k}}^{\mathrm{A}}\right]\delta_\perp^{ij} - \lambda\mathrm{tr}\left[\hat{\sigma}^i\hat{\mathcal{G}}_{\boldsymbol{k}}^{\mathrm{R}}\sigma^j\hat{\mathcal{G}}_{\boldsymbol{k}}^{\mathrm{A}}\right]\epsilon^{ijz}\right\},$$

where $\delta_\perp^{ij} = \delta^{ij} - \delta^{iz}\delta^{jz}$. Evaluating the trace in these expressions yields

$$A_c(\epsilon) = \frac{|e|^2}{\pi^2\hbar\beta}\mathrm{Re}\big[\tilde{I}_{320} - \tilde{I}_{311} + 2X(\tilde{I}_{211} - \tilde{I}_{220}) \tag{4.76}$$

$$+\tilde{I}_{120}(X(X+2m\lambda^2)+Y^2) - \tilde{I}_{111}(2m\lambda^2X + |X|^2 + |Y|^2)\big]; \tag{4.77}$$

$$A_s(\epsilon) = -\frac{m|e|Ma^2\lambda}{\pi^2\hbar^2\beta}\mathrm{Re}\left[\tilde{I}_{220} - \tilde{I}_{211} - (X^2-Y^2)\tilde{I}_{020} - \tilde{I}_{011}(|Y|^2 - |X|^2)\right] \tag{4.78}$$

where we introduced $X(\epsilon) = \epsilon + \mu - i\gamma_0(\epsilon)$ and $Y(\epsilon) \equiv g_z(\epsilon) = -(M - i\gamma_z(\epsilon))$ and the integrals over momentum are summarized by $\tilde{I}_{lmn}(\epsilon)$ which are defined in the appendix 4.B.

$$B_c(\epsilon) = 2\frac{|e|^2\lambda^2 m}{\pi^2\hbar\beta}\tilde{I}_{111}\gamma_z; \tag{4.79}$$

$$B_s(\epsilon) = 2\frac{m|e|Ma^2\lambda}{\pi^2\hbar^2\beta}\tilde{I}_{011}\left(M\gamma_0 - \mu\gamma_z\right), \tag{4.80}$$

In the low temperature limit the derivative of the Fermi distribution tends to a delta function such that we need to evaluate the above expressions only at $\epsilon = 0$. In Figs. 4.4, 4.5 we show the results of the above Fermi surface torques for weak disorder, $\gamma/M = 0.1$, as a function of μ/M for various strengths of the SO coupling parameterized by the ratio $m\lambda^2/M$. We show the functions in dimensionless units at zero temperature, which are related to the above expressions via $A_s(0) = a^2m|e|\lambda\tilde{A}_s(0)/\pi^2\hbar^2$, and $B_s(0) = a^2m|e|\lambda\tilde{B}_s(0)/\pi^2\hbar^2$. Note that the torque in the direction of the applied electric field is scales as $1/\gamma = \tau_s/\hbar$ where τ_s is the scattering time. The perpendicular, *i.e.* B_s, term is intrinsic, that is, it is also present in the absence of disorder. Note that the Fermi surface torques vanish when $\lambda = 0$ as should be expected, which can be seen by the prefactor for the dimensionless parameters. Note that we only shown results for

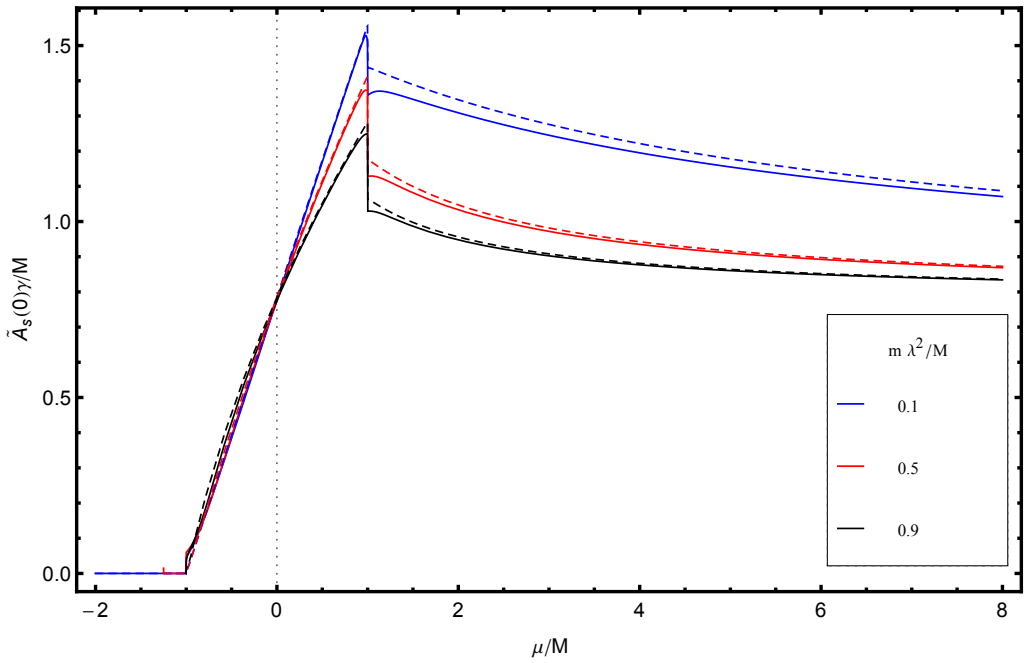

Figure 4.4: The longitudinal torque scales with the dimensionless parameter $\tilde{A}_s(0)\gamma/M$, plotted as a function of μ/M for various ratios of the SO coupling strength over M. Disorder strengths are given by $\gamma/M = 0.1$ for the solid lines and $\gamma/M = 0.01$ for the dashed ones.

$m\lambda^2/M < 1$, where the first-order Born approximation for the imaginary part of the self-energy is small.

The Fermi sea contributions to the currents and torques are present in the absence of disorder, as we discussed before, and are an intrinsic property of the system. From the last line of Eq. (4.52) we obtain

$$\partial_\epsilon C_c(\epsilon) = \frac{\hbar|e|^2}{2\pi\beta}\mathrm{Im}\sum_{\boldsymbol{k}}\left\{\lambda\frac{\hbar k^i}{m}\mathrm{tr}\left[\hat{\sigma}^j\frac{\partial\hat{\mathcal{G}}^{\mathrm{R}}_{\boldsymbol{k}}}{\partial\epsilon}\hat{\mathcal{G}}^{\mathrm{R}}_{\boldsymbol{k}}\right]\delta^{ij}_{\perp}\right\}; \tag{4.81}$$

$$\partial_\epsilon C_s(\epsilon) = -\frac{|e|Ma^2}{2\pi\beta}\mathrm{Im}\sum_{\boldsymbol{k}}\left\{\frac{\hbar k^i}{m}\mathrm{tr}\left[\hat{\sigma}^j\frac{\partial\hat{\mathcal{G}}^{\mathrm{R}}_{\boldsymbol{k}}}{\partial\epsilon}\hat{\mathcal{G}}^{\mathrm{R}}_{\boldsymbol{k}}\right]\delta^{ij}_{\perp} - \lambda\mathrm{tr}\left[\hat{\sigma}^i\frac{\partial\hat{\mathcal{G}}^{\mathrm{R}}_{\boldsymbol{k}}}{\partial\epsilon}\hat{\sigma}^j\hat{\mathcal{G}}^{\mathrm{R}}_{\boldsymbol{k}}\right]\epsilon^{ijz}\right\}. \tag{4.82}$$

The Fermi sea term for the current density is given by

$$\begin{aligned}\partial_\epsilon C(\epsilon) &= -\frac{|e|^2 m\lambda^2}{\pi^2\hbar\beta}\mathrm{Im}\left[\tilde{I}_{020}(\epsilon)\left(X'(\epsilon)Y(\epsilon) - X(\epsilon)Y'(\epsilon)\right) - \tilde{I}_{120}Y'(\epsilon)\right] \\ &= -\frac{|e|^2}{4\pi^2\hbar\beta}\frac{\partial}{\partial\epsilon}\mathrm{Im}\left[\log\frac{X+Y}{X-Y} + \frac{Y}{\Delta}\log\frac{\zeta_+}{\zeta_-}\right],\end{aligned} \tag{4.83}$$

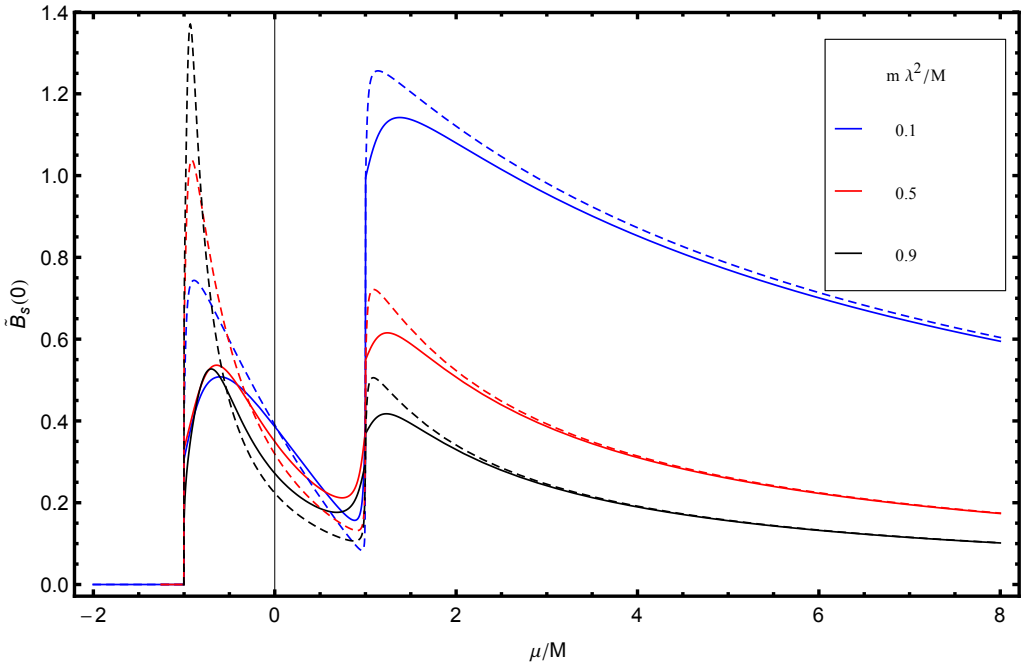

Figure 4.5: Dimensionless $\tilde{B}_s(0)$ as a function of μ/M for various strengths of the SO coupling. Disorder strengths are given by $\gamma/M = 0.1$ for the solid lines and $\gamma/M = 0.01$ for the dashed lines.

and for the spin Fermi sea term we have a very similar expression

$$\begin{aligned}\partial_\epsilon C_s(\epsilon) &= \frac{|e|mMa^2\lambda}{\pi^2\hbar^2\beta}\mathrm{Im}\left[\tilde{I}_{020}(\epsilon)\left(X'(\epsilon)Y(\epsilon)-X(\epsilon)Y'(\epsilon)\right)\right] \\ &= \frac{|e|mMa^2\lambda}{\pi^2\hbar^2\beta}\mathrm{Im}\left\{\frac{1}{4m\lambda^2}\frac{\partial}{\partial\epsilon}\left[\log\frac{X+Y}{X-Y}+\frac{Y}{\Delta}\log\frac{\zeta_-}{\zeta_+}\right]+\tilde{I}_{120}Y'(\epsilon)\right\} \quad (4.84)\end{aligned}$$

Note the extra contribution $\tilde{I}_{120}Y'(\epsilon)$ for the spin Fermi sea term with respect to the Fermi sea term for the current. This implies that in the absence of disorder both Fermi sea terms depend on the same function. We can work out the expression for the charge current Fermi sea contribution further such that, after a partial integration, we obtain

$$C_0 = -\frac{|e|^2}{4\pi^2\hbar\beta}\int_{-\infty}^{\infty}d\epsilon\left(-\frac{\partial f}{\partial\epsilon}\right)\mathrm{Im}\left[\log\frac{\epsilon+\mu-M-i\gamma_-}{\epsilon+\mu+M-i\gamma_+}-\frac{M-i\gamma_z}{\Delta}\log\frac{-\zeta_+}{-\zeta_-}\right], \quad (4.85)$$

where $\gamma_\pm = \gamma_0 \pm \gamma_z$. In Fig. 4.6 we show the results for the Fermi sea term at zero temperature. For the small disorder strengths we show here, the dimensionless part of the Fermi sea contribution to the spin torque $\tilde{C}_{s,0}$ is indistinguishable from the dimensionless contribution to the current density $\tilde{C}_0 = 4\pi^2\hbar C_0/|e|$ that is shown in the figure.

We can relate the above expression for the Fermi sea contribution to the results for the Dirac ferromagnet [119]. The Hamiltonian for the Rashba ferromagnet reduces to

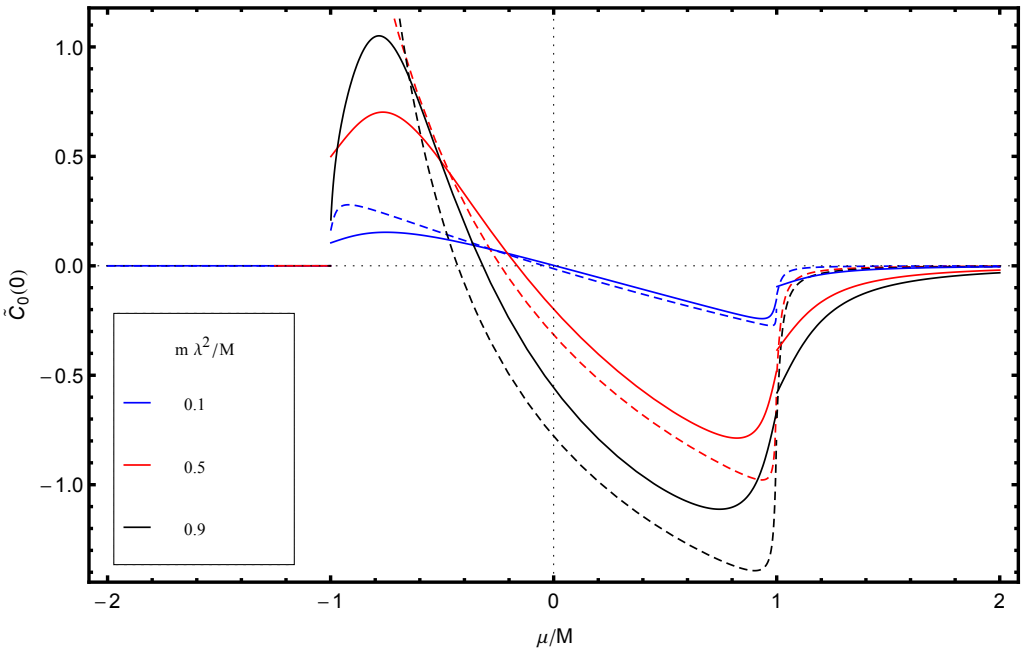

Figure 4.6: Results for the dimensionless Fermi-Sea term $\tilde{C}_0$. Solid lines correspond to $\gamma/M = 0.1$ and dashed lines correspond to $\gamma/M = 0.01$.

the Dirac ferromagnet when the kinetic energy vanishes, *i.e.* when the electrons become massless. In this limit, $m \to 0$ the second expression above is very similar to the result of Sakai and Kohno [119].

In this Section we presented the results for the charge and heat currents and spin torques for the homogeneous Rashba ferromagnet. Note that the relation between thermal en electric torques is given by Eq. (4.70). From the expressions in this Section it is clear that the thermal torques are not just described by a charge current induced thermally via the (spin-dependent) Seebeck effect. This has important consequences for the phenomenology we present in the next Section.

We can compare the results of this Chapter to the results of the previous one. The homogeneous torques calculated using the Boltzmann equation, given by Eqs. (3.29) and (3.30), agree with the results we obtained here using the Kubo formula when we take the direction of the magnetization along the z-axis.

4.6 Application

In the previous Section we derived expressions for the linear response coefficients for the Rashba ferromagnet in the presence of electric fields and temperature gradients. We studied the special situation where the magnetization is restricted to the z-direction for

weak disorder scattering. For this special case we obtained expressions for the torques induced electrically or thermally, and showed that these are related like the response coefficients of thermoelectric systems. In this Section we broaden our scope. In the following the magnetization is dynamic and is not restricted to the z-direction. We consider the effect of a temperature difference $\partial_x T$ and voltage bias E_x along the x-direction and only consider the longitudinal response for the (heat) current density. Thus we neglect any off-diagonal contributions to the conductivity, such as the B_c and C_c contributions of the previous Section. We neglect these terms here to focus on the additional dissipative contributions due to the spin torques.

The spin torques $\boldsymbol{\tau}_{\mathrm{ST}}$ are caused by a voltage or temperature gradient along the wire. In this Section we use the phenomenological parameters β, $\beta^{\perp}$ to denote these electrical induced torques. In addition we introduce the parameters β_T and $\beta_T^{\perp}$ that describe the spin torques arising from a temperature gradient. Note that we calculated these parameters in the previous Section within the *s-d* model using linear response theory. However, in this Section we are interested in additional dissipation induced by (thermal) SO torques independent of a specific model. Therefore we consider these parameters to be determined by experiment and consider the result they have on the dissipation power. The spin torques in terms of these phenomenological parameters read

$$\begin{aligned}\boldsymbol{\tau}_{\mathrm{ST}} &= +E_x\beta\boldsymbol{m}\times\boldsymbol{e}_y + E_x\beta^{\perp}\boldsymbol{m}\times(\boldsymbol{m}\times\boldsymbol{e}_y)\\ &\quad +\partial_x T\beta_T\boldsymbol{m}\times\boldsymbol{e}_y + \partial_x T\beta_T^{\perp}\boldsymbol{m}\times(\boldsymbol{m}\times\boldsymbol{e}_y).\end{aligned} \tag{4.86}$$

We can relate the phenomenological parameters that we introduced above to the calculation of the previous Section. When the magnetization points in the z-direction we see that β and β_T are related to the part of the torque proportional to $A_{s,0}$ and $A_{s,1}$, respectively. The coefficients corresponding to the perpendicular torques are obtained from $B_s - C_s$. We already remarked that our expressions agree with the theory in the previous Chapter. When we interpret the torque proportional to β as coming from a current induced Rashba magnetic field $\boldsymbol{H}_{\mathrm{R}}$ then using the parameters of Table 3.2 we obtain $H_R \sim 10^{-14}\,\mathrm{Tm^2A^{-1}}$ as an estimate. From Figs. 4.4 and 4.5 we can conclude that the perpendicular component is a about a factor ten smaller. The thermal torques follow from Eq. (4.70).

We rewrite the LLG equation given in Eq. (5.14) into the equivalent Landau-Lifshitz form that allows for a description using the linear response matrix, hence we have

$$\begin{aligned}\dot{\boldsymbol{m}} &= -\tilde{\gamma}\boldsymbol{m}\times\mu_0\boldsymbol{H}_{\mathrm{eff}} + \alpha_G\tilde{\gamma}\boldsymbol{m}\times\mu_0\boldsymbol{H}_{\mathrm{eff}}\times\boldsymbol{m}\\ &\quad +(\tilde{\beta}E_x + \tilde{\beta}_T\partial_x T)\boldsymbol{m}\times\boldsymbol{e}_y\\ &\quad +(\tilde{\beta}^{\perp}E_x + \tilde{\beta}_T^{\perp}\partial_x T)\boldsymbol{m}\times\boldsymbol{e}_y\times\boldsymbol{m},\end{aligned} \tag{4.87}$$

the scaled parameters read

$$\begin{aligned}\tilde{\gamma} &= \frac{\gamma}{1+\alpha_G^2};\\ \tilde{\beta}_{(T)} &= \frac{1}{1+\alpha_G^2}\left(\beta_{(T)} - \alpha_G\beta^{\perp}_{(T)}\right);\\ \tilde{\beta}^{\perp}_{(T)} &= \frac{1}{1+\alpha_G^2}\left(\beta^{\perp}_{(T)} + \alpha_G\beta_{(T)}\right).\end{aligned}$$

The dissipative torques in Eq. 4.87 are characterized by their change of sign under time reversal. We see that in addition to dissipation from the Gilbert damping term we have the additional dissipative contributions that are parameterized by $\tilde{\beta}^{\perp}$ and $\tilde{\beta}^{\perp}_T$.

The induced torques have Onsager reciprocals[45] as we discussed in the Introduction. Onsager symmetry for the linear response matrix $\Gamma(\boldsymbol{m})$ implies $\Gamma_{ij}(\boldsymbol{m}) = e_i e_j \Gamma_{ji}(-\boldsymbol{m})$, (note that we do not imply the Einstein convention here) where $e_i = +(-)1$ when component i is even (odd) under time-reversal. Using the symmetry relations we introduced above we obtain the linear response matrix for the Rashba ferromagnet,

$$\begin{pmatrix} j_c^x \\ j_Q^x \\ \dot{\boldsymbol{M}} \end{pmatrix} = \Gamma(\boldsymbol{m}) \cdot \begin{pmatrix} E_x \\ \partial_x T/T \\ \mu_0 \boldsymbol{H}_{\rm eff}, \end{pmatrix}, \tag{4.88}$$

where

$$\Gamma(\boldsymbol{m}) = \begin{pmatrix} \sigma & \sigma S T & M_s(-\tilde{\beta} + \tilde{\beta}^{\perp}\boldsymbol{m}\times)(\boldsymbol{m}\times\boldsymbol{e}_y) \\ \sigma S T & \kappa' T & T M_s(-\tilde{\beta}_T + \tilde{\beta}^{\perp}_T \boldsymbol{m}\times)(\boldsymbol{m}\times\boldsymbol{e}_y) \\ M_s(\tilde{\beta} + \tilde{\beta}^{\perp}\boldsymbol{m}\times)(\boldsymbol{m}\times\boldsymbol{e}_y) & T M_s(\tilde{\beta}_T + \tilde{\beta}^{\perp}_T \boldsymbol{m}\times)(\boldsymbol{m}\times\boldsymbol{e}_y) & \Gamma_m(\boldsymbol{m}) \end{pmatrix},$$

where σ is the conductivity, S is the Seebeck coefficient and $\kappa' = \kappa(1+ZT)$ is the heat conductivity, where $ZT = \sigma S^2 T/\kappa$ is the dimensionless thermoelectric figure of merit and $\Gamma_m(\boldsymbol{m})$ is the response of the magnetization to the magnetic field. The matrix entry $\Gamma_m(\boldsymbol{m})$ leads to the Landau-Lifshitz equation without the spin torques.

In the following we ignore anisotropies of the ferromagnet and for simplicity take the effective field equal to the applied field, *i.e.*, $\boldsymbol{H}_{\rm eff} = \boldsymbol{H}$. The dissipation power per unit volume in the system is given by the inner product of the forces and fluxes

$$P = j_c^x E_x + j_Q^x \frac{\partial_x T}{T} + M_s \mu_0 \dot{\boldsymbol{m}} \cdot \boldsymbol{H},$$

which, using the linear response matrix, yields

$$P = P_{\rm TE} + \alpha_G \tilde{\gamma} (\mu_0 M_s)^2 (\boldsymbol{m}\times\boldsymbol{H})^2 - 2\mu_0 M_s \left(\tilde{\beta}^{\perp} E_x + \tilde{\beta}^{\perp}_T \partial_x T\right)(\boldsymbol{m}\times\boldsymbol{H})\cdot(\boldsymbol{m}\times\boldsymbol{e}_y), \tag{4.89}$$

where M_s is the saturation magnetization of the ferromagnet and

$$P_{\rm TE} = \sigma E_x^2 + \kappa' \partial_x T^2/T + 2\sigma S E_x(\partial_x T),$$

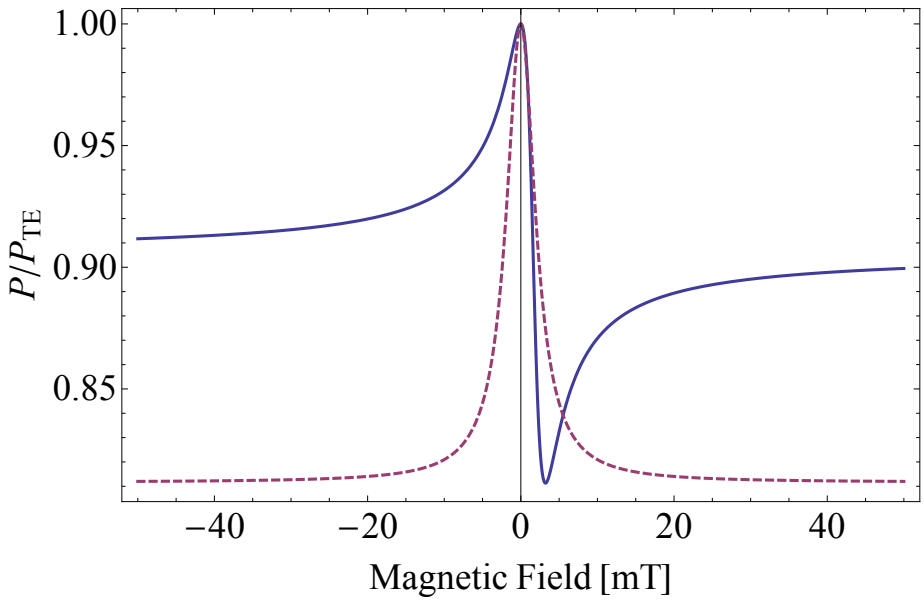

Figure 4.7: The dissipation power depends on the angle θ_H of the magnetic field with the x-axis. The solid blue line is the result for $\theta_H = \pi/4$ and the dashed purple line is $\theta_H = 0$. For $\theta_H = \pi/2$ the power is given by the thermoelectric power P_{TE}. Here we assumed a current density $j_{c,x} = 10^{10}\mathrm{A/m}^2$, $\nabla T = 0$ and $\beta^{\perp}/\beta = 0.1$.

is the thermoelectric dissipation power which consists of the Joule and Thomson heating. By the second law of thermodynamics the total dissipation should be positive for all temperature and voltage differences. This has consequences for the parameters that the describe the torques due to SO coupling and leads to the following inequality for the phenomenological parameters

$$\sigma\frac{\tilde{\gamma}\alpha_G}{M_s} > \tilde{\beta}^{\perp 2} + \frac{\sigma}{\kappa T}\left(ST\tilde{\beta}^{\perp} - T\tilde{\beta}_T^{\perp}\right)^2. \tag{4.90}$$

4.6.1 Static magnetization

Once a bias, whether it is a voltage or temperature bias, is applied over the Rashba ferromagnet the presence of the additional spin torques implies that the steady state magnetization direction not necessarily orients itself in the external magnetic field applied in the plane. The steady state direction of the magnetization, $\boldsymbol{m}_0$, is such that

$$\begin{pmatrix} j^0 \\ j_Q^0 \\ \mathbf{0} \end{pmatrix} = \Gamma\left(\boldsymbol{m}_0\right) \cdot \begin{pmatrix} E_x \\ \partial_x T/T \\ \mu_0 \boldsymbol{H} \end{pmatrix}. \tag{4.91}$$

Up to first order in the voltage and temperature difference we obtain for the steady state magnetization

$$\boldsymbol{m}_0 \propto \gamma\mu_0\boldsymbol{H} - (\beta E_x + \beta_T \partial_x T)\boldsymbol{e}_y - \cos(\theta_H)(\beta^\perp E_x + \beta_T^\perp \partial_x T)\boldsymbol{e}_z, \tag{4.92}$$

where θ_H is the angle the magnetic field makes with the x-axis. Two special cases can be distinguished, where the above first-order solution becomes exact. The first being when the magnetic field points in the $\boldsymbol{e}_y$ direction ($\theta_H = \pi/2$) which gives $\boldsymbol{m}_0 = \boldsymbol{e}_y$. In this case the dissipative spin torques and Gilbert damping align, which allows for an exact solution linear in temperature and voltage gradients. The approximation to linear order is also exact when the dissipative torques induced by SO coupling vanish, *i.e.*, $\beta^\perp_{(T)} = 0$.

When we insert the expression for the equilibrium magnetization, Eq. (4.92), into the equation for dissipation power (Eq. (4.89)) we obtain the dissipation from the misalignment of the equilibrium magnetization and the applied magnetic field when the applied field is not in the $\boldsymbol{e}_y$ direction. In Fig. 4.7 we show the ratio of the total dissipation power to P_{TE} the power dissipated by thermoelectric effects only. The dependence of the dissipation power on the magnetization direction, which is influenced strongly by the external magnetic field, shows that the spin torques also are related to anisotropic magnetoresistance.

4.6.2 Ferromagnetic resonance

In this Section we extend the steady-state situation described in the last Section by applying an additional small radio frequency (rf) magnetic field in the z-direction. The frequency of this field is ω, such that $\boldsymbol{H}_{\rm rf} = H_{\rm rf}\cos(\omega t)\boldsymbol{e}_z$. We linearize the equation of motion for small angle precession around the steady-state direction $\boldsymbol{m}_0$. The magnetization is written as

$$\boldsymbol{m} = \boldsymbol{m}_0 + \delta_1(t)\boldsymbol{e}_1 + \delta_2(t)\boldsymbol{e}_2, \tag{4.93}$$

where $\boldsymbol{m}_0$, $\boldsymbol{e}_1$, $\boldsymbol{e}_2$ are such that we have an orthonormal basis. In this basis we have the differential equations

$$\dot{\delta}_1(t) = \omega_{rf}\cos(\omega t) + \Omega\delta_2(t) - \Omega_D\delta_1(t); \tag{4.94}$$

$$\dot{\delta}_2(t) = \alpha_G\omega_{rf}\cos(\omega t) - \Omega\delta_1(t) - \Omega_D\delta_2(t), \tag{4.95}$$

where we defined the frequencies

$$\omega_{rf} = \tilde{\gamma}\mu_0 H_{rf}; \tag{4.96}$$

$$\Omega = \left(-\tilde{\gamma}\mu_0\boldsymbol{H} + (\tilde{\beta}E_x + \tilde{\beta}_T\partial_x T)\boldsymbol{e}_y\right)\cdot\boldsymbol{m}_0; \tag{4.97}$$

$$\Omega_D = \left(-\alpha_G\tilde{\gamma}\mu_0\boldsymbol{H} + (\tilde{\beta}^\perp E_x + \tilde{\beta}_T^\perp\partial_x T)\boldsymbol{e}_y\right)\cdot\boldsymbol{m}_0. \tag{4.98}$$

Note that when $\beta^\perp_{(T)} = 0$ we obtain $\Omega_D = \alpha_G\Omega$. The amount of heat produced follows from Eq. (4.89). Here we focus on the parts involving the magnetization only and are interested in dissipation averaged over a period of the frequency of the rf field.

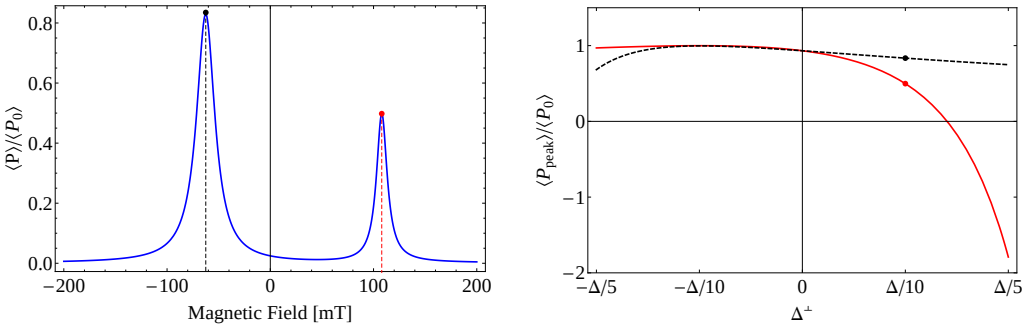

(a) (b)

Figure 4.8: (a) The power signal with respect to the peak power without SO coupling as a function of magnetic field. Here we took $\omega = 15\,\mathrm{GHz}$, $\beta = 2.0 \times 10^6\,\mathrm{m/Vs}$, $\beta^\perp = 0.1\beta$ and $E_x = 2.0 \times 10^3\,\mathrm{V/m}$ and no temperature gradient. (b) The dependence of the power at resonance on $\Delta^\perp$.

The resonant parts involve the unit-vectors $\boldsymbol{e}_1$ and $\boldsymbol{e}_2$. Those unit-vectors form a orthonormal basis with $\boldsymbol{m}_0$, keeping only terms up to first order in E_x and $\partial_x T$ we obtain for the dissipation power.

$$\begin{aligned}\frac{\langle P_\mathrm{r}\rangle}{\omega_\mathrm{rf}^2} &= -H\left(2\Omega_D + \alpha_G\tilde{\gamma}\mu_0 H\right)\frac{(1+\alpha_G^2)(\omega^2+\Omega^2+\Omega_D^2)}{2((\omega-\Omega)^2+\Omega_D^2)((\omega+\Omega)^2+\Omega_D^2)} \\ &\quad + \frac{\alpha_G}{2\tilde{\gamma}} + \frac{2}{\tilde{\gamma}}\Omega_D\frac{\omega^2(\Omega+\alpha_G\Omega_D)-(\Omega^2+\Omega_D^2)(\Omega-\alpha_G\Omega_D)}{2((\omega-\Omega)^2+\Omega_D^2)((\omega+\Omega)^2+\Omega_D^2)}. \end{aligned} \tag{4.99}$$

The resonance frequencies are given by

$$\omega_\pm = \omega \pm (\beta E_x + \beta_T \partial_x T)\sin\theta_H.$$

In Fig. 4.8a the dissipation power as a function of the applied field is shown, the resonances can be easily found. Thus, by a series of measurements, with different voltage or temperature differences over the Rashba ferromagnet, the parameters $\beta_{(T)}$ that describe the reactive SO coupling induced torques can be measured. Substitution of the resonant frequencies into the equation for the dissipation power as given in Eq. (4.99) yields the power dissipated at resonant frequencies, which shown in Fig. 4.8b. In the absence of SO coupling the power dissipated at the resonances is equal. But, as can be seen from Fig. 4.8b, the relative height of the maximum dissipation power depends on the dissipative spin torques parameterized by $\Delta^\perp$, where we used the notation $\Delta^{(\perp)} = (\beta^{(\perp)}E_x + \beta_T^{(\perp)}\partial_x T)\sin\theta_H$.

4.7 Discussion

In this Chapter we calculated thermal spin torques for the Rashba ferromagnet using the *s-d* model. In order to arrive at the results in Sec. 6.6, we needed to make a subtraction

to remove an unphysical divergency at zero temperature. We showed that the divergent term could be accounted for by properly subtracting the local equilibrium spin density in the presence of the gravitational potential. Subsequently we described the Rashba ferromagnet phenomenologically and showed that the (thermal) spin torque parameters can in principle be determined using a FMR experiment.

4.A Traces

Below we list the results for the traces involving two Green's functions. The tilde is used to distinct the two Green's functions which may depend on different coordinates or be on a different branch of the continuation.

$$\begin{aligned}
\mathrm{tr}\left[\mathcal{G}\tilde{\mathcal{G}}\right] &= 2D\tilde{D}\left(g_0\tilde{g}_0 + \boldsymbol{g}\cdot\tilde{\boldsymbol{g}}\right); && (4.100)\\
\mathrm{tr}\left[\sigma^i\mathcal{G}\tilde{\mathcal{G}}\right] &= 2D\tilde{D}\left(g_0\tilde{g}^i + \tilde{g}_0 g^i - i\epsilon^{ijk}g^j\tilde{g}^k\right); && (4.101)\\
\mathrm{tr}\left[\sigma^i\mathcal{G}\sigma^j\tilde{\mathcal{G}}\right] &= 2D\tilde{D}\Big(\delta^{ij}(g_0\tilde{g}_0 - \boldsymbol{g}\cdot\tilde{\boldsymbol{g}}) + g^i\tilde{g}^j + \tilde{g}^i g^j\\
&- i\epsilon^{ijk}(g_0\tilde{g}^k - \tilde{g}_0 g^k)\Big). && (4.102)
\end{aligned}$$

4.B Integrals

The nonvanishing integrals we encounter are of the form

$$I_{lmn} \equiv \sum_{\boldsymbol{k}} \left(\frac{\hbar^2\boldsymbol{k}^2}{2m}\right)^l \left(D^R_{\boldsymbol{k}}\right)^m \left(D^A_{\boldsymbol{k}}\right)^n, \tag{4.103}$$

where $D^R_{\boldsymbol{k}}$ is the retarded denominator of the Green's function. This means

$$I_{lmn} = \frac{m}{2\pi\hbar^2}\tilde{I}_{lmn}, \tag{4.104}$$

where

$$\tilde{I}_{lmn} = \int_0^\infty dx \frac{x^l}{\left[(x-\zeta_+)(x-\zeta_-)\right]^m\left[(x-\zeta_+^*)(x-\zeta_-^*)\right]^n}, \tag{4.105}$$

where the star means complex conjugation and

$$\zeta_\pm = \epsilon + \mu + m\lambda^2 + i\gamma_0 \pm \Delta, \tag{4.106}$$

where

$$\Delta = \sqrt{(M+i\gamma_z)^2 + (m\lambda^2)^2 + 2m\lambda^2(\epsilon+\mu+i\gamma_0)}. \tag{4.107}$$

Note that for the calculation of the self-energy in the first born approximation we should put γ_0, $\gamma_z = 0$, and use $\epsilon \to \epsilon \pm i\eta$ for the retarded and advanced branches. Below we

list some properties

$$\tilde{I}_{lmn} = \tilde{I}^*_{lnm}; \tag{4.108}$$

$$\tilde{I}_{l,m,n} = (\zeta_+ + \zeta_-)\tilde{I}_{l-1,m,n} + \tilde{I}_{l-2,m-1,n} - \zeta_+\zeta_-\tilde{I}_{l-2,m,n} \quad , \quad (l \geq 2); \tag{4.109}$$

$$\begin{aligned}\tilde{I}_{l,1,0} &= \tilde{I}_{l+2,1,1} - \tilde{I}_{l+1,1,1}\mathrm{Re}[\zeta_+ + \zeta_-] + \tilde{I}_{l,1,1}\mathrm{Re}[\zeta_+\zeta_-] \\ &+ i\left(\tilde{I}_{l+1,1,1}\mathrm{Im}[\zeta_+ + \zeta_-] - \tilde{I}_{l,1,1}\mathrm{Im}[\zeta_+\zeta_-]\right),\end{aligned} \tag{4.110}$$

and some results

$$\begin{aligned}
\tilde{I}_{010} &= \frac{\log(-\zeta_-) - \log(-\zeta_+)}{2\Delta}; \\
\tilde{I}_{020} &= -\frac{\zeta_- + \zeta_+}{\Delta^2\zeta_+\zeta_-} - \frac{\log(-\zeta_-) - \log(-\zeta_+)}{4\Delta^3}; \\
\tilde{I}_{120} &= \frac{1}{2\Delta^2} - (\zeta_+ + \zeta_-)\frac{\log(-\zeta_-) - \log(-\zeta_+)}{8\Delta^3}; \\
\tilde{I}_{011} &= \frac{1}{\zeta_- - \zeta_+}\left(\frac{\log(-\zeta_+)}{(\zeta_+ - \zeta_+^*)(\zeta_+ - \zeta_-^*)} - \frac{\log(-\zeta_-)}{(\zeta_- - \zeta_+^*)(\zeta_- - \zeta_-^*)}\right) + c.c.; \\
\tilde{I}_{111} &= \frac{1}{\zeta_- - \zeta_+}\left(\frac{\zeta_+\log(-\zeta_+)}{(\zeta_+ - \zeta_+^*)(\zeta_+ - \zeta_-^*)} - \frac{\zeta_-\log(-\zeta_-)}{(\zeta_- - \zeta_+^*)(\zeta_- - \zeta_-^*)}\right) + c.c.; \\
\tilde{I}_{211} &= \frac{1}{\zeta_- - \zeta_+}\left(\frac{\zeta_+^2\log(-\zeta_+)}{(\zeta_+ - \zeta_+^*)(\zeta_+ - \zeta_-^*)} - \frac{\zeta_-^2\log(-\zeta_-)}{(\zeta_- - \zeta_+^*)(\zeta_- - \zeta_-^*)}\right) + c.c.
\end{aligned}$$

The integral I_{110} does not converge but we only need its imaginary part to calculate the self-energy. We can obtain the imaginary part from Eq. (4.110).

Chapter 5

Magnetic-texture-controlled transverse spin injection

Abstract

We propose an effect whereby an electric current along the interface between a ferromagnetic and normal metal leads to injection of pure spin current into the normal metal, if the magnetization-direction in the ferromagnet varies spatially along the direction of current. For the specific example of a ferromagnetic spin spiral, we compute the inverse spin-Hall effect voltage this spin current gives rise to when injected into a Pt layer. Furthermore, we show that this pure spin current leads to modification of the parameters that govern spin transfer and current-driven domain-wall motion, which can be used to tune the latter in layered magnetic systems. This effect in principle enables in-situ control over the location, magnitude and polarization of spin-current injection in devices.

5.1 Introduction

Spintronic devices make use of the spin degree of freedom to process and store information. Hence, the generation and detection of non-equilibrium spin accumulation and spin currents is of paramount importance. In particular, all-electric injection and control of spin currents at room temperature and without high magnetic fields is crucial for viable integration with and as extension of current technology. [120] To obtain spin currents, a large variety of physical mechanisms and geometries are investigated.[4, 5, 121] One class of approaches relies on parametric pumping.[122] In these, a periodic (AC) excitation is transformed into a DC spin current. Examples are circularly polarized optical photons,[5, 123–125] magnons [126–128] acoustic waves [129] and single-domain ferromagnetic resonance.[21, 130, 131] For example, recently the injection of pure spin current using this last method was demonstrated for p-Type Si. [132]

In contrast to the pumping approaches described above, a spin accumulation can also be obtained via a static bias. A current through a ferromagnet-nonmagnetic-metal (FM-NM) junction causes spin injection into the nonmagnetic layer.[133–136] Room-temperature injection in silicon was demonstrated in Ref. [137]. Spin-orbit coupling also

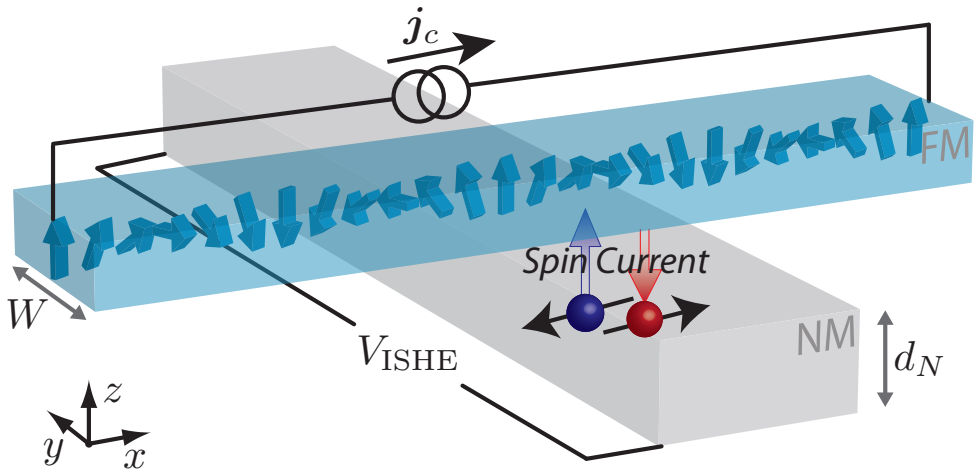

Figure 5.1: (Color online) A charge current along the interface between a ferromagnet containing a magnetic texture and a normal metal leads to the injection of a transverse pure spin current at the interface. The direction of the spin component of the injected spin current is in the direction of the helicity $\boldsymbol{m} \times (\boldsymbol{j}_c \cdot \nabla)\boldsymbol{m}$ of the spin spiral along the current direction, leading to a spin accumulation in the normal metal.

opens the possibility to create spin currents using electric fields only. For example, the spin Hall effect generates a spin current transverse to a charge current. [63, 138–142]

The interplay between heat flow and spin currents studied in the young field of spin caloritronics, yields novel ways to inject pure spin currents using temperature gradients. For example, heat flow leads to the generation of spin accumulation via the spin Seebeck effect, [113] spin-dependent Seebeck effect [143] and spin Seebeck tunneling.[144] Controlling spin currents with charge flow is the prime occupation of spintronics. Research on spin currents, however, has impact beyond this field, and has led, for example, to the discovery of time-reversal-invariant topological insulators.[145, 146]

In this Chapter we propose a mechanism for the injection of a spin current into the normal metal in a FM-NM heterostructure that is perpendicular to the FM-NM interface and transverse to the electric current that flows along the interface (see Fig. 5.1). Consider a *static* magnetic texture in the FM layer such that the direction of magnetization $\boldsymbol{m}(\boldsymbol{x})$ depends on the coordinate along the wire, and such that electric current flows along the wire. We denote the charge current density on the interface by $\boldsymbol{j}_c$. It is the magnitude of this charge current density that governs the magnitude of the injected spin current. As we discuss in detail below, the change in orientation of the magnetization due to the presence of a magnetization gradient will cause a transverse spin current $\boldsymbol{j}_s^{\mathrm{in}}$ into the NM given by

$$\boldsymbol{j}_s^{\mathrm{in}}(\boldsymbol{x}) = \frac{\hbar g}{4\pi G_0} \boldsymbol{m}(\boldsymbol{x}) \times \left[(\boldsymbol{v}_s \cdot \boldsymbol{\nabla}) \boldsymbol{m}(\boldsymbol{x}) \right], \tag{5.1}$$

where $\boldsymbol{j}_s^{\rm in}(\boldsymbol{x})$ is the injected spin-current density flowing perpendicular to the interface (and hence transverse to the charge current direction) with spin polarization in the direction of the helicity $\boldsymbol{m}\times(\boldsymbol{j}_c\cdot\nabla)\boldsymbol{m}$ of the magnetization texture along the current direction (in the x-direction for the situation in Fig. 5.1). Here, $\boldsymbol{m}(\boldsymbol{x})$ is the unit-vector magnetization direction of the FM-layer, $\boldsymbol{v}_s = -g_L\mu_B P\boldsymbol{j}_c/2M_s|e|$ is the spin velocity, P is the spin polarization of the current density at the interface, g_L the Landé g-factor, μ_B is the Bohr magneton, M_s is the saturation magnetization, and $-|e|$ the charge of an electron. Moreover, $G_0 = 2e^2/h$ is the quantum of conductance. Furthermore, the parameter g is governed by the spin-dependent transport properties of the FM-NM interface. Eq. (5.1) is the main equation describing the effect we propose in this Chapter.

In the next Section we give a scattering-theory expression for the interface parameter g, that can be evaluated using ab initio methods. The scattering theory is valid for treating the interface which is atomically sharp, and yields boundary conditions for the diffusive description appropriate for the bulk.

5.2 Scattering theory

We consider a two-dimensional tight-binding model for the interface between ferromagnet and normal metal. The ferromagnetism is described with localized magnetic moments exchange coupled to the electrons, and connected on every site $\mathbf{r} = \{i_x, i_y\}$ to a metallic reservoir (*i.e.*, the normal metal) with chemical potentials $\mu_{\mathbf{r}}$. The system is described by the Hamiltonian $\mathcal{H} = \mathcal{H}_S + \mathcal{H}_L + \mathcal{H}_C$ representing electronic system in the FM, NM-leads and contacts between them, respectively. The first term is specified in terms of second-quantized operators $\hat{c}_{\mathbf{r},\sigma}(\hat{c}^\dagger_{\mathbf{r},\sigma})$ that annihilate (create) an electron with spin σ at site $\mathbf{r}$

$$\mathcal{H}_S = -J_S\sum_{\langle\mathbf{r},\mathbf{r}'\rangle;\sigma}\hat{c}^\dagger_{\mathbf{r},\sigma}\hat{c}_{\mathbf{r}',\sigma} - \Delta\sum_{\mathbf{r};\sigma,\sigma'}\hat{c}^\dagger_{\mathbf{r},\sigma}\boldsymbol{m}_{\mathbf{r}}\cdot\boldsymbol{\tau}_{\sigma,\sigma'}\hat{c}_{\mathbf{r},\sigma'}, \tag{5.2}$$

which describes nearest-neighbor (indicated by the brackets $\langle\cdot,\cdot\rangle$) hopping with amplitude J_S and coupling to the local magnetic moments $\boldsymbol{m}_{\mathbf{r}}$, where Δ is the exchange energy and $\boldsymbol{\tau}$ is the Pauli spin-matrix vector. The metallic contact is described by a set of one-dimensional leads at chemical potential $\mu_{\mathbf{r}}$ and modeled by the Hamiltonian $\mathcal{H}_L = \sum_{\mathbf{r}}\mathcal{H}_{\mathbf{r}}$ where the Hamiltonian for the lead connected to site $\mathbf{r}$ is given by $\mathcal{H}_{\mathbf{r}} = -J_{L_{\mathbf{r}}}\sum_{\langle j',j''\rangle;\sigma}\left[\hat{d}^{L_{\mathbf{r}}}_{j',\sigma}\right]^\dagger\hat{d}^{L_{\mathbf{r}}}_{j'',\sigma}$, where the hopping amplitude is $J_{L_{\mathbf{r}}}$ and $\hat{d}^{L_{\mathbf{r}}}_{j,\sigma}$ and $\left[\hat{d}^{L_{\mathbf{r}}}_{j,\sigma}\right]^\dagger$ are the fermionic operators in the $\mathbf{r}^{\rm th}$ lead. Finally the contact between the ferromagnetic system and its leads is described by $\mathcal{H}_C = \sum_{\mathbf{r}}\mathcal{H}^{\mathbf{r}}_C$ with

$$\mathcal{H}^{\mathbf{r}}_C = -J^{\mathbf{r}}_C\sum_\sigma\left[\hat{c}^\dagger_{\mathbf{r},\sigma}\hat{d}^{L_{\mathbf{r}}}_{\partial L_{\mathbf{r}},\sigma} + \left[\hat{d}^{L_{\mathbf{r}}}_{\partial L_{\mathbf{r}},\sigma}\right]^\dagger\hat{c}_{\mathbf{r},\sigma}\right], \tag{5.3}$$

where $\partial L_{\mathbf{r}}$ denotes the last site of the lead and $J^{\mathbf{r}}_C$ is the amplitude of tunneling among both subsystems. An electric current flows through the FM by a difference in chemical potentials μ_L and μ_R that connect the left and right sides of the FM.

The spin current flowing from the system to the leads is determined as the rate of change of spin density in the $\mathbf{r}$-th site, *i.e.* $\frac{d\mathbf{s}^{\mathbf{r}}}{dt} = \frac{\hbar}{2a^2}\frac{d}{dt}\sum_{\sigma,\sigma'}\langle \hat{c}^{\dagger}_{\mathbf{r},\sigma}\boldsymbol{\tau}_{\sigma,\sigma'}\hat{c}_{\mathbf{r},\sigma'}\rangle$, where a is the distance between sites. The general expression has been derived before [147] and is given by

$$\frac{d\mathbf{s}^{\mathbf{r}}}{dt} = \frac{i\hbar}{2a^2}\int\frac{d\epsilon}{2\pi}\mathrm{Tr}\Bigg[N\left(\epsilon-\mu^{\mathbf{r}}\right)\Gamma^{\mathbf{r}}_{\mathbf{r},\mathbf{r}}(\epsilon)\left(\boldsymbol{\tau}G^{R}_{\mathbf{r},\mathbf{r}}(\epsilon)-G^{A}_{\mathbf{r},\mathbf{r}}(\epsilon)\boldsymbol{\tau}\right) - \sum_{\mathbf{r}'}N\left(\epsilon-\mu^{\mathbf{r}'}\right)\left(\boldsymbol{\tau}\Sigma^{\mathbf{r},R}_{\mathbf{r},\mathbf{r}}(\epsilon)-\Sigma^{\mathbf{r},A}_{\mathbf{r},\mathbf{r}}(\epsilon)\boldsymbol{\tau}\right)A^{\mathbf{r}'}_{\mathbf{r},\mathbf{r}}(\epsilon)\Bigg], \tag{5.4}$$

where $N(\epsilon) = \left[e^{\epsilon/k_BT}+1\right]^{-1}$ is the Fermi-Dirac distribution function with k_BT the thermal energy, $A^{\mathbf{r}}(\epsilon) = G^{R}(\epsilon)\hbar\Gamma^{\mathbf{r}}(\epsilon)G^{A}(\epsilon)$ is the spectral-weight contribution due to the lead at site $\mathbf{r}$ and the rate $\Gamma^{\mathbf{r}}(\epsilon) = i\left[\Sigma^{\mathbf{r},R}(\epsilon)-\Sigma^{\mathbf{r},A}(\epsilon)\right]$, where the superscript R (A) means the retarded (advanced) function (See Ref. [147] for details). Since we are assuming non-magnetic leads, the self-energy $\Sigma^{\mathbf{r},R}(\epsilon)$ will be proportional to the identity in spin space. Its only nonzero matrix elements are $\hbar\Sigma^{\mathbf{r},R}_{\mathbf{r},\sigma;\mathbf{r},\sigma'} = -(J^{\mathbf{r}}_{C})^2e^{ik^{\mathbf{r}}(\epsilon)a}\delta_{\sigma,\sigma'}/J_{L_{\mathbf{r}}}$, with $k^{\mathbf{r}}(\epsilon)a = \arccos\left[-\epsilon/2J_{L_{\mathbf{r}}}\right]$. To carry out the explicit evaluation of Eq. (5.4) in terms of the magnetization orientation $\boldsymbol{m}_{\mathbf{r}}$ it is convenient to decompose the Green's functions into spin-independent *singlet* and spin-dependent *triplet* parts, namely

$$G^{R}_{\mathbf{r},\sigma;\mathbf{r}',\sigma'}(\epsilon) = G^{(s)R}_{\mathbf{r},\mathbf{r}'}(\epsilon)\delta_{\sigma,\sigma'} + G^{(t)R}_{\mathbf{r},\mathbf{r}'}(\epsilon)\boldsymbol{m}_{\mathbf{r}}\cdot\boldsymbol{\tau}_{\sigma,\sigma'}, \tag{5.5}$$

and likewise for the advanced Green's function. Taking the trace over the spin indices in Eq. (5.4) we distinguish two contributions to the spin current, one component parallel to the magnetization vector and other transverse, denoted by $\boldsymbol{j}^{\parallel}_{s}(\mathbf{r})$ and $\boldsymbol{j}^{\mathrm{in}}_{s}(\mathbf{r})$ respectively. The transverse spin current density induced by the magnetic texture to lead $\mathbf{r}$ is given by

$$\boldsymbol{j}^{\mathrm{in}}_{s}(\mathbf{r}) = \frac{1}{a^2}\int\frac{d\epsilon}{(2\pi)}\sum_{\mathbf{r}'}N\left(\epsilon-\mu^{\mathbf{r}'}\right)\mathrm{t}^{(t)}_{\mathbf{r}\mathbf{r}'}(\epsilon)\left(\boldsymbol{m}_{\mathbf{r}}\times\boldsymbol{m}_{\mathbf{r}'}\right), \tag{5.6}$$

with the transmission probability $\mathrm{t}^{(t)}_{\mathbf{r}\mathbf{r}'}(\epsilon) = \hbar\Gamma^{\mathbf{r}}_{\mathbf{r},\mathbf{r}}(\epsilon)G^{(t)R}_{\mathbf{r},\mathbf{r}'}(\epsilon)\hbar\Gamma^{\mathbf{r}'}_{\mathbf{r}',\mathbf{r}'}(\epsilon)G^{(t)A}_{\mathbf{r}',\mathbf{r}}(\epsilon)$ for the spin-polarized part of the current flowing from the lead at site $\mathbf{r}$ to the lead at site $\mathbf{r}'$ through the FM. We now consider a zero net current (but nonzero spin current) flow into the leads, except for the left and right leads that have chemical potentials $\mu_L = \epsilon_F + |e|V$ and $\mu_R = \epsilon_F$, respectively, with ϵ_F the Fermi energy. At low temperatures and assuming the length scale of magnetization-orientation variation much greater than the inverse Fermi wavelength we see that in the continuum limit the only contributions to Eq. (5.6) are from neighboring leads for which $\boldsymbol{m}_{\mathbf{r}}\times\boldsymbol{m}_{\mathbf{r}'}\to\boldsymbol{m}(\mathbf{x})\times a\partial_x\boldsymbol{m}(\mathbf{x})$, taking the current in the x-direction. Keeping these contributions, we find that the transverse spin-current density to lowest order in magnetization gradients satisfies Eq. (5.1) with $g = a(16M_s/g_L\mu_BP)\times(G_0\mathrm{t}^{t}(\epsilon_F)/\mathrm{t}(\epsilon_F))$, where $\mathrm{t}(\epsilon_F)$ is the total (*i.e.*, summed for both spin channels) transmission probability. Both this transmission probability, and the spin-dependent transmission probability are taken between leads at neighboring sites and are taken at the Fermi energy. Also note that these transmission probabilities are

evaluated for the homogeneous ferromagnetic state, as Eq.(5.6) is already first order in magnetization gradient.

5.3 Spin spiral and inverse spin Hall effect detection

We now calculate the spin accumulation in the normal metal due to the injected spin current, for a *static* magnetization texture $\boldsymbol{m}(x)$ depending on the coordinate x along the wire. The spin diffusion equation for the spin accumulation, is given by

$$\nabla^2 \boldsymbol{\mu}_s = \frac{\boldsymbol{\mu}_s}{\lambda_{\rm sd}^2}, \tag{5.7}$$

where $\lambda_{\rm sd} \equiv \sqrt{D_s \tau_{\rm sf}}$ is the spin-diffusion length in the NM, and D_s and $\tau_{\rm sf}$ are its spin-diffusion constant and spin-flip time, respectively. The boundary conditions for Eq. (5.7) enforce continuity for the spin current and are given by

$$\partial_z \boldsymbol{\mu}_s(x,z)|_{z=0} = -\frac{G_0}{\sigma} \boldsymbol{j}_{s,z}^{\rm net}(x); \tag{5.8}$$

$$\partial_z \boldsymbol{\mu}_s(x,z)|_{z=d_N} = 0; \tag{5.9}$$

$$\partial_x \boldsymbol{\mu}_s(x,z)|_{x=\pm L_N} = 0, \tag{5.10}$$

where L_N, d_N and σ are the length, thickness and conductivity of the NM respectively, $\boldsymbol{j}_{s,z}^{\rm net}(x)$ is the net spin current into the NM. The net spin current is the sum of the spin-injection, as given in Eq. (5.1), and a backflow spin current $\boldsymbol{j}_s^{\rm back}$ in the opposite direction due to the induced spin accumulation on the NM side of the interface. Thus $\boldsymbol{j}_{s,z}^{\rm net} = \boldsymbol{j}_{s,z}^{\rm in} + \boldsymbol{j}_{s,z}^{\rm back}$, where [148]

$$\boldsymbol{j}_{s,z}^{\rm back} = \frac{g^{\uparrow\downarrow}}{4\pi G_0} \boldsymbol{\mu}_s(x, z=0), \tag{5.11}$$

where $g^{\uparrow\downarrow}$ is the mixing conductance. (We neglect the imaginary part of the mixing conductance, which is justified for realistic interfaces.[149]) We note that in the absence of dissipation that leads to spin relaxation in the normal metal the net spin current across the interface would be zero as the injected spin current would be exactly canceled by the backflow spin current.

For a static helical, *i.e.*, spiral magnetization, given by $\boldsymbol{m}_{\rm sp}(\boldsymbol{x}) = (0, \cos qx, \sin qx)^T$, the injected transverse spin current is independent on the x-coordinate, and can be measured using a Hall type geometry possible as shown in Fig. 5.1. For an FM-Pt bilayer with this geometry the large ISHE [150, 151] in the Pt converts the injected spin current into a voltage difference perpendicular to the direction of applied current. After solving the spin diffusion equation the voltage difference averaged over the thickness d_N of the Pt layer due to the ISHE is given by

$$\frac{V_{\rm ISHE}}{g/g^{\uparrow\downarrow}} = \frac{\hbar W \theta_{\rm SH}}{d_N |e|} q v_s \frac{\cosh \frac{d_N}{\lambda_{\rm sd}} - 1}{\frac{4\pi\sigma}{g^{\uparrow\downarrow}\lambda_{\rm sd}} \sinh \frac{d_N}{\lambda_{\rm sd}} + \cosh \frac{d_N}{\lambda_{\rm sd}}},$$

where W is the width of the FM-Pt interface and $\theta_{\rm SH}$ is the spin-Hall angle of Pt. Note that the thickness of the Pt-layer influences the signal considerably. [152] For the ferromagnet we take the helimagnet MnSi which supports spin spirals with $q \sim 2\pi/20\,\mathrm{nm}^{-1}$. For a MnSi-Pt interface we estimate $g^{\uparrow\downarrow} \approx 10^{15}\Omega^{-1}\mathrm{m}^{-2}$, $\sigma_{\rm Pt} = 9.5 \cdot 10^{6}\Omega^{-1}\mathrm{m}^{-1}$, a spin diffusion length $\lambda_{\rm sd} = 1.5$nm, and a platinum thickness of $d_N = 3$nm, $\theta_{\rm SH} = .05$, and obtain $V_{\rm ISHE}/W \approx 1.5(g/g^{\uparrow\downarrow})\,\mathrm{V/m}$, for a current density in the MnSi of $j_c \approx 10^{11}\mathrm{Am}^{-2}$, where we assumed the spin velocity is of the order of the drift velocity.

5.4 Interfacial enhancement of spin transfer

Another implication of the injection of the spin current is the effect it has on the current-driven motion of e.g. a domain wall. This is important for the understanding of domain-wall dynamics in layered magnetic materials, that are the subject of ongoing research. [153] Note that up to this point we only considered static textures. For a moving domain-wall we should however also include the spin-pumping contribution [21, 130]

$$\boldsymbol{j}_s^{\rm pump} = \frac{\hbar g^{\uparrow\downarrow}}{4\pi G_0}\boldsymbol{m} \times \frac{\partial \boldsymbol{m}}{\partial t}. \tag{5.12}$$

For the inhomogeneous injection of transverse spin current the solution of Eq. (5.7) for the spin accumulation yields $\boldsymbol{\mu}_s(x,z) = \int dx' K(x-x',z)\boldsymbol{j}_{s,z}^{\rm net}(x')$ where the net spin-current is given by $\boldsymbol{j}_{s,z}^{\rm net} = \boldsymbol{j}_{s,z}^{\rm in+pump} + \boldsymbol{j}_{s,z}^{\rm back}$. The fourier transform of the kernel $K(x,z)$ is given by

$$\tilde{K}(k_x,z) = -\frac{G_0\lambda_{sd}}{\sigma}\frac{\cosh\left(\frac{z+d_N}{\lambda_{sd}}\sqrt{k_x^2\lambda_{sd}^2+1}\right)}{\sqrt{k_x^2\lambda_{sd}^2+1}\sinh\left(\frac{d_N}{\lambda_{sd}}\sqrt{k_x^2\lambda_{sd}^2+1}\right)}. \tag{5.13}$$

The total spin current ejected from the FM-layer reduces the angular momentum of the FM, inducing a torque which modifies the domain-wall dynamics. The Landau-Lifshitz-Gilbert (LLG) equation in the presence of this additional torque is given by

$$\begin{aligned}\frac{\partial \boldsymbol{m}}{\partial t} + v_s\frac{\partial \boldsymbol{m}}{\partial x} &= \alpha_0 \boldsymbol{m}\times\frac{\partial \boldsymbol{m}}{\partial t} - \frac{1}{\hbar}\boldsymbol{m}\times\frac{\delta E_{\rm MM}}{\delta \boldsymbol{m}} \\ &+ \beta_0 v_s \boldsymbol{m}\times\frac{\partial \boldsymbol{m}}{\partial x} + \frac{\gamma}{M_s d_F}\boldsymbol{j}_{s,z}^{\rm net},\end{aligned} \tag{5.14}$$

where α_0 and β_0 are the bulk Gilbert damping and non-adiabaticity parameter respectively and γ is the gyromagnetic ratio. Note that the spin current $\boldsymbol{j}_{\rm net}$ now also includes the spin pumping contribution in Eq. (5.12) as we now consider a dynamic texture. The FM has thickness d_F and hard-axis anisotropy $K_\perp$ which we take to be along the y-axis and is included in the energy functional $E_{\rm MM}$ that also contains the exchange and easy axis anisotropy that set the domain-wall width. The domain wall is described by the collective coordinates $\varphi_{\rm dw}(t)$ which is the azimuthal angle and $r_{\rm dw}(t)$ which is the domain wall position that enters in the polar angle $\theta_{\rm dw}(x,t) = 2\arctan\exp(x - r_{\rm dw}(t))/\lambda_{\rm dw}$,[14] viz. $\boldsymbol{m} = (\cos\varphi_{\rm dw}\sin\theta_{\rm dw}, \sin\varphi_{\rm dw}\sin\theta_{\rm dw}, \cos\theta_{\rm dw})^T$. From the LLG equation [Eq. (5.14)]

we obtain the equations of motion for the collective coordinates of the domain wall, which are given by

$$\dot{\varphi}_{\rm dw} + \alpha_\varphi \frac{\dot{r}_{\rm dw}}{\lambda_{\rm dw}} = \beta_\varphi \frac{v_s}{\lambda_{\rm dw}}; \tag{5.15}$$

$$\frac{\dot{r}_{\rm dw}}{\lambda_{dw}} - \alpha_r \dot{\varphi}_{\rm dw} = \frac{K_\perp}{2\hbar} \sin 2\varphi_{\rm dw} + \frac{v_s}{\lambda_{\rm dw}}, \tag{5.16}$$

where $\alpha_{r,\varphi}$ and β_φ are given by

$$\alpha_{r,\varphi} = \alpha_0 + \frac{\gamma\hbar g^{\uparrow\downarrow}}{4\pi M_s d_F}\mathcal{I}_{r,\varphi} \quad ; \quad \beta_\varphi = \beta_0 + \frac{\gamma\hbar g}{4\pi M_s d_F}\mathcal{I}_\varphi;$$
$$\mathcal{I}_\xi = \frac{4\pi G_0}{\hbar g^{\uparrow\downarrow}} \iint dx dx' \, \Pi(x-x') \boldsymbol{j}_{s,z}^{\rm in+pump}(x) \cdot \frac{\delta \boldsymbol{m}_{\rm dw}}{\delta \xi}(x'),$$

with $\xi = \{r, \varphi\}$ and where $\Pi(x-x')$ is given by

$$\Pi(x-x') = \int_{-\infty}^{\infty} \frac{dk_x}{2\pi} \left[1 - \frac{g^{\uparrow\downarrow}}{4\pi G_0}\tilde{K}(k_x, 0)\right]^{-1} e^{ik_x(x-x')}.$$

Note that the integrals $\mathcal{I}_{\varphi,r}$ are functions of the dimensionless parameters $\lambda_{\rm dw}/\lambda_{\rm sd}$, $d_N/\lambda_{\rm sd}$ and $g^{\uparrow\downarrow}\lambda_{\rm sd}/4\pi\sigma$. The average velocity of the current-driven domain wall is given by

$$\langle \dot{r}_{\rm dw} \rangle = \frac{\beta_\varphi}{\alpha_\varphi} v_s + \frac{\mathrm{sign}\left[1 - \frac{\beta_\varphi}{\alpha_\varphi}\right]}{1 + \alpha_r \alpha_\varphi} \mathrm{Re}\left[\sqrt{(1 - \frac{\beta_\varphi}{\alpha_\varphi})^2 v_s^2 - v_c^2}\right],$$

where the critical velocity is given by $v_c = K_\perp \lambda_{\rm dw}/2\hbar$. The ratio $\beta_\varphi/\alpha_\varphi$ determines the qualitative behavior of the domain-wall velocity as a function of current. In Fig. 5.2 this ratio is shown as a function of the thickness of the normal metal layers in the multilayer. Note that for $d_N \gg d_F$ the interface enhancement dominates over the bulk values, and that in the limit of a large ratio $\lambda_{\rm dw}/\lambda_{\rm sd}$ our result for α_φ coincides with interfacial enhancement of Gilbert damping in single-domain magnets.[21, 130] Also note that for moving domain-walls $j_{s,z}^{\rm in+pump} \propto (g v_s - g^{\uparrow\downarrow} v_{\rm dw})$, so that the net injected spin current goes down once the domain wall is set into motion.

5.5 Discussion and conclusions

In this Chapter we describe a mechanism for transverse spin injection across a FM-NM interface that is induced by a magnetization gradient along the current, and focused on the examples of spin spirals and domain walls. In the example of a domain wall, the spin-current injection takes place at the position of the domain wall which could lead to spin injection with control over spin polarization and location of injection. Moreover, due to the spin accumulation induced in the NM layer(s) the measured α and β parameters for domain-wall motion in multilayer systems will be different than their bulk values. We expect that this effect plays a role in all metallic heterostructure thin-film measurements

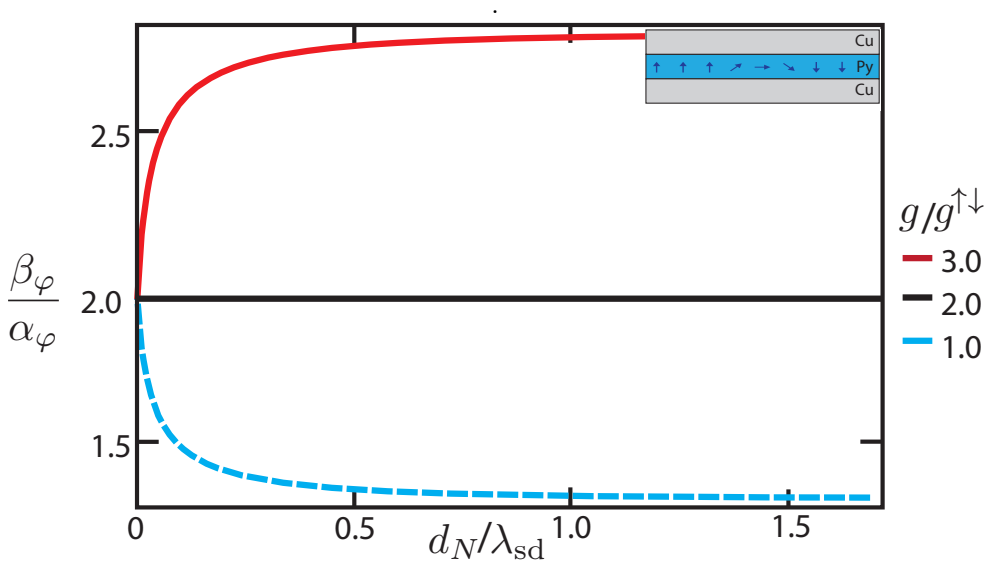

Figure 5.2: (Color online) The ratio $\beta_\varphi/\alpha_\varphi$ is shown as a function of the thickness $d_{\rm N}$ of the normal metal layers in units of its spin diffusion length $\lambda_{\rm sd} = 250$nm, for a Cu-Py-Cu multilayer. The head-to-head domain wall in the Py has a width of 100 nm. For $g/g^{\uparrow\downarrow} = 2$, where $g^{\uparrow\downarrow} = 1.6 \cdot 10^{15}\Omega^{-1}\mathrm{m}^{-2}$ is the mixing conductance of a Py-Cu interface the ratio, the ratio $\beta_\varphi/\alpha_\varphi = 2$ coincides with the bulk ratio with $\alpha_0 = 0.006$.

of domain-wall dynamics. In fact, large values of beta are typically reported in such systems,[154] pointing to the possibility of interfacial enhancement.

We can make a connection between the transverse spin-current injection and spin pumping. Consider spin-pumping by a precessing spiral magnetization in the absence of a current, [c.f. Eq. (5.1)] when the wavelength of the helix is much larger than the spin diffusion length in the ferromagnet. If the system would be Galilean invariant a Galilean transformation to the frame moving with velocity ω/q yields a static magnetization and a nonzero spin current leading to transverse spin-injection as given by Eq. (5.1) with $g/g^{\uparrow\downarrow} = 1$. Therefore we expect $g/g^{\uparrow\downarrow}$ to be of order unity. However, since Galilean invariance in practice is broken there is a difference between injection and pumping, analogous to the difference between the α and β parameters in the LLG equation. This is also reflected in the fact that the parameter g is a three-terminal transport property, since it involves transverse spin transport into one lead in response to longitudinal charge transport driven through two other leads [c.f. Eq. (5.6)], which is microscopically distinct from the two-terminal scattering processes contributing to $g^{\uparrow\downarrow}$ and spin-pumping.

It is also possible to give another interpretation of magnetic-texture-controlled transverse spin injection. We do this by considering the adiabatic spin transfer torque (STT)

[7, 8]

$$\left.\frac{\partial \boldsymbol{m}}{\partial t}\right|_{\mathrm{STT}} = -\left(\boldsymbol{v}_s \cdot \nabla\right) \boldsymbol{m} \propto \boldsymbol{m} \times \langle \boldsymbol{s} \rangle, \tag{5.17}$$

and interpret it as a torque due to a current-induced spin density $\langle \boldsymbol{s} \rangle \propto \boldsymbol{m} \times (\boldsymbol{v}_s \cdot \nabla)\, \boldsymbol{m}$ of the itinerant electrons. This non-equilibrium spin density may leak into the normal metal, giving rise to a spin current of the form in Eq. (5.1). We stress again, however, that for a microscopic treatment one has to resort to the formalism of Sec. 5.2 as, e.g., a diffusive treatment of the non-equilibrium spin density $\langle \boldsymbol{s} \rangle$ with boundary conditions at the interface between FM and NM will not involve the parameter g and thus not account correctly for the lack of Galilean invariance.

We also note that in principle there is a spin current with spin polarization in the direction of $(\boldsymbol{v}_s \cdot \nabla)\boldsymbol{m}$ that we have ignored as it oscillates and averages out to small values when integrated over position, and is determined approximately by the imaginary part of the mixing conductance which is small for realistic interfaces.

Other spin-injection mechanisms, like the spin-dependent Seebeck effect [143] or diffusive spin injection, [135] typically induce a spin current in the NM-layer with the spin polarization parallel to the magnetization in the ferromagnet. Therefore the spin-injection we discussed in this Chapter, which induces a spin current polarized in the direction of the helicity of the magnetic texture along the current, is distinguishable even when an inhomogeneous current distribution leads to current paths through the FM-NM interface and thus to injection of spin with polarization along the magnetization. Moreover, the spin current we propose is tunable in position and polarization via manipulation of the magnetization, in contrast to the SHE and other mechanisms of spin injection.

The Onsager reciprocal process of the spin-injection mechanism we discussed here occurs as well. A spin current with a spin direction aligned to the helicity of a magnetization texture injected into a ferromagnet leads to a voltage difference over the ferromagnetic strip. In this way domain walls could be used as a local movable sensors of spin current. In future work we plan to investigate transverse pure spin currents associated with heat currents in the same geometry as discussed here.

Chapter 6

Domain-wall motion in the two-dimensional random-bond Ising model

Abstract

We consider the field driven motion of domain walls in the two-dimensional ferromagnetic Ising model with random bond disorder. The nearest-neighbor bond strengths are $J+\Delta$ or $J-\Delta$ with equal probability. The disorder induces a pinning force F_p for the domain wall in our simulations. We are able to distinguish two regimes of domain-wall motion. For forces larger than the pinning force the domain-wall velocity is given by $v_{\mathrm{dw}} = \mu(F - F_p)$ where μ is the mobility and F is the driving force. We determine the dependence of μ and F_p on disorder strength Δ and temperature. For fields much slower than the critical force we observe domain-wall creep, so that $\ln v \propto (F_p/F)^{\mu}$ with $\mu = 1/4$.

6.1 Introduction

Field and current-driven motion of magnetic domain walls is an active field of study. This is due to the promising applications in magnetic memory and logic devices [20, 155]. Recent progress is made using materials with perpendicular magnetic anisotropy (PMA) where the magnetization points out of the plane of the nanowire. The strong magnetic anisotropy of PMA materials implies that the domain walls are very narrow leading to efficient depinning and motion under the influence of a driving force. The typical systems used for creation of perpendicular magnetized materials, such as Pt/Co (multi-)layers, create a very thin magnetic layer. The dynamics of these domain walls are under intense experimental scrutiny. In the absence of disorder and pinning sites the dynamics can be understood using the 1D domain-wall model we discussed in the previous Chapters. For motion through a disorder landscape the domain wall moves by the movement of segments of it between pinning sites. In this way the domain wall creeps from metastable state to metastable state in the energy landscape. The motion of the domain wall can be very slow due to the disorder. A better understanding how the velocity depends on the disorder strength may help to create fast and reliable non-volatile memory devices.

The understanding of the motion of domain walls through disordered landscapes is a tough theoretical challenge. Therefore we study the motion of domain walls using a simple crude model. Arguably one of the simplest models to understand magnetism is the Ising model which in two-dimensions was solved by Onsager [156]. The 2D ferromagnetic Ising model consists of a lattice with spins pointing either up or down. Therefor it closely resembles the perpendicular magnetized materials with strong anisotropy, where the domain walls are very narrow. But the similarities between experimental systems and the Ising model end here.

The reason why we might learn something for PMA systems in particular or magnets in general from studying the Ising model comes from the notion of universality classes. The critical exponents associated with the phase transition from the unordered to the ordered phase are the same for all systems belonging to the same universality class. As we explain below, creep motion is determined by the static roughness exponent and dimensionality of the domain wall. The roughness exponent is universal and does not depend on the microscopic details of the system. Therefore we expect to learn something about real systems by considering the simulation-friendly Ising model.

In this Chapter we consider the motion of domain walls in the two-dimensional Ising model with short-ranged random bond (RB) disorder. We introduce bond disorder to study the effects disorder has on the field driven motion of the domain wall. The equilibrium static roughness or wandering exponent for RB disorder is given by $\zeta_{\mathrm{RB}} = 2/3$ for a domain wall in a 2D ferromagnet [157, 158], which was also obtained in experiments on thin magnetic films [159–162]. This in contrast to random field disorder as studied in [163, 164] which leads to a roughness exponent $\zeta_{\mathrm{RF}} = 1$.

Beside the promising applications of magnetic domain walls, the motion of an elastic interface through a disordered landscape underlies a broad range of physical phenomena, such as moving vortices in superconductors [158], wetting phenomena [165] and propagating crack fronts [166]. For all of these examples it holds that the interplay between the elasticity of the interface and the pinning induced by the disorder in the presence of thermal fluctuations gives rise to different regimes of the driven motion of the interface.

Before we can study the creep motion of domain walls in the RB Ising model (RBIM) we have to locate this regime in the parameter space. This turns out not to be a simple task. Even in the absence of disorder, where we naively expected simple linear response of the domain wall, we obtained a nonlinear dependence of the velocity on the applied field. In the presence of disorder we obtain a critical field H_c. For fields above the critical field H_c the domain wall is in the flow regime where the velocity is given by the linear relation

$$v_{\mathrm{dw}} = \mu_{\mathrm{dw}} \, (H - H_c) \quad (H \gg H_c), \tag{6.1}$$

where μ_{dw} is the mobility of the domain wall. In the zero temperature limit the domain-wall velocity should scale as $v_{\mathrm{dw}} \propto (H - H_c)^{\beta}$ around the depinning field, where β is the depinning exponent [167]. All our data is consistent with $\beta = 1$. At finite temperatures the depinning transition will be smeared due to thermal fluctuations. The critical velocity scales with the temperature as $v_c \equiv v_{\mathrm{dw}}(H = H_c) \propto T^{\psi}$ [168, 169]. Here we do not address the interesting depinning regime since it requires sample-to-sample determination

of the pinning field H_c which is unfeasible in our implementation. Instead we focus on the regime below depinning were the velocity is theorized to be given by the creep law. Before we can study this regime, we need to determine the critical field H_c.

For small driving fields $H \ll H_c$ the interface is pinned and can only move due to thermal fluctuations. For very low driving fields the average velocity is of the form

$$v_{\mathrm{dw}} \propto \exp\left\{-\beta E_p \left(\frac{H_c}{H}\right)^{\mu}\right\}, \tag{6.2}$$

which describes the motion in the creep regime [170]. In the above equation we defined E_p as a characteristic energy scale, $\beta \equiv (1/k_B T)$ is the inverse thermal energy and μ is the creep exponent. The creep exponent depends on the dimensionality of the system and the static roughness exponent of the domain wall.

In order to describe the roughness we introduce the roughness function w as a measure for the roughness of the domain wall. It is defined as the thermal and disorder averaged variation of the domain-wall position $r_{\mathrm{dw}}(z,t)$ via the relation

$$w^2(L,t) = \left\langle \left(r_{\mathrm{dw}}(z+L,t) - r_{\mathrm{dw}}(z,t)\right)^2 \right\rangle, \tag{6.3}$$

which for $L > L_c$ scales as

$$w^2(L) \propto L^{2\zeta} \quad \text{for} \quad (L > L_c), \tag{6.4}$$

where ζ is the roughness exponent and L_c is the crossover length scale between thermally induced roughness and disorder induced roughness, which is known as the Larkin length and was first introduced for vortex lines in superconductors [170]. On length scales below the Larkin length the domain-wall roughness is determined by thermal fluctuations that induce a roughness with $\zeta_T = \frac{1}{2}$, whereas above it the form of the wall and thus the roughness will be determined by the disorder. For the one-dimensional domain wall in the 2D RBIM the disorder induces $\zeta_{\mathrm{RB}} = \frac{2}{3}$ [157]. Note that for random field disorder, where the effect of the disorder scales with the surface enclosed by the domain wall, the roughness exponent is $\zeta_{\mathrm{RF}} = 1$. The exponent for the creep motion is given by $\mu = (d-2+2\zeta)/(2-\zeta)$, which for the RBIM studied in this Chapter, with the dimension of the wall $d = 1$, yields $\mu = 1/4$.

The main purpose of this Chapter is to study the field driven motion of the domain wall through a disorder landscape with an emphasis on the low driving field behavior. In the next Section we describe the model and its implementation of the RBIM in two dimensions. Before we turn to field driven motion in the flow (Sec. 6.4) and creep regimes (Sec. 6.5) we first study the roughness of the domain walls since the equilibrium properties determine the exponent of the creep regime.

6.2 Model and implementation

The energy of the field driven RBIM is given by

$$\mathcal{H} = -\sum_{\langle i,j \rangle} J_{ij}\sigma_i\sigma_j - H\sum_i \sigma_i \tag{6.5}$$

where $\sigma_i \in \{-1, 1\}$ is the Ising spin at lattice site i, $\langle i, j\rangle$ denotes nearest-neighbor pairs and H is the external magnetic field that drives the domain wall. The RB disorder is characterized by the coupling between nearest-neighbors is $J_{ij} = J \pm J\Delta$, where $1 > \Delta > 0$, such that

$$\langle J_{ij}\rangle_{\rm dis} = J; \tag{6.6}$$

$$\langle J_{ij}J_{i'j'}\rangle_{\rm dis} = J^2 + J^2\Delta^2\delta_{ii'}\delta_{jj'}, \tag{6.7}$$

where the brackets here denote the average over disorder configurations.

Simulations are performed on a square lattice with dimensions $L \times W$. The boundary conditions are periodic in the W direction and antiperiodic in the L direction. This induces the topology of a Klein bottle on the system. This non-orientable surface without boundaries makes sure we always have at least one domain wall below the critical temperature. We drive the domain wall on average always from left to right, thus we switch the direction of the driving field once the domain wall reaches the edge of our system. We switch the sign of the field in the half of the sample where the domain wall is not located. For reasons of clarity we ignore the extra signs to accommodate this technical detail of the implementation of the system in the definition of the domain-wall position below.

We use the Metropolis algorithm with single spin-flip dynamics to study the dynamics of the RBIM [171]. We use multispin coding where we use a single bit per spin such that we work with 64 different disorder configurations in parallel on our 64-bit machine. The disorder averaged results we present below are the averages over these different configurations.

Let $r_{\rm dw}(z,t)$ be a single valued function that defines the position of the domain wall as a function of the coordinate along the short direction $0 \le z < W$ and time. The position is defined via the function $f(r_{\rm dw}(z,t),z,t) \ge f(r,z,t)$ for all $r \in L_z$ where L_z are the spins in row z. The function is given by

$$f(r,z,t) = \sum_{i\in L_z} \Theta_{i,r}\sigma_i(t),$$

where

$$\Theta_{i,j} = \begin{cases} 1 & i < j \\ -1 & i \ge j \end{cases}$$

The single valuedness of the function implies that we ignore overhangs or multiple domain walls in our sample. These effects are also ignored in the works concerning roughness and creep motion.

The lattice is initialized at zero temperature with a domain wall located at the center, *i.e.*, all spins are aligned with the external field left of the middle and antialigned on the other half. Once every fifty Monte Carlo steps per lattice site the domain-wall position $r_{\rm dw}(z,t)$ is measured. Since the initialization of the system is out of equilibrium we expect, and observe, transient effects before we reach steady state. The transient effects are then discarded and we investigate the steady state characteristics of the domain-wall motion.

6.3 Equilibrium

In this Section we introduce the background necessary to interpret the results of the following Sections. We start with a discussion of the equilibrium properties of domain walls in the RBIM. We begin with a discussion of the roughness of domain walls. The domain wall can be described as an elastic string moving through a disorder landscape. The energy for this elastic string is given by

$$E_{\mathrm{dw}} = \int dz \frac{\Gamma}{2} (\nabla r_{\mathrm{dw}}(z))^2 + V_{\mathrm{dis}}(r_{\mathrm{dw}}(z)), \tag{6.8}$$

where the first term is the contribution due to the interface tension Γ, and the second term is the energy contribution due to the disorder landscape. In addition to the thermal roughening the bond disorder induces additional roughening of the domain wall. In the absence of disorder and at zero temperature domain walls are completely flat due to the elastic energy of the interface. At non-zero temperature the domain wall is rough due to thermal fluctuations. The description of the domain wall as an elastic string then leads to an energy per mode $E_k = k^2 \tilde{r}^2_{\mathrm{dw}}(k)/2\Gamma$. Equipartition then leads to the scaling relation,

$$S_k \propto \frac{k^{-2}}{\beta\Gamma}, \tag{6.9}$$

where the structure factor is defined as

$$S_k = \left\langle \left| \frac{1}{W} \sum_{z=0}^{W-1} u(z) e^{-i\frac{2\pi k z}{W}} \right|^2 \right\rangle,$$

where $u(z) = r_{\mathrm{dw}}(z) - r_{\mathrm{dw}}$ is the deviation from the average wall position and the wave number $k \in \{1, 2, \ldots, W-1\}$. From dimensional analysis we see that $S_k \propto k^{-(1+2\zeta)}$ when $w(L)^{2\zeta} \propto L^{2\zeta}$. The result in Eq. (6.9) thus implies the thermal roughness or wandering exponent $\zeta_T = 1/2$. In Fig. 6.1 we show the thermal and disorder averaged amplitudes of the modes of the domain wall. At short length scales (long wave lengths) the data differs from the k^{-2} scaling, this is due to the finite size of the lattice. At low temperatures and weak disorder the data is well described by [172] $\tilde{r}_{\mathrm{dw}}(k) \propto (\sin(\pi k/W))^{-2}$, which is a low temperature expression incorporating only the smallest fluctuations around the flat $T = 0$ result in the absence of disorder. Note that for length scales long compared to the lattice the expression reduces to the result for the elastic string. In Fig. 6.1 the dashed lines correspond to the wandering exponent $\zeta = 2/3$ confirming the expectations for the RBIM for the systems where disorder is present. The crossover to the thermally induced roughness is a measure for the Larkin length of the system, the crossover length scale decreases for increasing disorder strengths. Unfortunately the data quality in our samples was too poor to be able to do a systematic analysis on this crossover and the wandering exponent. However consistency of the data over a range of temperatures and disorder strengths with $\zeta = 2/3$ is observed, and are supported by the creep exponent of $\mu = 1/4$ in our results on the motion of domain walls in the creep regime, see Sec. 6.5. In

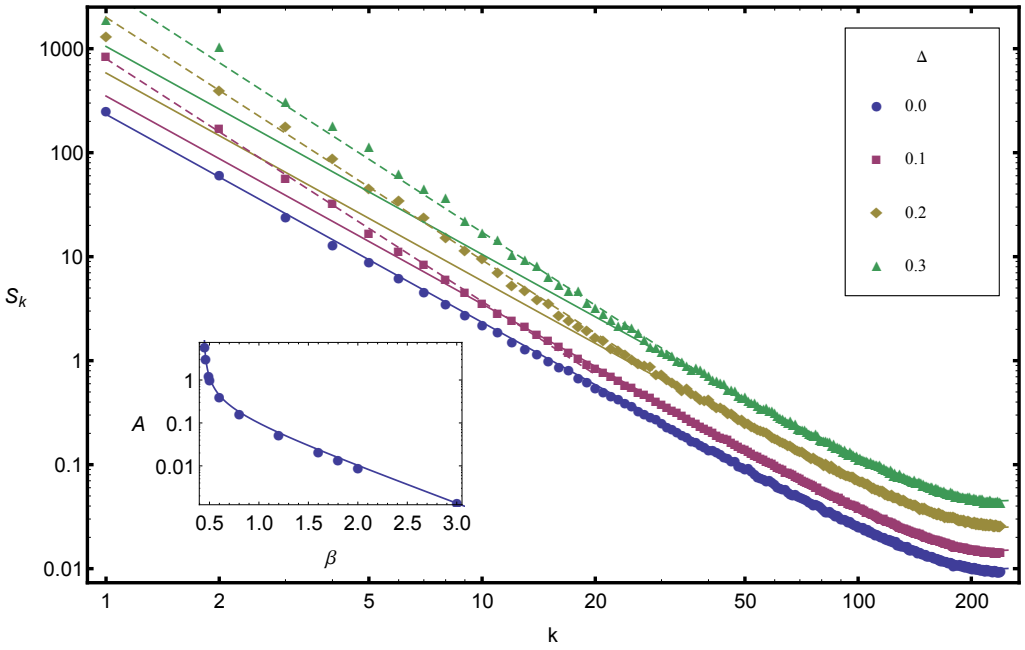

Figure 6.1: The structure factor as a function of wave number k for $\beta = 2.0$. Solid lines are fits to the function $S_k = A(\beta)\left[\sin(2\pi k/480)\right]^{-2}$ that correspond to the thermal regime. Dashed lines correspond fits $S_k \propto k^{-(1+2\zeta_{\mathrm{RB}})}$, with $\zeta_{\mathrm{RB}} = 2/3$ the random bond roughness exponent. The inset shows how the amplitude $A(\beta)$ scales for various temperatures without disorder. The solid line corresponds to $(\beta\Gamma)^{-1}$.

the inset we show the prefactor A for the thermal scaling regime for various temperatures and show that it agrees with Eq. (6.9), where the effective interface tension given by

$$\Gamma = \beta^{-1}\sinh(\beta\sigma_0) \tag{6.10}$$

is predicted by capillary wave theory [173] with

$$\beta\sigma_0 = 2J\beta + \log\tanh\beta J, \tag{6.11}$$

which is Onsager's [156] result for the surface tension σ_0 of the 2D Ising model.

6.4 Flow regime

Now we can investigate the out-of-equilibrium steady-state dynamics of the domain walls. In this Section and the next we study the velocity, $v_{\mathrm{dw}}(t) = \langle \partial_t r_{\mathrm{dw}}(t)\rangle$, of the domain wall as a function of applied driving field. The dynamics of the domain wall can be understood as the motion through a disordered energy landscape. The effect of the driving field on the energy of the domain wall can be considered as simply tilting the energy landscape.

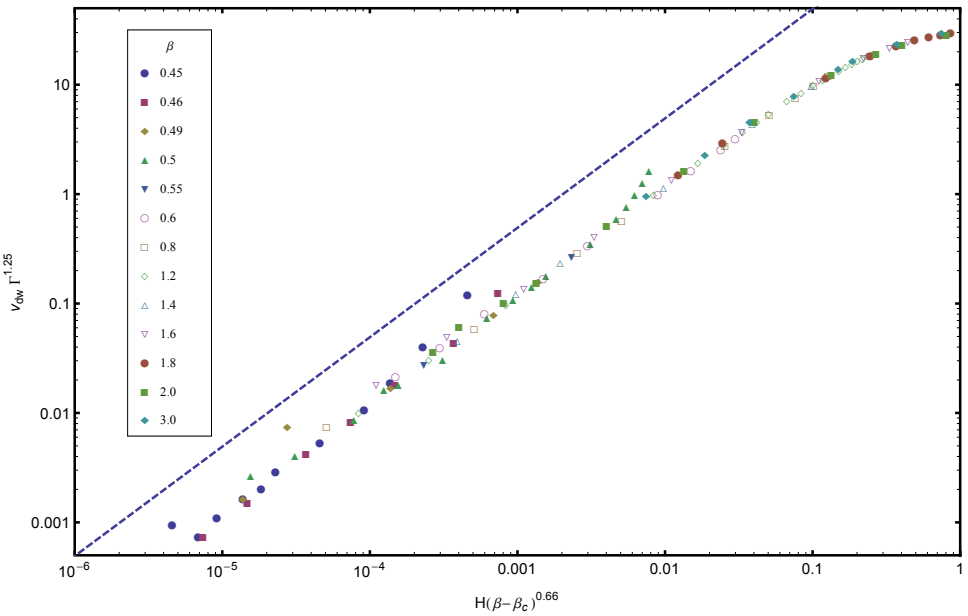

Figure 6.2: The scaled domain-wall velocity as function of external field for various temperatures in the absence of disorder. The dashed line corresponds $v_{\mathrm{dw}} \propto H$ and is a guide to the eye. For low temperatures the velocity depends sublinearly on the external field for higher driving fields.

In this Section we study the flow regime of domain-wall motion. In this regime the domain-wall velocity depends to the external field via a linear relationship. In order to extract the the domain-wall mobility $\mu(\beta, \Delta)$ as a function of temperature and disorder strength we first study the velocity in the disorder free ($\Delta = 0$) limit. In Fig. 6.2 the velocity of the domain wall is plotted as a function of the driving field in the absence of disorder for various temperatures. The velocity is scaled with a power of the effective interface tension $\Gamma^{1.25}$, and the driving fied is scaled by the $(\beta - \beta_c)^{0.66}$. Using this scaling, a collapse of the data over several orders of magnitude is obtained.

In the absence of disorder a linear dependence on the external field is expected, *i.e.* $v_{\mathrm{dw}} = \mu_{\mathrm{dw}} H$. We observe this linear scaling for low and intermediate driving fields. For high driving fields two effects are present.

For temperatures close to the critical temperature we see the nucleation of smaller extra domains that coalesce with the favored domain leading to a stronger than linear dependence on the external field. This behavior can be observed in Fig. 6.2 for the inverse temperatures $\beta = \{0.45, 0.5\}$, where the velocities increase stronger than linearly with the field for high field strengths.

For high driving fields at low temperatures the velocity scales sublinearly with the applied field. We attribute this difference to the finite size of our system. At low temperatures the domain walls in our finite size samples become completely flat. And

the motion of the wall is governed by the chance of flipping one spin at the edge of the domain wall. After this single spin is flipped a whole line of spins will, due to the high field, immediately be added. Then it will again take time for the addition of a new line. In our finite size system will be flatter than the thermal roughness an infinite sample will show. Since the progression of the wall is mainly due to growth near imperfections from flatness this leads to a sublinear scaling with the field.

For driving field strengths large compared to the temperature, both nucleation and finite-size induced slowing lead to a nonlinear dependence of the domain-wall velocity on the field which is incompatible with the flow regime. These effects can also be observed in the presence of disorder, see Fig. 6.3a, and have opposite effects on the dependence of the velocity on the driving field. In this figure we see the velocity of the domain wall versus the applied field for a temperature of $\beta = 0.8$ for increasing values of the strength of the disorder. We can clearly see the sublinear scaling of the velocity for low disorder strength and the superlinear scaling due to nucleation. These observations strengthen our interpretation of the described effects. As we increase the disorder the domain wall becomes less flat due to the disorder induced roughening. This means that the sublinear scaling sets in at higher field values. Contrary to this effect is that the nucleation of small domains that can be added to the moving wall sets in at lower driving fields since the disorder also changes the critical temperature of the RBIM [174]. The critical temperature in the presence of disorder is determined by the equation

$$\sinh(2\beta_c J(1+\Delta))\sinh(2\beta_c J(1-\Delta)) = 1. \tag{6.12}$$

Together with the fact that the flow region starts at increasing critical field strengths with increasing disorder means that the determination of the mobility becomes nontrivial for the high disorder and high temperature regime where it is hard to determine the linear scaling.

This means that for systems where we need rather high driving fields to overcome the critical field, it is hard to distinguish truly linear dependence from the conspiracy of the finite size and nucleation effects. In what follows we restrict ourselves to investigations of the domain-wall velocity from low to moderate values of the driving fields since we intend to study creep motion that is supposed to take place in this regime. Therefore we choose not to study the finite size and nucleation effects in more detail here.

As introduced before, disorder induces a critical field H_c below which the domain wall is pinned and can move only with thermal assistance, which is the subject of the next Section. For fields above the depinning threshold the velocity is given by the linear relation given in Eq. (6.1) that holds for $H > H_c$.

In Fig. 6.3a we show the scaled domain-wall velocity for $\beta = 0.8$ as a function of $H - H_c(\Delta)$. In the figure we used the scaling $H_c \propto \Delta^2$. Data for different temperatures is consistent with scaling $H_c \propto \Delta^\nu$ for the exponent in the range $\nu \in [1.9, 2.2]$. We do not have enough data to determine the form of the dependence of the critical field on temperature. The dependence on the disorder strength of the critical field is understood easily, stronger disorder leads to higher energy barriers to overcome. The temperature dependence of the critical field may be rooted in the temperature dependence of interface

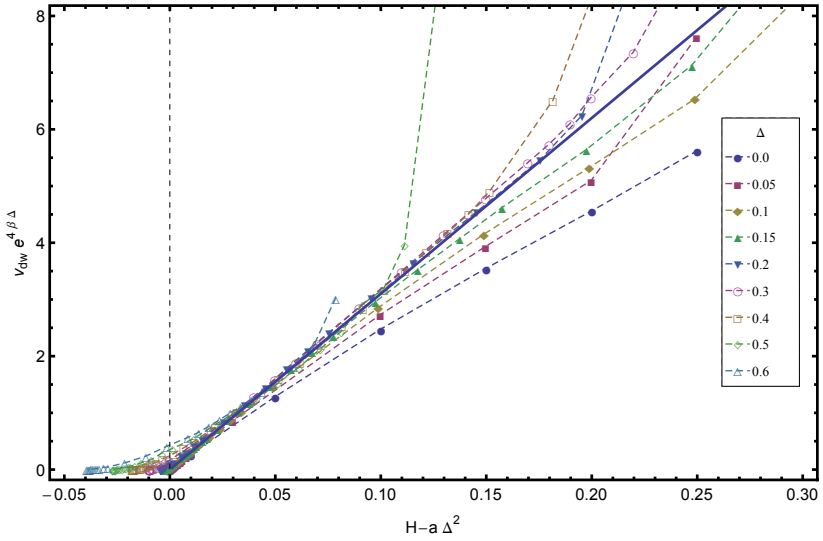

(a) Scaled domain-wall velocity versus $H - H_c$, where the critical field scales as $H_c = a\Delta^2$ with $a = 0.115$, for various disorder strengths at an inverse temperature of $\beta = 0.8$. At high fields we see the sublinear scaling for low disorder strengths that turn into nucleation dominated domain-wall motion for higher disorder strengths or even higher fields. For fields just above the critical field the data is well described by Eq. (6.1).

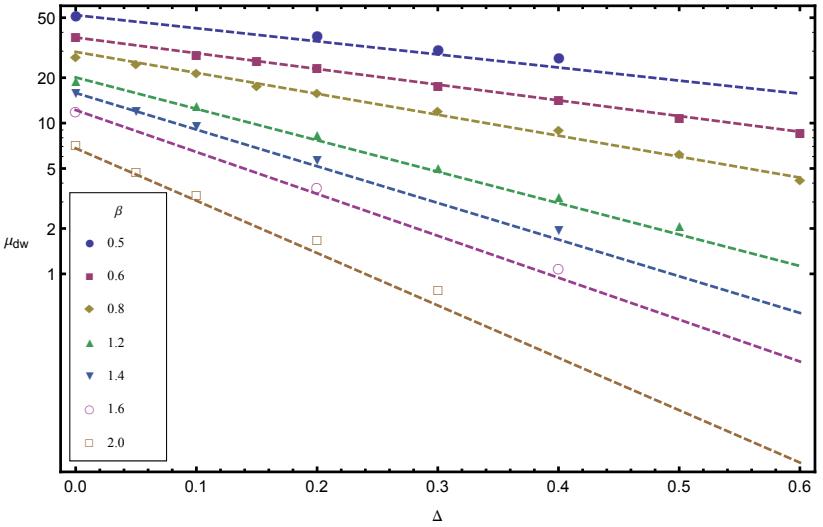

(b) The mobility of the domain wall as a function of disorder strength for the temperatures $\beta = \{0.5, 0.6, 0.8, 1.2, 1.4, 1.6, 2.0\}$ from top to bottom. The dashed lines correspond to Eq. (6.13), with $A = 4.0$ and $\mu_0 = 115$.

Figure 6.3

tension of the wall. For very low temperatures the cost of bending around a weak pinning site may be prohibitively expensive due to the elastic energy cost. Another explanation for the temperature dependence of the critical field can be the driving force on the domain wall is not just the driving field, but given by the combination $HM(\beta, \Delta)$, where $M(\beta, \Delta)$ is the magnetization as function of temperature and disorder.

The velocities of the domain walls are scaled in Fig. 6.3a. For the moderate values of the fields we can measure the mobility accurately and in Fig. 6.3b we show the result for the domain-wall mobility for various disorder strengths and temperatures. The dashed lines, which are consistent with all fitted mobilities, correspond to

$$\mu(\beta, \Delta) = \mu_0(\beta) \exp\left(-4\beta\Delta\right), \tag{6.13}$$

where $\mu_0(\beta)$ can be obtained from the disorder free system, as shown in Fig. 6.2, given by

$$\mu_0(\beta) \propto (\beta - \beta_c)^{0.66} \Gamma(\beta)^{-1.25}. \tag{6.14}$$

We can compare the dependence of the mobility on the disorder strength and temperature to thermally assisted flux flow (TAFF) [175, 176], that can be understood as follows. Note that TAFF is supposed to describe the motion below a depinning transition. It is, however, useful to introduce TAFF to refer to when we discuss creep motion. Suppose that the disorder landscape has a characteristic length scale l between characteristic energy barriers U_b. In the presence of a driving field the landscape is tilted leading to a exponentially small linear response given by the Arrhenius law

$$v_{\mathrm{dw}} \propto \frac{a}{\tau_f} - \frac{a}{\tau_b} \approx a \left(e^{-\beta(U_b - Ha/2)} - e^{-\beta(U_b + Ha/2)} \right) \propto e^{-\beta U_b} H, \tag{6.15}$$

where the we used the Arrhenius law for the forward and backward hopping rates τ_f^{-1} and τ_b^{-1}. When the barriers obey $U_b \propto \Delta$ we have a form similar to Eq. (6.13). However, our data does not show another regime, for higher fields as one should expect following the TAFF interpretation. Given the dependence on the effective interface tension in the absence of disorder, it could very well be that the the disorder not only creates pinning sites that slow down the domain wall, but has an effect on the interface tension of the wall. We do not address this issue further in this Chapter.

6.5 Creep regime

In this Section we study the velocity of the domain wall as a function of the driving field for fields below the critical fields defined in the previous Section. Before we consider the results of the simulations, as shown in Fig. 6.4, we motivate Eq. (6.2) that describes creep motion. Creep motion is based on two assumptions. The first is that the motion is sufficiently slow such that we can use a quasi-static description of the domain wall. The second assumption is that the scaling, with the length L of a displaced segment, for the energy barriers between metastable states is the same as the scaling with this length of the metastable states, as given in Eq. (6.16).

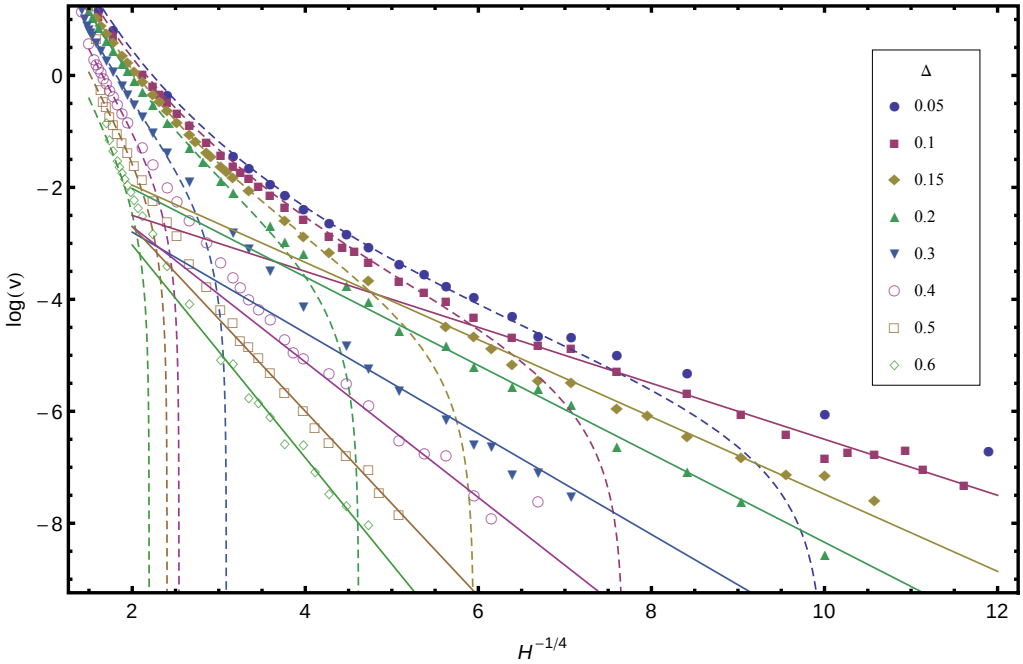

Figure 6.4: The natural logarithm of the velocity of the domain wall versus $H^{-1/4}$ for $\beta = 0.8$. Dashed lines correspond to $v_{\mathrm{dw}} = \mu(H - H_c)$ for $H > H_c$, with the fitted mobilities and critical fields obtained in Sec. 6.4. The straight solid lines are guides to the eye consistent with a creep law for the velocity with $\mu = 1/4$.

In the Sec. 6.3 we saw that the disorder introduced a scaling relation for the variations in the domain wall $w^2(L) \propto L^{2\zeta}$. This scaling relation implies that the energy of a displaced segment of length L is given by [159, 176]

$$E(L) \propto L^{d-2+2\zeta} - HL^{d+\zeta}, \tag{6.16}$$

where the first term comes from the elastic energy of the roughened wall and the second term describes the energy gain due to external field. The energy depends nonmonotonically on the length scale which means we can introduce the optimal length L_* via the minimalization of the above equation, this yields

$$L_* \propto H^{-\frac{1}{2-\zeta}}.$$

This length L_* determines the lowest energy cost of a displacement. The energy barrier associated with the displacement of a segment of the wall with this length is then, via Eq.6.16, given by

$$U_b(F) \propto E(L_*) \propto H^{-\frac{d-2+2\zeta}{2-\zeta}}. \tag{6.17}$$

Note the difference with our discussion of the TAFF in the previous Section where the barrier height was given by a characteristic value independent of the field. The

dependence of the barrier on the driving field is common in of the glassy systems [176]. If we then use the Arrhenius law to describe the rate at which the barriers are overcome we can safely assume that all motion comes from the movement of segments with the optimal length, since longer or shorter segments result in energy barriers that are exponentially suppressed. We thus find that the velocity in the creep regime is given by

$$v = v_0 \exp\left[-\frac{U_c}{k_B T} H^{-\mu}\right], \tag{6.18}$$

where we introduced the parameters U_c and v_0 that we determine from our data. In Fig. 6.4 we plotted the logarithm of the velocity versus $H^{-1/4}$. For the velocities below the critical field we find the data is consistent with creep motion given by Eq. (6.18).

In Fig. 6.5 we show the data of our simulations for field values below the critical fields that we determined in the previous Section. Again we plot the logarithm of the velocity versus $H^{-1/4}$ which should result in straight lines. In addition we have scaled the axes with powers of the inverse temperature and disorder strength and obtained a collapse of the data for all disorder strengths at separate temperatures. The collapse is consistent with the predictions of the creep regime, since the points fall on straight lines in the figure. Note that the lines all have the same slope which means that we only need the dependence of v_0 in Eq. (6.18) on temperature to get a collapse of all data points. However, we were unable to obtain such a collapse, since v_0 does not seem to scale with a power of the temperature.

6.6 Discussion

In this Chapter we studied domain walls in the RBIM. Our results are consistent with the predicted thermal and random-bond induced roughness exponents. In future work it is necessary to obtain better quality data for a range of disorder strengths and temperatures to determine the exponents and it would be interesting to study the dependence of the crossover length scale L_c on the disorder strength, temperature and external field.

Furthermore we studied the influence of a driving field on the motion of a domain wall. Before we could study the creep regime in the last Section we needed to determine the critical field H_c as a function of disorder and temperature, to determine in what parameter regime to expect the creep motion. The velocity versus field characteristics of the RBIM proved to be rather nontrivial. Already in the absence of disorder two different mechanisms leading to nonlinear dependence were observed. The physical mechanism that determines the dependence of the domain-wall mobility on temperature via the effective interface tension, in the absence of disorder, as given by Eq. (6.14), is not understood. However due to the good collapse of the data we could determine how disorder changes the mobility. Both the roughness and mobility depend on the effective interface tension of the Ising model, as shown in Figs. 6.1 and 6.2. If the change in the mobility due to disorder, comes from a changed effective surface tension, then this change should also be measurable from the amplitude associated to the $\propto k^{-2}$ regime of the roughness, thus on length scales below the Larkin length. With this hypothesis we

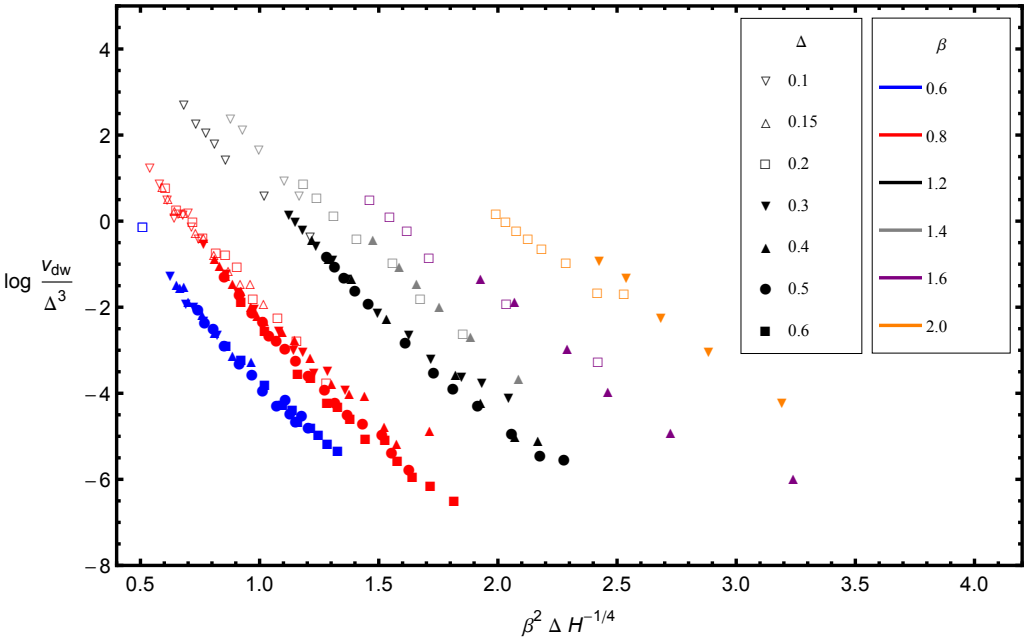

Figure 6.5: Domain-wall velocities for driving fields below the critical field as determined in Sec. 6.4 for various temperatures and disorder strengths. On the vertical axes we have $\log v/\Delta^3$ versus $\beta^2\Delta H^{-1/4}$ in the horizontal axes.

looked at this disorder dependence of the roughness and the data with poor quality that we have in this regime seems to agree with it. In addition to the mobility we were able to measure the critical fields H_c as a function of disorder and temperature and found a $H_c \propto \Delta^2$ relation.

Using the results for the critical fields we were able to isolate the creep regime. The results presented in this Chapter are not conclusive about the value of the creep exponent μ or the existence of the regime. In Fig. 6.5 we showed a collapse of the data with the same disorder strength for various temperatures indicating creep behavior. However a fit of the creep formula as given in Eq. (6.18) to the data with three parameters v_0, U_c yields inconclusive results. This due to the limited number of data points available in the creep regime.

In this Chapter we assumed the domain walls move linearly with time, leading to a well defined velocity. However, for low driving fields the motion of the walls can be interpreted, alternatively, as anomalous diffusion where the position depends on time nonlinearly. This type of motion was not systematically studied here, because the interpretation in terms of the creep behavior is consistent with the data, which is also observed experimentally giving it further credibility. Better data quality for the static and dynamic roughness will vastly improve our understanding of the results presented in this Chapter.

Hoofdstuk 7

Samenvatting

Iedere minuut wordt er honderd uur aan filmpjes geüpload naar YouTube [177]. Of het nu het 1,8 miljard keer bekeken Gangnam Style van Psy is of een willekeurige grappige kat, al deze filmpjes moeten ergens worden opgeslagen. Alsof dat nog niet genoeg is, wordt, zoals we sinds kort weten, door overheidsdiensten ook nog eens opgeslagen wie, waar wanneer naar al deze filmpjes kijkt.
In 2010 werd de mondiale jaarlijkse informatieproductie geschat op 1200 exabytes (dat is 1200 miljard gigabytes). En dat terwijl de totale productie in 2002 nog op 2 exabytes werd geschat [178]. Deze exponentiële toename komt niet doordat we als mensheid zoveel creatiever geworden zijn maar puur door de technologische vooruitgang die het opslaan van digitale informatie zeer goedkoop heeft gemaakt. In mijn proefschrift bestudeer ik processen die een grote rol kunnen gaan spelen in de volgende generatie opslagmedia.

Magnetische opslag

Een groot deel van alle digitale informatie staat opgeslagen op harde schijven. Op een harde schijf is de informatie opgeslagen in een magnetisch materiaal. De nullen en enen worden gerepresenteerd door de oriëntatie van de magnetisatie. Bijvoorbeeld wanneer de magnetisatie in figuur 7.1 naar boven wijst representeert zij een één en wanneer zij omlaag wijst een nul. Typische domeinen meten een paar honderd nanometer in de radiale richting van de schijf en tientallen nanometers in de leesrichting. De voordelen van harde schijven zijn dat informatie bewaard blijft wanneer het apparaat is uitgeschakeld en de hoge informatiedichtheid voor relatief lage kosten.
De overgang tussen twee magnetische domeinen wordt een domeinwand genoemd. Het blijkt mogelijk om door middel van stroompulsen de domeinwanden te bewegen door de magneet. Dit verschijnsel zou in de toekomst kunnen leiden tot een geheugenmodule waarbij niet het magnetisch materiaal beweegt, zoals in een harde schijf, maar waarbij de domeinen, en dus de informatie zelf, met snelheden van ongeveer 100 m/s door de magneet racen. Dit type geheugen is als racetrack geheugen gepatenteerd door IBM. Wanneer het gerealiseerd kan worden zou het de voordelen van harde schijven combineren met lees- en schrijfsnelheden die aangetroffen worden in geheugen gebaseerd op transistors en bovendien zou het de kosten per opgeslagen bit nog verder verlagen.

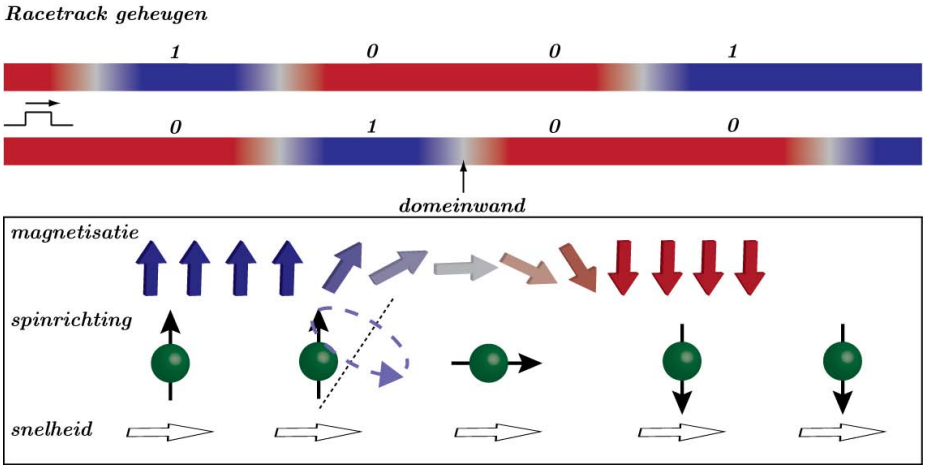

Figuur 7.1: Illustratie van het voorgestelde racetrack geheugen. Digitale informatie wordt gerepresenteerd door de richting van de magnetisatie. Door een stroompuls schuiven alle domeinwanden, en dus de informatie, in dezelfde richting. Daaronder een vergroting van een domeinwand en een elektron met de lokale spinrichting en snelheid. De precessie van de spinrichting rond de lokale magnetisatierichting leidt tot de loodrechte componenten die de *spin-transfer torque* veroorzaken. Deze hebben tot gevolg dat de domeinwanden met de elektronen mee bewegen.

Spin-transfer torque

In mijn proefschrift laat ik zien dat de natuurkunde achter het racetrackgeheugen met een simpel model begrepen kan worden. In dit model wordt de magneet beschreven door twee deelsystemen: een magnetisatierichting die veroorzaakt wordt door gelokaliseerde elektronen en daarnaast mobiele elektronen die voor de stroomgeleiding zorgen. De magnetisatie en het intrinsieke magnetisch moment van de mobiele elektronen zijn gekoppeld. Het gevolg van de koppeling is dat het systeem de laagste energie heeft wanneer de magnetisatie en het moment van de elektronen parallel zijn. Wanneer het moment van de elektronen niet parallel is aan de magnetisatierichting zal het een precessiebeweging uitvoeren.
Het intrinsieke magnetische moment van elektronen wordt veroorzaakt door hun spin; het intrinsieke impulsmoment van de elektronen. Door de koppeling van magnetisatie en elektronspin zal een elektrische stroom door een magneet gepolariseerd zijn met de spinpolarisatie parallel aan de magnetisatierichting.
Wanneer we nu een stroom door twee aangrenzende magnetische domeinen met verschillende magnetisatierichtingen beschouwen, dan verandert de spinpolarisatie van die stroom van parallel aan de magnetisatierichting van de eerste magneet naar parallel aan die van de tweede, zoals geïllustreerd in figuur 7.1. De veranderende spinpolarisatie betekent dat het spinimpulsmoment dat door de stroom wordt meegevoerd veranderd. Omdat het impulsmoment van het totale systeem behouden is, volgt dat het impulsmo-

ment geassocieerd met de magnetisatie een even grote maar tegengestelde verandering moet ondergaan. Deze verandering van impulsmoment betekent dat er een krachtmoment op de magnetisatie werkt. Dit krachtmoment dat geïnduceerd wordt door een stroom wordt een *spin-transfer torque* genoemd.
Microscopisch wordt de *spin-transfer torque* veroorzaakt door de componenten van de spinpolarisatie loodrecht op de richting van de magnetisatie. In een homogene magneet wijzen de spins van alle elektronen gemiddeld in de richting van de magnetisatie en dus zijn er geen loodrechte componenten en geen krachtmomenten. De loodrechte componenten van de polarisatie ontstaan wanneer de magnetisatierichting verandert als functie van de positie. In figuur 7.1 is dit geïllustreerd bij het tweede elektron van links. Een klein verschil tussen de spinrichting en de lokale magnetisatierichting leidt tot precessie om magnetisatierichting van de spin. Dit heeft een loodrechte component van de spinpolarisatie tot gevolg.

Spin-baan koppeling

Naast de *spin-transfer torque* is er in bepaalde systemen ook een krachtmoment op een homogene magnetisatierichting geobserveerd. Een mogelijke verklaring voor dit krachtmoment is een spinpolarisatie veroorzaakt door spin-baan koppeling van de elektronen.
Spin-baan koppeling wordt in deze systemen wordt veroorzaakt door het breken van inversie symmetrie langs een bepaalde as. Dit wil zeggen dat het systeem er verschillend uitziet wanneer het wordt gespiegeld in het vlak loodrecht op die as. Typisch bestaan de magnetische systemen die experimenteel bestudeerd worden uit verschillende gestapelde laagjes. Wanneer de laagjes die het magnetische laagje omringen van verschillende materialen of dikte zijn is de inversiesymmetrie in de richting van stapelen gebroken. Zoals het voorbeeldsysteem in figuur 7.2 dat bestaat uit een stapeling van aluminiumoxide, kobalt en platina.
Langs de as van de asymmetrie kan in deze materialen een elektrisch veld bestaan. Voor de elektronen, die met een bepaalde snelheid door het materiaal bewegen, heeft dit veld een magnetische component. Dit magnetische veld koppelt aan de spinrichting van de elektronen zoals ook de magnetisatie dat doet. Uit de details van de berekeningen volgt dat het door spin-baan koppeling genduceerde magnetische veld (gele pijlen in figuur 7.2) loodrecht staat op zowel de bewegingsrichting van de elektronen en de as waarlangs de symmetrie gebroken is.
Spin-baan koppeling kan dus genterpreteerd worden als de koppeling tussen de spin en een magnetisch veld dat afhangt van de snelheid van het elektron. Wanneer een stroom door de magneet wordt aangelegd is er een netto snelheid van de elektronen. Dit leidt, door de bovengenoemde koppeling, tot een component van de spinpolarisatie in de richting van de het door spin-baan koppeling geïnduceerde veld (gele stippellijn in figuur 7.2). Wanneer het geïnduceerde veld en de magnetisatierichting niet parallel zijn leidt dit tot componenten van de spinpolarisatie loodrecht op de richting van de magnetisatie. Het krachtmomenten veroorzaakt door deze component wordt een *spin-orbit torque* genoemd.

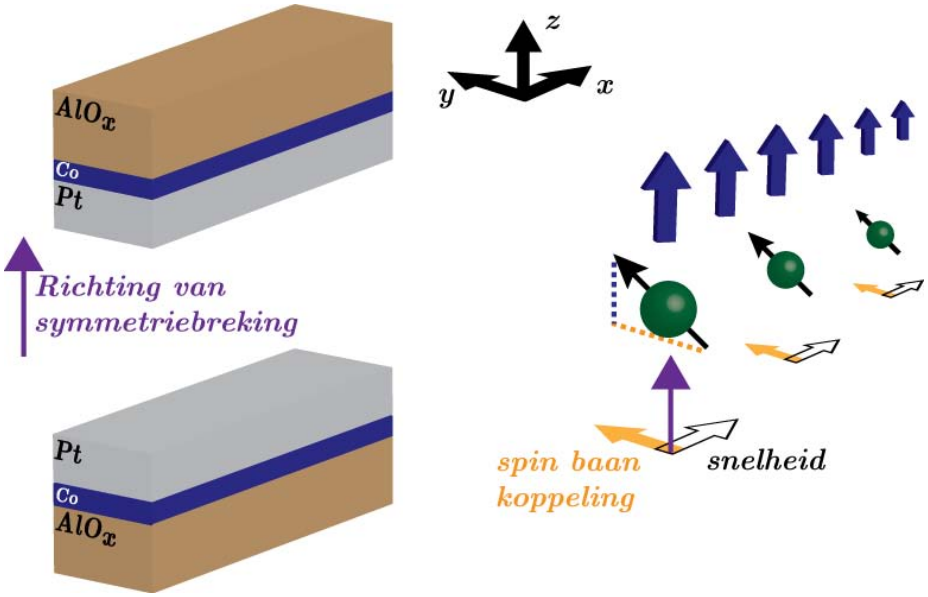

Figuur 7.2: Links een systeem waar het magnetische kobalt tussen een platina en aluminiumoxide laagjes zit. Een spiegeling langs de z as laat duidelijk zien dat de symmetrie gebroken is. Dit zorgt voor een magnetisch veld genduceerd door de spin-baan koppeling, geïllustreerd door de gele pijl, loodrecht op de richting van symmetriebreking en bewegingsrichting. De spinpolarisatie wijst in de richting van het gecombineerde veld van de magnetisatie en het veld ontstaan door de spin-baan koppeling. Het gevolg is een loodrechte component van de spinpolarisatie die voor een krachtmoment zorgt.

Symmetrie

In mijn proefschrift laat ik zien dat wanneer er zowel spin-baan koppeling als een positieafhankelijke magnetisatierichting is er veel meer krachtmomenten op de magnetisatie werken dan alleen de bovengenoemde *spin-transfer torque* en *spin-orbit torque*. Dit doe ik op twee manieren, de eerste is door een analyse van de symmetrieën van het systeem. De tweede manier is gebaseerd op een berekening aan de hand van het hierboven geïntroduceerde model. Hier zal ik de eerste methode toelichten.
We hebben gezien dat krachtmomenten geïnduceerd worden door componenten van de spinpolarisatie loodrecht op de magnetisatierichting. Wanneer er geen spin-baan koppeling is zijn we bij de beschrijving van het systeem vrij om de richtingen van de magnetisatie en spins gezamenlijk willekeurig te draaien ten opzichte van de coördinaten in ons laboratorium. De relatieve oriëntatie van de magnetisatie en spins verandert hierdoor niet waardoor de krachtmomenten gelijk blijven.
Alle krachtmomenten die we voor dit systeem op grond van het bovenstaande argument mogen opschrijven moeten dus onafhankelijk zijn van onafhankelijke rotaties van de laboratorium coördinaten en magnetisatie- en spinrichtingen. Een aangelegd elektrisch

veld $\boldsymbol{E}$ en de verandering van de magnetisatierichting $\boldsymbol{\nabla m}$ draaien met de coördinaten van het laboratorium mee. Dit betekend dat de enig mogelijke krachtmomenten die eerste orde zijn in de verandering van de magnetisatierichting en het elektrische veld gegeven worden door $\boldsymbol{\tau} \propto (\boldsymbol{E}\cdot\boldsymbol{\nabla})\boldsymbol{m} + \beta \boldsymbol{m}\times(\boldsymbol{E}\cdot\boldsymbol{\nabla})\boldsymbol{m}$, waar β een constante is die de verhouding tussen deze twee krachtmomenten bepaald. Onafhankelijke rotaties laten het inproduct tussen het elektrisch veld en de verandering van de magnetisatierichting ongewijzigd en de krachtmomenten roteren zo hetzelfde als de magnetisatie.
Dit zijn precies de reactieve en dissipatieve spin-transfer torques. Het dissipatieve krachtmoment, welke evenredig met β is in bovenstaande vergelijking, kan ook met het in de voorafgaande secties geïntroduceerde model gevonden worden. Dan moeten we voor de bewegingsvergelijking van de spin naast de precessiebeweging ook relaxatie naar de magnetisatierichting toevoegen.

Meer mogelijkheden

Als er spin-baan koppeling is hebben we niet meer de vrijheid om de magnetisatie en spinrichtingen onafhankelijk van ons laboratorium te draaien. Dit komt doordat de genduceerde spinpolarisatie niet langer alleen gekoppeld is aan de magnetisatierichting maar ook expliciet aan de bewegingsrichting van de elektronen, zie figuur 7.2. Daarom moet een draaiing van magnetisatie- en spinrichtingen in dit geval altijd gecombineerd worden met een gelijke draaiing van het assenstelsel in het laboratorium.
De eisen aan de mogelijke krachtmomenten zijn nu veel minder strikt omdat ze alleen onder een totale rotatie van het systeem gelijk moeten blijven. Wanneer de magnetisatierichting niet positieafhankelijk is zijn er twee mogelijke krachtmomenten die lineair in het elektrisch veld en de sterkte van de spin-baan koppeling zijn. Deze worden gegeven door $\boldsymbol{\tau} \propto \boldsymbol{m}\times(\boldsymbol{E}\times\boldsymbol{z}) + \beta'\boldsymbol{m}\times(\boldsymbol{E}\times\boldsymbol{z})\times\boldsymbol{m}$, waar $\boldsymbol{z}$ de as van symmetriebreking is en β' een constante is die de verhouding tussen de reactieve en dissipatieve *spin-orbit torques* weergeeft.
Deze krachtmomenten waren al bekend. Maar wanneer er naast spin-baan koppeling ook een positieafhankelijke magnetisatie is dan vinden we op eerste orde in de sterkte van de spin-baan koppeling al veertien extra mogelijke krachtmomenten naast de hierboven genoemde. Deze krachtmomenten hangen af van het elektrische veld, de verandering van de magnetisatie en de richting van symmetriebreking.
Ook voor al deze extra krachtmomenten geldt dat ze in paren van reactieve en dissipatieve krachtmomenten voorkomen. Deze paren worden steeds gevormd door een toegestaan krachtmoment en het vectorproduct tussen dit krachtmoment en de magnetisatierichting. De relatieve sterkte van alle krachtmomenten kan niet door middel van symmetrie bepaald worden. Uit berekeningen aan de hand van het model van magnetisatierichting gekoppeld aan de spin van de elektronen kan de sterkte van de krachtmomenten bepaald worden. En daaruit weer het effect op de beweging van domeinwanden.
Uit de berekeningen komt dat de domeinwandsnelheid als functie van het elektrische veld kwalitatief behoorlijk kan verschillen afhankelijk van de relatieve sterkte van alle door ons voorspelde krachtmomenten. Het is nu wachten op metingen die uitsluitsel kunnen

geven welke combinatie van krachtmomenten de stroomgeïnduceerde beweging van de domeinwand het beste beschrijven.
Om de domeinwanden door de magnetische draden te laten racen zijn behoorlijke stroomdichtheden nodig. Deze zijn zo groot dat zelfs op nanoschaal de draden behoorlijk verhit worden door Ohmse dissipatie. De verhitting door de stromen en omdat er op de markt geheugenchips zijn die juist een lokale opwarming gebruiken om eenvoudiger informatie te kunnen schrijven met behulp van de *spin-transfer torques* hebben we ook het effect van een temperatuurgradiënt op de krachtmomenten bestudeerd.
Het blijkt een behoorlijke uitdaging om thermische effecten in systemen met spin-baan koppeling uit te rekenen. Wanneer we de lineaire respons van een systeem willen uitrekenen als functie van een temperatuurgradiënt lopen we tegen een term aan die zich onfysisch gedraagt. In de limiet dat de temperatuur naar nul gaat zou er een oneindig krachtmoment zijn en thermisch geïnduceerde stroom gaan lopen. In mijn proefschrift bestudeer ik de oorsprong van deze term en laat ik zien hoe de berekening hersteld kan worden.
Het is spannend of de extra krachtmomenten experimenteel aangetoond kunnen worden en of het racetrackgeheugen de geheugentechnologie van de toekomst gaat worden.

Dankwoord

De eerste persoon die ik wil bedanken is Rembert Duine. Naast een uitstekende begeleider, die altijd beschikbaar was voor een goed idee, technische hulp, extra motivatie of een gezellig praatje, is hij ook nog een leuke vent. Dat laatste ben ik onder meer te weten gekomen door gezamenlijke fietstochtjes, afdalingen van zwarte pistes en karaokeavonden. Overigens is hij me in alle hier genoemde disciplines de baas. Ik wil hem enorm bedanken voor zijn hulp bij het tot stand komen van dit proefschrift en de leuke tijd.
Ook zonder Henk Stoof was er waarschijnlijk geen proefschrift van mijn hand gekomen. Niet alleen omdat hij me bij Rembert heeft aanbevolen voor de promotieplaats maar vooral omdat ik tijdens mijn masterscriptie onder zijn leiding plezier gekregen heb in het doen van onderzoek. Daarnaast was hij ook tijdens mijn promotie altijd beschikbaar voor vragen en discussies.
A special word of gratitude to Hiroshi Kohno. Who did not only help me with my calculations but also made my visit to Japan a very pleasant experience. This was due to the many parties that he organised, the excursion to shinsekai district and the strange but often glorious Japanese food he ordered for me.
I also want to thank Roberto Troncoso for the nice collaboration that resulted in Chapter 5. And furthermore for showing me the maximum number of potatoes that fit on a grill.
Vervolgens wil ik Gerard Barkema bedanken. Uit de discussies tijdens het vak dat ik assisteerde is het project dat tot hoofdstuk zes heeft geleid voortgekomen.
Furthermore, I would like to thank all the past and present members of the BEC group and the institute for theoretical physics for providing the nice atmosphere for doing research. A few of those I want to mention here explicitly, Joost, Jildou, Ties, Rene and Jan for sharing tremendous amounts of coffee and endless conversations. Also my (former) roommates, Marius, Jogundas and Andreas I would like to acknowledge for all the nice discussions.
Ook zonder de ondersteuning van Olga, Els, Riny and Wanda zou dit proefschrift niet tot stand gekomen zijn. Daarom wil ik ook hen hartelijk bedanken.
Als laatste wil ik Marthe bedanken. Voor alle moedige pogingen te begrijpen waar dit proefschrift over gaat. Maar bovenal omdat ze mijn leven zo leuk maakt.

Curriculum Vitae

Erik van der Bijl werd op 26 november 1985 te Rotterdam geboren. Zijn gymnasiumdiploma behaalde hij in 2004 aan het Huygenslyceum in Voorburg. Daarna begon hij in Utrecht aan de bacheloropleidingen Natuur- en Sterrenkunde en Wiskunde. Na succesvolle voltooiing van deze programma's schreef hij zich in voor de masteropleiding theoretische natuurkunde. Na een extra semester aan de Universität Zürich begon hij aan zijn scriptie over zeer koude en ijle gaswolken van sterk wisselwerkende bosonen. Vervolgens begon hij aan zijn promotieonderzoek dat tot dit proefschrift heeft geleid.

Bibliography

[1] G. Binasch, P. Grünberg, F. Saurenbach, and W. Zinn, Phys. Rev. B **39**, 4828 (1989).

[2] M. N. Baibich, J. M. Broto, A. Fert, F. N. Van Dau, F. Petroff, P. Etienne, G. Creuzet, A. Friederich, and J. Chazelas, Phys. Rev. Lett. **61**, 2472 (1988).

[3] S. Datta and B. Das, Applied Physics Letters **56**, 665 (1990).

[4] S. A. Wolf, D. D. Awschalom, R. A. Buhrman, J. M. Daughton, S. von Molnr, M. L. Roukes, A. Y. Chtchelkanova, and D. M. Treger, Science **294**, 1488 (2001).

[5] I. Žutić, J. Fabian, and S. Das Sarma, Rev. Mod. Phys. **76**, 323 (2004).

[6] B. Dieny, V. S. Speriosu, S. S. P. Parkin, B. A. Gurney, D. R. Wilhoit, and D. Mauri, Phys. Rev. B **43**, 1297 (1991).

[7] L. Berger, Phys. Rev. B **54**, 9353 (1996).

[8] J. Slonczewski, Journal of Magnetism and Magnetic Materials **159**, L1 (1996).

[9] M. Tsoi, A. G. M. Jansen, J. Bass, W.-C. Chiang, M. Seck, V. Tsoi, and P. Wyder, Phys. Rev. Lett. **80**, 4281 (1998).

[10] E. B. Myers, D. C. Ralph, J. A. Katine, R. N. Louie, and R. A. Buhrman, Science **285**, 867 (1999).

[11] G. Tatara, H. Kohno, and J. Shibata, Physics Reports **468**, 213 (2008).

[12] A. Brataas, A. D. Kent, and H. Ohno, Nature Materials **11**, 372 (2012).

[13] G. E. Volovik, Journal of Physics C: Solid State Physics **20**, L83 (1987).

[14] G. Tatara and H. Kohno, Phys. Rev. Lett. **92**, 086601 (2004).

[15] H. Kohno, G. Tatara, and J. Shibata, Journal of the Physical Society of Japan **75**, 113706 (2006).

[16] A. Stern, Phys. Rev. Lett. **68**, 1022 (1992).

[17] S. E. Barnes and S. Maekawa, Phys. Rev. Lett. **95**, 107204 (2005).

[18] S. E. Barnes and S. Maekawa, Phys. Rev. Lett. **98**, 246601 (2007).

[19] Everspin Technologies, (2012).

[20] S. S. P. Parkin, M. Hayashi, and L. Thomas, Science **320**, 190 (2008).

[21] Y. Tserkovnyak, A. Brataas, and G. E. W. Bauer, Phys. Rev. Lett. **88**, 117601 (2002).

[22] W. M. Saslow, Phys. Rev. B **76**, 184434 (2007).

[23] J.-i. Ohe, A. Takeuchi, and G. Tatara, Phys. Rev. Lett. **99**, 266603 (2007).
[24] R. A. Duine, Phys. Rev. B **77**, 014409 (2008).
[25] S. A. Yang, G. S. D. Beach, C. Knutson, D. Xiao, Q. Niu, M. Tsoi, and J. L. Erskine, Phys. Rev. Lett. **102**, 067201 (2009).
[26] Y. Tserkovnyak and M. Mecklenburg, Phys. Rev. B **77**, 134407 (2008).
[27] M. V. Berry, Proceedings of the Royal Society of London. A. Mathematical and Physical Sciences **392**, 45 (1984).
[28] Y. Aharonov and A. Stern, Phys. Rev. Lett. **69**, 3593 (1992).
[29] A. C. Swaving and R. A. Duine, Phys. Rev. B **83**, 054428 (2011).
[30] K. M. D. Hals, Y. Tserkovnyak, and A. Brataas, Phys. Rev. Lett. **106**, 107206 (2011).
[31] A. H. MacDonald and M. Tsoi, Philosophical Transactions of the Royal Society A: Mathematical, Physical and Engineering Sciences **369**, 3098 (2011).
[32] A. Manchon and S. Zhang, Phys. Rev. B **78**, 212405 (2008).
[33] A. Manchon and S. Zhang, Phys. Rev. B **79**, 094422 (2009).
[34] D. A. Pesin and A. H. MacDonald, Phys. Rev. B **86**, 014416 (2012).
[35] J. Ryu, S.-M. Seo, K.-J. Lee, and H.-W. Lee, J. Magn. Magn. Mater. **324**, 1449 (2012).
[36] E. van der Bijl and R. A. Duine, Phys. Rev. B **86**, 094406 (2012).
[37] G. E. W. Bauer, in *Spin Current* (Oxford University Press, 2012) Chap. 9.
[38] A. Brataas, Y. Tserkovnyak, and G. E. W. Bauer, Phys. Rev. Lett. **101**, 037207 (2008).
[39] K. M. D. Hals, A. K. Nguyen, and A. Brataas, Phys. Rev. Lett. **102**, 256601 (2009).
[40] R. A. Duine, A. S. Núñez, J. Sinova, and A. H. MacDonald, Phys. Rev. B **75**, 214420 (2007).
[41] Y. Tserkovnyak, H. J. Skadsem, A. Brataas, and G. E. W. Bauer, Phys. Rev. B **74**, 144405 (2006).
[42] C. H. Wong and Y. Tserkovnyak, Phys. Rev. B **84**, 115209 (2011).
[43] C. H. Wong and Y. Tserkovnyak, Phys. Rev. B **80**, 184411 (2009).
[44] Y. Tserkovnyak and C. H. Wong, Phys. Rev. B **79**, 014402 (2009).
[45] L. Onsager, Phys. Rev. **37**, 405 (1931).
[46] L. Landau and E. Lifshitz, *Statistical Physics*, 3rd ed., Vol. 1 (Pergamon Press, 1975) pp. 365 – 371.
[47] A. A. Thiele, Phys. Rev. Lett. **30**, 230 (1973).
[48] A. Yamaguchi, T. Ono, S. Nasu, K. Miyake, K. Mibu, and T. Shinjo, Phys. Rev. Lett. **92**, 077205 (2004).
[49] M. Kläui, P.-O. Jubert, R. Allenspach, A. Bischof, J. A. C. Bland, G. Faini, U. Rüdiger, C. A. F. Vaz, L. Vila, and C. Vouille, Phys. Rev. Lett. **95**, 026601 (2005).
[50] O. Tchernyshyov and G.-W. Chern, Phys. Rev. Lett. **95**, 197204 (2005).

[51] S.-B. Choe, Y. Acremann, A. Scholl, A. Bauer, A. Doran, J. Sthr, and H. A. Padmore, Science **304**, 420 (2004).

[52] B. Van Waeyenberge, A. Puzic, H. Stoll, K. W. Chou, T. Tyliszczak, R. Hertel, M. Fahnle, H. Bruckl, K. Rott, G. Reiss, I. Neudecker, D. Weiss, C. H. Back, and G. Schutz, Nature **444**, 461 (2006).

[53] K.-S. Lee and S.-K. Kim, Applied Physics Letters **91**, 132511 (2007).

[54] M. Bolte, G. Meier, B. Krüger, A. Drews, R. Eiselt, L. Bocklage, S. Bohlens, T. Tyliszczak, A. Vansteenkiste, B. Van Waeyenberge, K. W. Chou, A. Puzic, and H. Stoll, Phys. Rev. Lett. **100**, 176601 (2008).

[55] K. Tanabe, D. Chiba, J. Ohe, S. Kasai, H. Kohno, S. E. Barnes, S. Maekawa, K. Kobayashi, and T. Ono, Nature Communications , 845 (2012).

[56] S. A. Yang, G. S. D. Beach, C. Knutson, D. Xiao, Z. Zhang, M. Tsoi, Q. Niu, A. H. MacDonald, and J. L. Erskine, Phys. Rev. B **82**, 054410 (2010).

[57] Y. Nakatani, A. Thiaville, and J. Miltat, Nature Materials **2**, 521 (2003).

[58] A. M. Polyakov and A. Belavin, JETP Lett. **22**, 245 (1975).

[59] J. Shibata, Y. Nakatani, G. Tatara, H. Kohno, and Y. Otani, Phys. Rev. B **73**, 020403 (2006).

[60] J.-H. Moon and K.-J. Lee, J. Magn. (2011), 10.4283/jmag.2011.16.1.006.

[61] M. E. Lucassen, G. C. F. L. Kruis, R. Lavrijsen, H. J. M. Swagten, B. Koopmans, and R. A. Duine, Phys. Rev. B **84**, 014414 (2011).

[62] M. Hayashi, J. Ieda, Y. Yamane, J.-i. Ohe, Y. K. Takahashi, S. Mitani, and S. Maekawa, Phys. Rev. Lett. **108**, 147202 (2012).

[63] J. Sinova, D. Culcer, Q. Niu, N. A. Sinitsyn, T. Jungwirth, and A. H. MacDonald, Phys. Rev. Lett. **92**, 126603 (2004).

[64] I. E. Dzyaloshinkii, Sov. Phys. JETP **20**, 665 (1965).

[65] T. Moriya, Phys. Rev. Lett. **4**, 228 (1960).

[66] A. Thiaville, S. Rohart, E. Jué, V. Cros, and A. Fert, EPL (Europhysics Letters) **100**, 57002 (2012).

[67] K.-S. Ryu, L. Thomas, S.-H. Yang, and S. Parkin, Nature Nanotechnology **8**, 527 (2013).

[68] E. Satoru, U. Bauer, S.-M. Ahn, E. Martinez, and G. S. D. Beach, Nature Materials **12**, 611 (2013).

[69] S. Mühlbauer, B. Binz, F. Jonietz, C. Pfleiderer, A. Rosch, A. Neubauer, R. Georgii, and P. Böni, Science **323**, 915 (2009).

[70] T. H. R. Skyrme, Proceedings of the Royal Society of London. Series A. Mathematical and Physical Sciences **260**, 127 (1961).

[71] J. J. Sakurai, *Modern Quantum Mechanics* (Addison-Wesley, 1994).

[72] J. D. Jackson, *Classical Electrodynamics*, 3rd ed. (John Wiley & Sons, Inc., 1998) Chap. 11.

[73] G. Dresselhaus, Phys. Rev. **100**, 580 (1955).

[74] Y. A. Bychkov and E. I. Rashba, Journal of Physics C: Solid State Physics **17**,

6039 (1984).
[75] E. I. Rashba, Fiz. Tverd. Tela (Leningrad) **2**, 1224 (1960).
[76] G. Sundaram and Q. Niu, Phys. Rev. B **59**, 14915 (1999).
[77] B. Binz and A. Vishwanath, Phys. Rev. B **74**, 214408 (2006).
[78] M.-C. Chang and Q. Niu, Phys. Rev. B **53**, 7010 (1996).
[79] R. Karplus and J. M. Luttinger, Phys. Rev. **95**, 1154 (1954).
[80] N. A. Sinitsyn, J. Phys.: Condens. Matter **20**, 023201 (2008).
[81] N. Nagaosa, J. Sinova, S. Onoda, A. H. MacDonald, and N. P. Ong, Rev. Mod. Phys. **82**, 1539 (2010).
[82] F. D. M. Haldane, Phys. Rev. Lett. **93**, 206602 (2004).
[83] D. J. Thouless, M. Kohmoto, M. P. Nightingale, and M. den Nijs, Phys. Rev. Lett. **49**, 405 (1982).
[84] M. Z. Hasan and C. L. Kane, Rev. Mod. Phys. **82**, 3045 (2010).
[85] Z. Li and S. Zhang, Phys. Rev. B **69**, 134416 (2004).
[86] D. Xiao, M.-C. Chang, and Q. Niu, Rev. Mod. Phys. **82**, 1959 (2010).
[87] D. Xiao, J. Shi, and Q. Niu, Phys. Rev. Lett. **95**, 137204 (2005).
[88] D. Xiao, Y. Yao, Z. Fang, and Q. Niu, Phys. Rev. Lett. **97**, 026603 (2006).
[89] L. Smrcka and P. Streda, Journal of Physics C: Solid State Physics **10**, 2153 (1977).
[90] N. R. Cooper, B. I. Halperin, and I. M. Ruzin, Phys. Rev. B **55**, 2344 (1997).
[91] J. M. Luttinger, Phys. Rev. **135**, A1505 (1964).
[92] J. Shi, G. Vignale, D. Xiao, and Q. Niu, Phys. Rev. Lett. **99**, 197202 (2007).
[93] T. Qin, Q. Niu, and J. Shi, Phys. Rev. Lett. **107**, 236601 (2011).
[94] S. Zhang and Z. Li, Phys. Rev. Lett. **93**, 127204 (2004).
[95] F. Piéchon and A. Thiaville, Phys. Rev. B **75**, 174414 (2007).
[96] R. A. Duine, Phys. Rev. B **79**, 014407 (2009).
[97] L. Thomas, M. Hayashi, X. Jiang, R. Moriya, C. Rettner, and S. Parkin, Nature **443**, 197 (2006).
[98] L. Heyne, M. Kläui, D. Backes, T. A. Moore, S. Krzyk, U. Rüdiger, L. J. Heyderman, A. F. Rodríguez, F. Nolting, T. O. Mentes, M. A. Niño, A. Locatelli, K. Kirsch, and R. Mattheis, Phys. Rev. Lett. **100**, 066603 (2008).
[99] L. Heyne, J. Rhensius, D. Ilgaz, A. Bisig, U. Rüdiger, M. Kläui, L. Joly, F. Nolting, L. J. Heyderman, J. U. Thiele, and F. Kronast, Phys. Rev. Lett. **105**, 187203 (2010).
[100] M. E. Lucassen, C. H. Wong, R. A. Duine, and Y. Tserkovnyak, Applied Physics Letters **99**, 262506 (2011).
[101] K. Obata and G. Tatara, Phys. Rev. B **77**, 214429 (2008).
[102] I. Garate and A. H. MacDonald, Phys. Rev. B **80**, 134403 (2009).
[103] I. Miron, K. Garello, G. Gaudin, P.-J. Zermatten, M. Costache, S. Auffret, S. Bandiera, B. Rodmacq, A. Schuhl, and P. Gambardella, Nature **476**, 189 (2011).
[104] I. Miron, T. Moore, H. Szambolics, L. Buda-Prejbeanu, S. Auffret, B. Rodmacq, S. Pizzini, J. Vogel, M. Bonfim, A. Schuhl, and G. Gaudin, Nature Materials **10**,

419 (2011).

[105] L. Liu, O. J. Lee, T. J. Gudmundsen, D. C. Ralph, and R. A. Buhrman, Phys. Rev. Lett. **109**, 096602 (2012).

[106] K.-W. Kim, S.-M. Seo, J. Ryu, K.-J. Lee, and H.-W. Lee, Phys. Rev. B **85**, 180404 (2012).

[107] K. M. D. Hals and A. Brataas, (2012), private communication.

[108] T. Jungwirth, Q. Niu, and A. H. MacDonald, Phys. Rev. Lett. **88**, 207208 (2002).

[109] E. van der Bijl and R. A. Duine, Phys. Rev. Lett. **107**, 195302 (2011).

[110] H. Kurebayashi, J. Sinova, D. Fang, A. C. Irvine, J. Wunderlich, V. Novak, R. P. Campion, B. L. Gallagher, E. K. Vehstedt, L. P. Zarbo, K. Vyborny, A. J. Ferguson, and T. Jungwirth, (2013).

[111] G. Tatara and H. Kohno, Phys. Rev. Lett. **96**, 189702 (2006).

[112] D. Culcer, M. E. Lucassen, R. A. Duine, and R. Winkler, Phys. Rev. B **79**, 155208 (2009).

[113] K. Uchida, S. Takahashi, K. Harii, J. Ieda, W. Koshibae, K. Ando, S. Maekawa, and E. Saitoh, Nature **455**, 778 (2008).

[114] H. Yu, S. Granville, D. P. Yu, and J.-P. Ansermet, Phys. Rev. Lett. **104**, 146601 (2010).

[115] J. Flipse, F. Bakker, A. Slachter, F. K. Dejene, and B. van Wees, Nature Nanotechnology **7**, 166 (2012).

[116] C. H. Wong, H. J. van Driel, R. Kittinaradorn, H. T. C. Stoof, and R. A. Duine, Phys. Rev. Lett. **108**, 075301 (2012).

[117] R. Kubo, Journal of the Physical Society of Japan **12**, 570 (1957).

[118] T. Thonhauser, D. Ceresoli, D. Vanderbilt, and R. Resta, Phys. Rev. Lett. **95**, 137205 (2005).

[119] A. Sakai and H. Kohno, (2013), private communication.

[120] R. Jansen, Nature Materials **11**, 400 (2012).

[121] S. Takahashi and S. Maekawa, Science and Technology of Advanced Materials **9**, 014105 (2008).

[122] P. W. Brouwer, Phys. Rev. B **58**, R10135 (1998).

[123] G. Lampel, Phys. Rev. Lett. **20**, 491 (1968).

[124] S. D. Ganichev, E. L. Ivchenko, S. N. Danilov, J. Eroms, W. Wegscheider, D. Weiss, and W. Prettl, Phys. Rev. Lett. **86**, 4358 (2001).

[125] M. J. Stevens, A. L. Smirl, R. D. R. Bhat, A. Najmaie, J. E. Sipe, and H. M. van Driel, Phys. Rev. Lett. **90**, 136603 (2003).

[126] C. W. Sandweg, Y. Kajiwara, A. V. Chumak, A. A. Serga, V. I. Vasyuchka, M. B. Jungfleisch, E. Saitoh, and B. Hillebrands, Phys. Rev. Lett. **106**, 216601 (2011).

[127] K. Ando, S. Takahashi, J. Ieda, H. Kurebayashi, T. Trypiniotis, C. Barnes, S. Maekawa, and E. Saitoh, Nature Materials **10**, 655 (2011).

[128] H. Kurebayashi, O. Dzyapko, V. Demidov, D. Fang, A. Ferguson, and S. Demokritov, Nature Materials **10**, 660 (2011).

[129] M. Weiler, H. Huebl, F. S. Goerg, F. D. Czeschka, R. Gross, and S. T. B. Goennenwein, Phys. Rev. Lett. **108**, 176601 (2012).

[130] Y. Tserkovnyak, A. Brataas, and G. E. W. Bauer, Phys. Rev. B **66**, 224403 (2002).

[131] S. Mizukami, Y. Ando, and T. Miyazaki, Phys. Rev. B **66**, 104413 (2002).

[132] E. Shikoh, K. Ando, K. Kubo, E. Saitoh, T. Shinjo, and M. Shiraishi, Phys. Rev. Lett. **110**, 127201 (2013).

[133] M. Johnson and R. H. Silsbee, Phys. Rev. B **35**, 4959 (1987).

[134] M. Johnson and R. H. Silsbee, Phys. Rev. B **37**, 5312 (1988).

[135] F. J. Jedema, M. S. Nijboer, A. T. Filip, and B. J. van Wees, Phys. Rev. B **67**, 085319 (2003).

[136] P. C. van Son, H. van Kempen, and P. Wyder, Phys. Rev. Lett. **58**, 2271 (1987).

[137] S. Dash, S. Sharma, R. Patel, M. De Jong, and R. Jansen, Nature **462**, 491 (2009).

[138] M. I. D'Yakonov and V. I. Perel', JETP Lett. **13**, 467 (1971).

[139] M. I. D'yakonov and V. I. Perel', Physics Letters A **35**, 459 (1971).

[140] J. E. Hirsch, Phys. Rev. Lett. **83**, 1834 (1999).

[141] V. Sih, W. H. Lau, R. C. Myers, V. R. Horowitz, A. C. Gossard, and D. D. Awschalom, Phys. Rev. Lett. **97**, 096605 (2006).

[142] S. Murakami, N. Nagaosa, and S.-C. Zhang, Science **301**, 1348 (2003).

[143] A. Slachter, F. Bakker, J.-P. Adam, and B. Van Wees, Nature Physics **6**, 879 (2010).

[144] J.-C. Le Breton, S. Sharma, H. Saito, S. Yuasa, and R. Jansen, Nature **475**, 82 (2011).

[145] M. König, S. Wiedmann, C. Brüne, A. Roth, H. Buhmann, L. W. Molenkamp, X.-L. Qi, and S.-C. Zhang, Science **318**, 766 (2007).

[146] C. L. Kane and E. J. Mele, Phys. Rev. Lett. **95**, 146802 (2005).

[147] R. A. Duine, P. M. Haney, A. S. Núñez, and A. H. MacDonald, Phys. Rev. B **75**, 014433 (2007).

[148] A. Brataas, Y. Nazarov, and G. Bauer, The European Physical Journal B - Condensed Matter and Complex Systems **22**, 99 (2001).

[149] K. Xia, P. J. Kelly, G. E. W. Bauer, A. Brataas, and I. Turek, Phys. Rev. B **65**, 220401 (2002).

[150] E. Saitoh, M. Ueda, H. Miyajima, and G. Tatara, Applied Physics Letters **88**, 182509 (2006).

[151] T. Kimura, Y. Otani, T. Sato, S. Takahashi, and S. Maekawa, Phys. Rev. Lett. **98**, 156601 (2007).

[152] V. Castel, N. Vlietstra, J. B. Youssef, and B. J. van Wees, Applied Physics Letters **101**, 132414 (2012).

[153] M. Hayashi, L. Thomas, C. Rettner, R. Moriya, Y. B. Bazaliy, and S. S. P. Parkin, Phys. Rev. Lett. **98**, 037204 (2007).

[154] I. M. Miron, P.-J. Zermatten, G. Gaudin, S. Auffret, B. Rodmacq, and A. Schuhl, Phys. Rev. Lett. **102**, 137202 (2009).

[155] D. A. Allwood, G. Xiong, C. C. Faulkner, D. Atkinson, D. Petit, and R. P. Cowburn, Science **309**, 1688 (2005).

[156] L. Onsager, Phys. Rev. **65**, 117 (1944).

[157] D. A. Huse and C. L. Henley, Phys. Rev. Lett. **54**, 2708 (1985).

[158] G. Blatter, M. V. Feigel'man, V. B. Geshkenbein, A. I. Larkin, and V. M. Vinokur, Rev. Mod. Phys. **66**, 1125 (1994).

[159] S. Lemerle, J. Ferré, C. Chappert, V. Mathet, T. Giamarchi, and P. Le Doussal, Phys. Rev. Lett. **80**, 849 (1998).

[160] L. S. E. Alvarez, K.-Y. Wang, and C. Marrows, Journal of Magnetism and Magnetic Materials **322**, 2529 (2010).

[161] G. Rodrguez-Rodrguez, J. L. Menndez, A. Hierro-Rodriguez, A. Prez-Junquera, N. Montenegro, D. Ravelosona, J. M. Alameda, and M. Vlez, Journal of Physics D: Applied Physics **43**, 305002 (2010).

[162] F. Cayssol, D. Ravelosona, C. Chappert, J. Ferré, and J. P. Jamet, Phys. Rev. Lett. **92**, 107202 (2004).

[163] T. Nattermann, in *Spin Glasses and Random Fields* (1997) Chap. 9, pp. 277–298.

[164] Dong, R. H., Zheng, B., and Zhou, N. J., EPL **98**, 36002 (2012).

[165] P. G. de Gennes, Rev. Mod. Phys. **57**, 827 (1985).

[166] J. P. Bouchaud, E. Bouchaud, G. Lapasset, and J. Planès, Phys. Rev. Lett. **71**, 2240 (1993).

[167] S. Bustingorry, A. B. Kolton, and T. Giamarchi, Phys. Rev. E **85**, 021144 (2012).

[168] Bustingorry, S., Kolton, A. B., and Giamarchi, T., EPL **81**, 26005 (2008).

[169] U. Nowak and K. D. Usadel, EPL (Europhysics Letters) **44**, 634 (1998).

[170] M. V. Feigel'man, V. B. Geshkenbein, A. I. Larkin, and V. M. Vinokur, Phys. Rev. Lett. **63**, 2303 (1989).

[171] M. E. J. Newman and G. T. Barkema, *Monte Carlo Methods in Statistical Physics* (Oxford University Press, 2006).

[172] R. Keesman, *Domain-wall structure*, unpublished.

[173] M. P. A. Fisher, D. S. Fisher, and J. D. Weeks, Phys. Rev. Lett. **48**, 368 (1982).

[174] R. Fisch, Journal of Statistical Physics **18**, 111 (1978).

[175] P. W. Anderson and Y. B. Kim, Rev. Mod. Phys. **36**, 39 (1964).

[176] T. Giamarchi, A. Kolton, and A. Rosso, in *Jamming, Yielding, and Irreversible Deformation in Condensed Matter*, Lecture Notes in Physics, Vol. 688, edited by M. Miguel and M. Rubi (Springer-Verlag, 2006) pp. 91–108.

[177] (2013), youTube Statistics.

[178] The Economist, Special Report: Managing Information (2010).